

---

# Photonic Metamaterials for Transformation Optics

---

Zur Erlangung des akademischen Grades eines  
DOKTORS DER NATURWISSENSCHAFTEN  
von der Fakultät für Physik des  
Karlsruher Instituts für Technologie (KIT)

genehmigte

DISSERTATION

von

Dipl.-Phys. Tolga Ergin  
aus Stuttgart

---

Tag der mündlichen Prüfung : 20. Januar 2012  
Referent : Prof. Dr. Martin Wegener  
Korreferent : Prof. Dr. Kurt Busch







# Publications

Parts of this thesis have already been published...

...in scientific journals:

- T. Ergin and M. Wegener, “Metamaterialien und Transformationsoptik,” Physik Journal, in preparation (2012).
- T. Ergin, J. Fischer, and M. Wegener, “Detailed Optical Characterization of Three-Dimensional Visible-Frequency Polarization-Independent Carpet Invisibility Cloak,” Physica B, accepted (2012).
- T. Ergin, J. Fischer, and M. Wegener, “Optical Phase Cloaking of 700 nm Light Waves in the Far Field by a Three-Dimensional Carpet Cloak,” Physical Review Letters **107**, 173901 (2011).
- J. Fischer, T. Ergin, and M. Wegener, “Three-Dimensional Polarization-Independent Visible-Frequency Carpet Invisibility Cloak,” Optics Letters **36**, 2059-2061 (2011).
- J. Müller, T. Ergin, N. Stenger, and M. Wegener, “Doppelt oder gar nicht sehen,” Physik Journal **10**, 16-17 (2011).
- T. Ergin, J. C. Halimeh, N. Stenger, and M. Wegener, “Optical Microscopy of 3D Carpet Cloaks: Ray-Tracing Calculations,” Optics Express **18**, 20535-20545 (2010).
- N. Stenger, T. Ergin, and M. Wegener, “Dreidimensionale optische Tarnkappe realisiert,” Physik in Unserer Zeit **41**, 218-219 (2010).
- J. C. Halimeh, T. Ergin, N. Stenger, and M. Wegener, “Transformationsoptik: Maßgeschneiderter optischer Raum,” Physik in unserer Zeit **41**, 170-175 (2010).
- T. Ergin, N. Stenger, P. Brenner, J. B. Pendry, and M. Wegener, “Three-Dimensional Invisibility Cloak at Optical Wavelengths,” Science **328**, 337-339 (2010).
- J. C. Halimeh, T. Ergin, J. Müller, N. Stenger, and M. Wegener, “Photorealistic Images of Carpet Cloaks,” Optics Express **17**, 19328-19336 (2009).

**...at conferences (only own presentations):**

- T. Ergin, J. Fischer, and M. Wegener, “Invisibility Cloaking for the Light Phase at Visible Frequencies,” contributed talk, SPIE Photonics West OPTO, San Francisco, CA, U.S.A., January 2012.
- T. Ergin, J. Fischer, J. C. Halimeh, N. Stenger, and M. Wegener, “3D Invisibility Cloaks at Visible Wavelengths,” **invited talk**, SPIE Optics+Photonics, San Diego, CA, U.S.A., August 2011.
- T. Ergin, J. Fischer, and M. Wegener, “Three-dimensional invisibility carpet cloak at 700 nm wavelength,” **invited talk**, CLEO/QUELS, Baltimore, MD, U.S.A., May 2011.
- T. Ergin, J. Fischer, J. C. Halimeh, N. Stenger, and M. Wegener, “3D Invisibility Cloaks at Optical Frequencies,” **invited talk**, SPIE Photonics West OPTO, San Francisco, CA, U.S.A., January 2011.
- T. Ergin, N. Stenger, P. Brenner, J. C. Halimeh, J. B. Pendry, and M. Wegener, “Three-Dimensional Invisibility-Cloaking Structure at Optical Frequencies,” contributed talk, CLEO/QELS, San Jose, CA, U.S.A., May 2010.
- T. Ergin, N. Stenger, J. Müller, J. C. Halimeh, and M. Wegener, “From Curved Space to Optical Cloaking,” contributed talk, DPG Spring Meeting, Dresden, Germany, March 2009.

# Contents

<b>Publications</b>	<b>i</b>
<b>1. Introduction</b>	<b>1</b>
<b>2. Transformation Optics</b>	<b>5</b>
2.1. Mathematical Framework . . . . .	5
2.1.1. Preparatory Considerations . . . . .	5
2.1.2. Mathematical Tools . . . . .	7
2.1.3. Curvature of Space and the Nature of Geodesics . . . . .	9
2.1.4. Deriving Optical Parameters from Geometries . . . . .	12
2.1.5. Exemplary Transformation Procedure . . . . .	20
2.1.6. Considerations on Dispersion and Superluminal Propagation . . . . .	23
2.2. Devices Based on Transformation Optics . . . . .	25
2.3. Carpet Cloak . . . . .	27
<b>3. Materials and Fabrication</b>	<b>33</b>
3.1. Metamaterials . . . . .	33
3.2. Photonic Crystals . . . . .	37
3.3. Fabrication Techniques . . . . .	42
3.3.1. Direct Laser Writing . . . . .	42
3.3.2. Stimulated-Emission-Depletion-Inspired Direct Laser Writing . . . . .	43
<b>4. Numerical Calculations</b>	<b>47</b>
4.1. Calculation of the Cloak's Index Distribution: Quasiconformal Mapping . . . . .	47
4.2. Finite-Element Calculations of the Carpet Cloak . . . . .	52
4.2.1. Performance of the Full Geometry . . . . .	53
4.2.2. Wavelength Dependence . . . . .	54
4.2.3. Angle Dependence . . . . .	56
4.3. Ray Tracing . . . . .	57
4.3.1. General Principle . . . . .	58
4.3.2. Photorealistic Images of a Macroscopic 3D Carpet Cloak . . . . .	58
4.3.3. Ray Tracing of Microscope Images . . . . .	66

<b>5. Experimental Results</b>	<b>81</b>
5.1. Blueprint and Fabrication of an Invisibility Cloak at Infrared Wavelengths	81
5.2. Setup and Measurement Results for the Infrared Cloak . . . . .	88
5.2.1. Optical Setup . . . . .	88
5.2.2. Measurement Results and Discussion . . . . .	90
5.3. Cloaking at Visible Wavelengths . . . . .	96
5.3.1. Parametric Studies of the Carpet Cloak at Visible Wavelengths . .	102
5.4. Full-Wave Cloaking Including the Light Phase . . . . .	107
<b>6. Summary</b>	<b>115</b>
<b>A. Appendix</b>	<b>121</b>
A.1. Finite-Element Calculations of the Cylindrical Cloak . . . . .	121
A.2. 90° Beam-Bending Sphere . . . . .	126
A.3. Finite-Element Calculations for TM polarization . . . . .	129
<b>Bibliography</b>	<b>133</b>
<b>Acknowledgments</b>	<b>148</b>

# 1. Introduction

For a long time, optical design has been more of an art than science. Master craftsmen carved and shaped transparent crystals in order to create the desired effects on the light's behavior. In the beginning, one might assume, this was done more by trial and error than anything else. After the proper concepts had been developed, the propagation of light rays could be described mathematically. But still, the geometrical shapes of materials were altered in order to refract the rays into their designated directions. And in a sense, although sophisticated computer software helps in the process, we still do this today: shaping (mostly) homogeneous materials until the light path matches the desired trajectory. But it turns out that this approach of designing optical elements is only one side of the medal. When we flip the medal, we discover the second approach: *a priori* planning of the exact light path, and deriving the corresponding optical parameters – not by shaping the geometry of materials, but by shaping the geometry of optical space itself.

This new approach on optical design is called transformation optics (TO). It is a field that offers new and fresh perspectives on “old” problems, but it also enables an unprecedented freedom of thoughts when it comes to conceiving and designing novel devices, some of which sound like they have sprung out of a science-fiction novel. However, the underlying idea of TO, namely that the geometry of space and the propagation of electromagnetic waves are connected, is not entirely new. Following A. Einstein's groundbreaking development of the Theory of General Relativity [1], it was in the beginning of the twentieth century (1924-1926) when pioneering work on the connection of light propagation and the implication of a changed space-time geometry was published [2, 3]. It took another 40 years before the correspondence between coordinate transformations of space-time and physical material parameters was first recognized and the basics of TO were established [4–7]. These early studies have not been noted too much at that time, one of the reasons being that the implications for the values of the optical parameters were grave – negative values and singularities could arise. This is due to the fact that the Jacobian matrix, which (as we will see) constitutes the optical parameters of the system and which is given directly by the applied coordinate transformation, is a purely mathematical entity with no physical constraints. In those years, there was simply no way of finding a material which could provide the necessary material parameters associated with the transformed geometry of space.

The last decade of the last millennium brought a new aspect to the game: metamaterials. J. B. Pendry and coworkers introduced these artificial composite materials [8, 9], which

can exhibit exotic optical parameters not found in nature, such as simultaneously negative permittivity and permeability. New possibilities opened up, such as materials with a negative index of refraction [10–15] (first proposed by V. G. Veselago [16]), creating the potential to realize exotic devices such as a perfect lens [16, 17]. The development of these new materials paved the way to rekindle the ideas of TO. It was at the beginning of the new millennium, when the field of TO was really developed and serious research was started [18, 19], most prominently by J. B. Pendry, D. R. Smith, U. Leonhardt and co-workers [20–26]. The field developed quite rapidly, and a plethora of theoretical suggestions for novel devices and optical elements followed [27, 28], some of which were demonstrated experimentally. However, since the demands on the material parameters arising from a transformation-optical design are often high (inhomogeneity, singularity, anisotropy), the experimental realization of most of the suggested devices has not been accomplished yet. Although there are theoretical proposals for the structure of metamaterials that exhibit the necessary optical parameters, they often are not feasible in terms of fabrication procedures and technology, especially at optical frequencies.

However, there is a class of transformation devices which only relies on spatially inhomogeneous optical parameters, while the local properties are isotropic. These devices can even be realized with a solely dielectric material response in some cases, neglecting the magnetic properties. One of these devices is the so-called “carpet cloak”, an invisibility cloak that can hide objects placed under a reflecting carpet and cancel out the corresponding distortions of the reflected light. Experimental progress for this type of cloak has been swift in a two-dimensional geometry and researchers pushed towards a three-dimensional realization. Remarkably, it only took five years since its birth in 2006 for the theory of TO to result in a device that was considered impossible or an entertaining artifact out of science-fiction novels for centuries: a three-dimensional polarization-independent invisibility cloak that works in the human visible spectrum. This invisibility cloak is the main topic of this thesis, and we will present how such a device is designed, numerically studied, fabricated, and optically characterized.

## Outline of this Thesis

In Chapter 2, the concepts of TO will be introduced. After establishing the necessary mathematical tools, we will describe how optical parameters are derived from coordinate transformations. To clarify this, the procedure will be demonstrated at an example and some of the implications of the transformation procedure will be discussed. The chapter closes with an overview over a variety of transformation devices, including the focus of this thesis, the carpet invisibility cloak. Chapter 3 will introduce the basic ideas of metamaterials. These materials are used to implement the sometimes exotic optical parameters of transformation devices. We will examine the material that is used in our experiments, a three-dimensional woodpile photonic crystal, and end the chapter by describing the used

---

fabrication techniques. Here, direct laser writing lithography as well as its enhanced version, namely stimulated-emission-depletion-inspired direct laser writing, will be discussed. In Chapter 4, we will turn to the numerical calculations that were carried out during the course of this thesis. After describing the derivation of the optical parameters of the carpet cloak and studying the cloak's performance with finite-element calculations, we will present various scenarios of ray-tracing calculations of the carpet cloak. These ray-tracing calculations will also provide the means to compare our experimental findings to theory. The main body of this thesis, the experimental results of three-dimensional carpet cloaking devices, is presented in Chapter 5. Starting with the schematic build-up of the cloak and describing the optical setups that are used for the measurements, we will subsequently demonstrate a cloak for infrared as well as for visible wavelengths of light. The dependence of the cloaking effect on various parameters, such as wavelength and incident angle, will also be determined. As the closing part of this chapter, the capability of a carpet cloak to reconstruct not only the amplitude, but also the phase of impinging electromagnetic waves, will be studied. In Chapter 6, we will summarize the results of this work.



## 2. Transformation Optics

This chapter is meant to give an introduction into the mathematical framework of TO, following the excellent book of U. Leonhardt and T. G. Philbin [26]. After the presentation of the principles of TO, we will demonstrate a complete transformation to clarify the procedure. The handling of magnetic responses is discussed afterwards, followed by some remarks on dispersion, losses and causality in TO. Subsequently, we will present an overview over some of the intriguing ideas for novel devices based on this theory. The last section in this chapter is devoted to introducing a special novel device and the main topic of this work – a type of invisibility cloak called the “carpet cloak”.

### 2.1. Mathematical Framework

#### 2.1.1. Preparatory Considerations

The fundamental idea of TO is that optical materials change the geometry that propagating light perceives, and, even more importantly, it also states the opposite: An altered geometry in the light’s path implies optical parameters for the medium, in which the light happens to propagate. Both statements are equivalent, yet the second statement has not found too much attention until recent years. The first statement, on the other hand, is anything but new. It was in January of 1662, when Marin Cureau de la Chambre, physician to the King of France, received a letter which contained ideas that would establish the fundamentals of Lagrangian and Hamiltonian dynamics, inspire Schrödinger’s quantum mechanics and greatly impact geometrical optics [29]. The author of the letter was Pierre de Fermat, and he formulated what became known as “Fermat’s principle”.

Fermat’s principle describes the behavior of light rays in optical media. It states that light always “chooses” the shortest path out of all possible. More precisely: light paths are always stationary. To describe this property, Fermat introduced the optical path length, in contrast to the geometrical path length. The optical path length  $s$  is described as the refractive index  $n$  multiplied by the geometrical path length  $l$ , or more precisely

$$s = \int n dl. \tag{2.1}$$

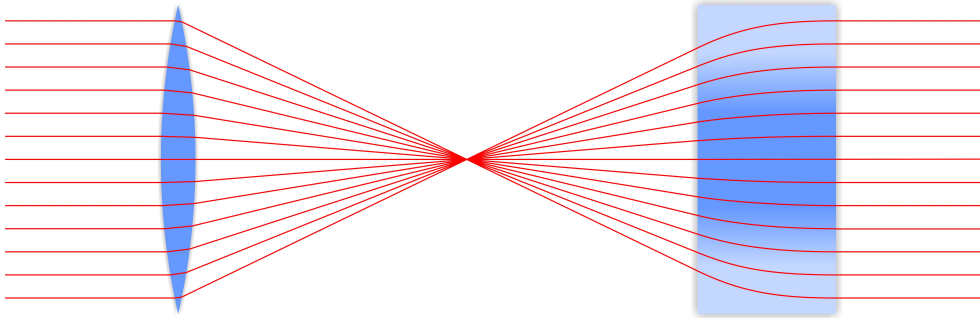


**Figure 2.1.:** Schematic drawing of two types of lenses. On the left, a usual biconvex lens out of a homogeneous material (blue) is shown. Light rays (red) travel in straight lines inside the lens and converge at the focus. On the right, a gradient-index (GRIN) lens is shown. The refractive index is color-coded in blue (darker means higher). Here, light rays follow curved paths to fulfill Fermat’s principle.<sup>1</sup>

Here,  $dl$  is an infinitesimal increment of  $l$  in Cartesian coordinates  $\{x, y, z\}$ :

$$dl = \sqrt{dx^2 + dy^2 + dz^2}. \quad (2.2)$$

For illustration, let us look at the path that light takes in two different types of lenses (Fig. 2.1). A parallel bundle of light rays hits a common biconvex lens. Since the lens is fabricated out of a homogeneous dielectric material (*e.g.*, glass), the rays refract according to Snell’s law  $n_1 \sin \theta_1 = n_2 \sin \theta_2$  at the interface of air and dielectric upon entering and exiting the lens. Here,  $n_1$  and  $\theta_1$  are the refractive index of air and the angle of the ray to the surface normal upon hitting the glass, respectively. The values with subscript 2 correspond to the parameters in the dielectric. Naturally, the rays travel in straight lines inside a homogeneous material, be it air or dielectric. All rays converge at the focus after exiting the lens. With regard to Fermat’s principle, this means that the optical path lengths of all rays should be minimal (otherwise light would not travel along them). In fact, this is true for all rays. In a simple argument, the additional geometrical path that rays with a large distance from the optical axis have to travel before hitting the focus is compensated by the shorter geometrical path inside the dielectric (with refractive index larger than unity). Actually, the optical path lengths of all rays are identical. Since the refractive index also connects the speed of light in the medium  $c$  with the speed of light in vacuum  $c_0$  *via*  $c = c_0/n$ , we can also interpret the situation as a time-of-flight measurement: All rays start at the same time, yet the rays close to the optical axis have to “wait” inside the lens (they travel slower in the dielectric by a factor of  $n$ ) for the rays further away to catch up, until they all meet at the same time at the focus. Lenses of this type, namely

---

<sup>1</sup>Note that throughout this thesis, figures without any citation and figures that only show a citation reference number [X] are the author’s original work or taken (or adapted) from the author’s published articles. Figures that are denoted with “taken from [X]” are taken from other work.

a homogeneous material that is put into a certain shape, have been known for centuries or even millenia [30]. The second type (shown on the right in Fig. 2.1) is more recent, yet it follows the same principle. A rectangular-shaped area is filled with an inhomogeneous medium, leading to a gradient in the refractive index (color-coded in blue). If we apply Fermat’s principle, the rays now follow curved paths inside the lens to fulfill the extremal constraint. These types of lenses are called gradient-index (GRIN) lenses. They are a simple example of optical materials influencing the geometry that light perceives – a large refractive index expands space, a small index compresses it.

Simply speaking, TO is a way of “reverse-engineering” Fermat’s principle. Where one would normally introduce materials into the light path and see how this changes the trajectory and therefore the perceived geometry of space, TO provides the tools to design the geometry of space, which leads to a tailored and desired light path, and then delivers the necessary optical material parameters to perform the task.

### 2.1.2. Mathematical Tools

The mathematical framework of TO is the same as the one on which Einstein’s general relativity is based: differential geometry and tensor analysis. The similarity is quite obvious, since both theories revolve around deformed space-time and coordinate transformations. Since we want to describe the propagation of light in arbitrary space-time geometries and, therefore, Maxwell’s equations in arbitrary coordinate systems, we have to introduce some of the necessary mathematical formalism here.

In this work, we use the Einstein summation convention

$$A^i B_i \equiv \sum_{i=1}^3 A^i B_i. \quad (2.3)$$

Latin indices refer to spatial coordinates and run from 1 to 3, so that  $x^i = \{x^1, x^2, x^3\}$ . It is convention to use Greek indices running from 0 to 3 to describe four-dimensional space-time, so that  $x^\mu = \{x^0, x^1, x^2, x^3\}$ . Here,  $x^0$  is the time coordinate (in Cartesian coordinates, it is  $x^0 = ct$ ). Furthermore, we depict all equations in SI units. Vector quantities are denoted with arrows and matrices are depicted in bold face.

Let us start by describing a coordinate transformation from an arbitrary set of coordinates  $\{x^i\}$  to a new set  $\{x^{i'}\}$ . Note that none of these sets has to be Cartesian. The differentials of these two sets are given by

$$dx^i = \frac{\partial x^i}{\partial x^{i'}} dx^{i'} \quad (2.4)$$

$$dx^{i'} = \frac{\partial x^{i'}}{\partial x^i} dx^i. \quad (2.5)$$

## 2. Transformation Optics

---

The transformation matrices which connect both coordinate systems in Eqs. (2.4) and (2.5) are the Jacobian matrices

$$J^i_{i'} = \frac{\partial x^i}{\partial x^{i'}} \quad (2.6)$$

$$J^{i'}_i = \frac{\partial x^{i'}}{\partial x^i}. \quad (2.7)$$

It is easy to prove that

$$J^i_{i'} J^{i'}_j = \delta^i_j \quad \text{or} \quad J^i_{i'} = \left( J^{i'}_i \right)^{-1}, \quad (2.8)$$

where  $\delta^i_j$  is the Kronecker delta or identity matrix. This simply means that the transformation matrix from  $\{x^i\} \rightarrow \{x^{i'}\}$  is the inverse of the backward transformation  $\{x^{i'}\} \rightarrow \{x^i\}$ .

The next thing we have to do is to measure distances in space. For simplicity, let us start in a Cartesian coordinate system  $\{x^i\} = \{x, y, z\}$ . For a measure of distance between two points in space, we need to describe an infinitesimally small step between  $x^i$  and  $x^i + dx^i$ . In Cartesian coordinates, this line element is given by

$$ds^2 = dx^2 + dy^2 + dz^2 = \delta_{ij} dx^i dx^j. \quad (2.9)$$

This is called the Euclidean form of the line element. It is important to mention that the value of the line element  $ds^2$  does not depend on the choice of coordinates – it is invariant under coordinate transformations. If we perform a transformation into an arbitrary system  $\{x^{i'}\}$  and replace the differentials in Eq. (2.9) by those in Eqs. (2.4), the line element reads

$$ds^2 = \delta_{ij} \frac{\partial x^i}{\partial x^{i'}} \frac{\partial x^j}{\partial x^{j'}} dx^{i'} dx^{j'} = \delta_{ij} J^i_{i'} J^j_{j'} dx^{i'} dx^{j'}. \quad (2.10)$$

Since the Jacobian matrices in Eq. (2.10) can be expressed in terms of the coordinates  $\{x^{i'}\}$  (and thus in a form that is free of Cartesian coordinates), we can now identify

$$ds^2 = g_{i'j'} dx^{i'} dx^{j'} \quad (2.11)$$

as the general form of the line element, independent of a special choice of the coordinate system. Here, we have substituted

$$g_{i'j'} = \delta_{ij} J^i_{i'} J^j_{j'}, \quad (2.12)$$

where the object  $g_{i'j'}$  is called the metric tensor. If we want to examine the transformation behavior of the metric, we should look at Eq. (2.11) in another arbitrary coordinate system  $\{x^i\}$ :

$$ds^2 = g_{ij} dx^i dx^j. \quad (2.13)$$

We can again compare Eqs. (2.11) and (2.13) and substitute the differentials in Eq. (2.13), so that

$$ds^2 = g_{ij} J^i_{i'} J^j_{j'} dx^{i'} dx^{j'}. \quad (2.14)$$

Therefore, the metric tensor transforms as

$$g'_{i'j'} = J^i_{i'} J^j_{j'} g_{ij}, \quad (2.15)$$

which, when written in matrix form, reads

$$\mathbf{g}' = \mathbf{J}^T \mathbf{g} \mathbf{J}. \quad (2.16)$$

Here,  $\mathbf{J}$  is the matrix with the elements  $J^i_{i'}$ . From Eq. (2.16) follows

$$g' = \det \mathbf{g}' = g(\det \mathbf{J})^2. \quad (2.17)$$

Without further technical proof, we state that the metric is a measure of space. For example, the volume element  $dV$  is given by

$$dV = \sqrt{g} d^3x. \quad (2.18)$$

In fact, the metric (in general) is not just a measure of space, but of space-time, since the spatial considerations that we did so far can easily be extended into four-dimensional space-time. The general line element and the space-time metric then follows as

$$ds^2 = g_{\mu\nu} dx^\mu dx^\nu. \quad (2.19)$$

Note that  $ds^2$  is still invariant under (Lorentz) transformations, it is a Lorentz scalar. If we restrict ourselves to Cartesian coordinates  $x^\mu = \{ct, x, y, z\}$ , the line element reads

$$ds^2 = -c^2 dt^2 + dx^2 + dy^2 + dz^2 = \eta_{\mu\nu} dx^\mu dx^\nu \quad (2.20)$$

with the Minkowski metric

$$\eta_{\mu\nu} = \text{diag}(-1, 1, 1, 1). \quad (2.21)$$

However, since transformations of four-dimensional space-time including the time coordinate are of little importance to this work, we will restrict ourselves to purely spatial transformations, if not stated otherwise.

### 2.1.3. Curvature of Space and the Nature of Geodesics

In TO, we obviously deal with transformations of space, and sometimes the terms “curved space” and “stretched or distorted space” are used as synonyms. Let us examine the meaning of curvature of space a bit more closely. As we have introduced before, the metric tensor  $g_{ij}$  is a measure of the geometry of space. The definition of curvature is the following: if a coordinate system can be found in which the line element  $ds^2$  takes the Euclidean form (2.9), then the space is flat. If such coordinates do not exist, we call the space curved. The meaning of this definition is best grasped when it is accompanied by an example. For simplicity (and for the sake of the imagination capabilities of the human

mind), let us reduce the spatial dimensions and consider two-dimensional sheets embedded in a three-dimensional space.

In the beginning, imagine the basic transformation from Cartesian coordinates  $\{x, y, z\}$  to cylindrical coordinates  $\{r, \theta, z\}$ . The resulting line element reads

$$ds^2 = dr^2 + r^2 d\theta^2 + dz^2. \quad (2.22)$$

If we fix the radius at  $r = a$ , the result is a sheet that is rolled up into a cylinder. Since  $dr = 0$ , the corresponding line element follows as

$$ds^2 = a^2 d\theta^2 + dz^2 = (d(a\theta))^2 + dz^2, \quad (2.23)$$

which has the Euclidean form (2.9). This result might be surprising, since the surface of the cylinder in three-dimensional space is obviously curved. Yet, this curvature can only be “observed” from the higher-dimensional embedding space, not from beings that live on the surface of the cylinder. This kind of curvature is called “extrinsic” curvature [31] and we won’t concern ourselves with it here. More importantly, we want to analyze what is called the “intrinsic” curvature of space. A mathematician on the cylinder-world could perfectly be named Euclid and find exactly the same theorems which he found in our world. The curvature of the cylinder is zero, its space is flat.

As a second example, let us consider spherical coordinates  $\{r, \theta, \phi\}$ . Here, the line element is

$$ds^2 = dr^2 + r^2 d\theta^2 + r^2 \sin^2 \theta d\phi^2. \quad (2.24)$$

If we again fix the radius at  $r = a$ , we have formed a spherical surface. The line element on this surface is

$$ds^2 = a^2 d\theta^2 + a^2 \sin^2 \theta d\phi^2. \quad (2.25)$$

Without technical proof, we state that there is no transformation to coordinates in which this line element takes the Euclidean form. A spherical surface has a non-zero curvature and is therefore non-Euclidean. It is noteworthy that the two aforementioned examples do *not* mean that cylindrical coordinates describe flat space and spherical coordinates describe curved space. By fixing the radius, we have created two-dimensional subspaces, and these are flat or curved, respectively.

The curvature of space is important for the way in which light propagates. Remembering Fermat’s principle (see Section 2.1.1), light travels on stationary paths and chooses the shortest (optical) connection between two points. In flat space, these connections are straight lines. In curved space, we can still construct the shortest line between two points, yet it will be curved and we call it a “geodesic”. For our example of the sphere, the geodesics are the circles whose centers coincide with the center of the sphere. They are called great circles. In general, we can derive the “geodesic equation”, which describes geodesics in arbitrary spaces and coordinates  $\{x^i\}$ . The equation for a light trajectory  $x^i(s)$  reads

$$\frac{d^2 x^i(s)}{ds^2} + \Gamma^i_{jk} \frac{dx^j(s)}{ds} \frac{dx^k(s)}{ds} = 0, \quad (2.26)$$

where  $s$  is used for parameterization and  $\Gamma^i_{jk}$  are the Christoffel symbols of the second kind given by

$$\Gamma^i_{jk} = \frac{g^{il}}{2} \left( \frac{\partial g_{lj}}{\partial x^k} + \frac{\partial g_{lk}}{\partial x^j} - \frac{\partial g_{jk}}{\partial x^l} \right). \quad (2.27)$$

If we examine the Christoffel symbols more closely, we see that they are given by the first-order partial derivatives of the metric. In Einstein’s general relativity, these symbols take the role of Newton’s gravitational force and they describe the movement of a particle in a gravitational field without any further external forces. Note that for the Euclidean metric  $g_{ij} = \delta_{ij}$ , the Christoffel symbols vanish. In this case, Eq. (2.26) reduces to

$$\frac{d^2 x^i(s)}{ds^2} = 0, \quad (2.28)$$

and the solutions are straight lines  $x^i(s) = a^i + sb^i$ , with  $a^i$  and  $b^i$  being constants. We verify that light (which always follows geodesics) travels in straight lines in a flat space, *i.e.*, a Euclidean metric. The Christoffel symbols also constitute another – and maybe the most important – object in geometry: the Riemann curvature tensor. It is given by

$$R^i_{jkl} = \frac{\partial \Gamma^i_{jl}}{\partial x^k} - \frac{\partial \Gamma^i_{jk}}{\partial x^l} + \Gamma^i_{mk} \Gamma^m_{jl} - \Gamma^i_{ml} \Gamma^m_{jk}. \quad (2.29)$$

It is easy to see that the Riemann curvature tensor is solely a function of the metric and its first-order and second-order partial derivatives. Consequently, it only depends on the geometry of space(-time) itself. It quantifies the geodesic deviation, which is the change of the rate of two “parallel” lines’ separation. Therefore, it is a measure of the curvature of space(-time) itself. Furthermore, it can be contracted to form the Riemann invariant (or curvature scalar), which is a coordinate-invariant measure of space(-time) curvature. We have found another way of defining curved space: if the Riemann curvature tensor vanishes, the space is flat. Otherwise, it is curved.

On a side note, we want to add that Riemannian manifolds, with which we deal here, are always “locally flat”. This means that, in general, one can always find a suitable coordinate system for which the metric is Euclidean *at any one point*, but *only* in that point. Therefore, also the Christoffel symbols vanish at this point. If one moves away from the point, they again become non-trivial. Importantly, the second-order derivatives generally do *not* vanish at this point, showing that the Riemann tensor really is a measure of curvature.

With regard to TO, we want to emphasize that a large part of the used transformations are coordinate transformations that map within Euclidean space. Therefore, the spaces involved should not be denoted as *curved*. However, it is noteworthy that the term “curved” is often used in the literature when dealing with TO, and in these cases it should be considered having the meaning of a general deformation of space, and not a strict mathematical curvature. Furthermore, there are classes of transformations which include truly curved spaces and non-Euclidean geometries [25, 26, 32].

### 2.1.4. Deriving Optical Parameters from Geometries

After introducing the necessary mathematical tools, let us now explore the actual potency of TO: How can we derive optical parameters for a transformation medium from a given coordinate transformation with a corresponding light trajectory?

Let us start with Maxwell's equations in Cartesian coordinates and in empty flat space [33]:

$$\nabla \cdot \vec{E} = \frac{\rho}{\varepsilon_0} \quad (2.30)$$

$$\nabla \cdot \vec{B} = 0 \quad (2.31)$$

$$\nabla \times \vec{E} = -\frac{\partial \vec{B}}{\partial t} \quad (2.32)$$

$$\nabla \times \vec{B} = \frac{1}{c_0^2} \frac{\partial \vec{E}}{\partial t} + \mu_0 \vec{j}. \quad (2.33)$$

Our task is to write Maxwell's equations in arbitrary coordinates. For this, we need a general expression for the divergence and the curl in arbitrary coordinates. For any vector  $\vec{V}$ , these expressions are (for technical proof, see for example Ref. [26]):

$$\nabla \cdot \vec{V} = \frac{1}{\sqrt{g}} \frac{\partial(\sqrt{g}V^i)}{\partial x^i} \quad (2.34)$$

$$(\nabla \times \vec{V})^i = \epsilon^{ijk} \frac{\partial V_k}{\partial x^j}. \quad (2.35)$$

Here, we have used again  $g = \det \mathbf{g}$  and the antisymmetric Levi-Civita tensor

$$\epsilon^{ijk} = \pm \frac{1}{\sqrt{g}} [ijk], \quad (2.36)$$

where  $[ijk]$  is the permutation symbol

$$[ijk] = \begin{cases} +1 & , \text{ if } ijk \text{ is an even permutation of } 123, \\ -1 & , \text{ if } ijk \text{ is an odd permutation of } 123, \\ 0 & \text{ otherwise.} \end{cases} \quad (2.37)$$

Note that the  $\pm$ -sign in Eq. (2.36) reflects the fact that transformations can change the handedness of the coordinate system (-), or leave it as it is (+). Using Eqs. (2.34), (2.35), and the fact that the magnetic induction in empty space is simply  $\vec{B} = \mu_0 \vec{H}$ , we write

Maxwell's equations as

$$\frac{1}{\sqrt{g}} \frac{\partial(\sqrt{g}E^i)}{\partial x^i} = \frac{\rho}{\epsilon_0} \quad (2.38)$$

$$\frac{1}{\sqrt{g}} \frac{\partial(\sqrt{g}H^i)}{\partial x^i} = 0 \quad (2.39)$$

$$\epsilon^{ijk} \frac{\partial E_k}{\partial x^j} = -\mu_0 \frac{\partial H^i}{\partial t} \quad (2.40)$$

$$\epsilon^{ijk} \frac{\partial H_k}{\partial x^j} = -\epsilon_0 \frac{\partial E^i}{\partial t} + j^i. \quad (2.41)$$

So far, we have only defined Maxwell's equations in flat space, albeit in arbitrary coordinates. If we remember the statement about *local* flatness of curved spaces in Section 2.1.3, we come to the conclusion that Maxwell's equations in the form (2.38)-(2.41) are also valid in arbitrary geometries. The argument is that we can regard curved space as a patchwork of locally flat pieces of space. On each individual piece we can define Maxwell's equations, therefore they also hold globally. If they hold globally, we can lose the constraint that the metric  $g_{ij}$  used here is the Euclidean one, in fact it can be arbitrary.

To advance towards our goal of connecting the geometry of space and material parameters, let us perform some "index gymnastics" and rearrangements on Eqs. (2.38)-(2.41). If we lower the indices of all vectors *via*  $g^{ji}V_i = V^j$  and use Eq. (2.36), we get

$$\frac{\partial(\epsilon_0\sqrt{g}g^{ij}E_j)}{\partial x^i} = \sqrt{g}\rho \quad (2.42)$$

$$\frac{\partial(\sqrt{g}g^{ij}H_j)}{\partial x^i} = 0 \quad (2.43)$$

$$[ijk] \frac{\partial E_k}{\partial x^j} = -\frac{\partial(\pm\mu_0\sqrt{g}g^{ij}H_j)}{\partial t} \quad (2.44)$$

$$[ijk] \frac{\partial H_k}{\partial x^j} = \frac{\partial(\pm\epsilon_0\sqrt{g}g^{ij}E_j)}{\partial t} \pm \sqrt{g}j^i. \quad (2.45)$$

Let us bear this form of Maxwell's equations in empty space but arbitrary geometries in mind and introduce the *macroscopic* Maxwell equations in dielectric media [33]:

$$\nabla \cdot \vec{D} = \varrho \quad (2.46)$$

$$\nabla \cdot \vec{B} = 0 \quad (2.47)$$

$$\nabla \times \vec{E} = -\frac{\partial \vec{B}}{\partial t} \quad (2.48)$$

$$\nabla \times \vec{H} = \frac{\partial \vec{D}}{\partial t} + \vec{J}. \quad (2.49)$$

As a final step, let us also rewrite the *macroscopic* Maxwell equations (2.46)-(2.49) in an arbitrary coordinate system  $\{x^i\}$ , where we denote the metric of this system by  $\gamma_{ij}$  and its determinant simply by  $\gamma$ . This gives us the freedom to describe the problem that is to be solved in a suitable coordinate system (*e.g.*, cylindrical coordinates), depending on the symmetry of the problem. The equations then read

$$\frac{\partial\sqrt{\gamma}D^i}{\partial x^i} = \sqrt{\gamma}\varrho \quad (2.50)$$

$$\frac{\partial\sqrt{\gamma}B^i}{\partial x^i} = 0 \quad (2.51)$$

$$[ijk]\frac{\partial E_k}{\partial x^j} = -\frac{\partial\sqrt{\gamma}B^i}{\partial t} \quad (2.52)$$

$$[ijk]\frac{\partial H^k}{\partial x^j} = \frac{\partial\sqrt{\gamma}D^i}{\partial t} + \sqrt{\gamma}J^i. \quad (2.53)$$

We have now arrived at the very essence and the core idea of TO. By comparing equation set (2.42)-(2.45) (Maxwell's equations in empty space but arbitrary geometries) with equation set (2.50)-(2.53) (macroscopic Maxwell equations in a medium), we see that they bare exactly the same form. We simply have to rescale the charge and current densities by

$$\varrho = \pm\frac{\sqrt{g}}{\sqrt{\gamma}}\rho \quad (2.54)$$

$$J^i = \pm\frac{\sqrt{g}}{\sqrt{\gamma}}j^i, \quad (2.55)$$

and derive the important relationship

$$D^i = \pm\varepsilon_0\frac{\sqrt{g}}{\sqrt{\gamma}}g^{ij}E_j \quad (2.56)$$

$$B^i = \pm\mu_0\frac{\sqrt{g}}{\sqrt{\gamma}}g^{ij}H_j. \quad (2.57)$$

We know the connection of  $\vec{D}$  and  $\vec{E}$  ( $\vec{B}$  and  $\vec{H}$ ) in a medium:

$$D^i = \varepsilon_0\varepsilon^{ij}E_j \quad (2.58)$$

$$B^i = \mu_0\mu^{ij}H_j. \quad (2.59)$$

By comparing Eqs. (2.56) and (2.57) with Eqs. (2.58) and (2.59), respectively, we can finally deduce the fundamental connection between the geometry of space and material parameters:

$$\varepsilon^{ij} = \mu^{ij} = \pm\frac{\sqrt{g}}{\sqrt{\gamma}}g^{ij}. \quad (2.60)$$

Let us bear the fundamental equation (2.60) in mind and elaborate on the interpretation of the transformation procedure. We want to introduce the terms “physical” and “virtual” space. Physical space is the space in which we live, it is flat in the Euclidean sense. Nevertheless, we can describe this very same space using different coordinate grids, which means we can choose an arbitrary set of coordinates  $\{x^i\}$ . We denote the metric that corresponds to a specific set of coordinates with  $\gamma_{ij}$ . Furthermore, we can introduce media in this space. This physical space is described by the *macroscopic* Maxwell equations (2.50)-(2.53). We can now imagine a (hypothetical) virtual space, which is empty. This space is described by a coordinate set  $\{x^{i'}\}$  with a corresponding metric  $g_{i'j'}$ . In the beginning, both virtual and physical space are identical. This means that the components of the metric tensors  $\gamma_{ij}$  and  $g_{i'j'}$  are the same when  $\{x^i\}$  and  $\{x^{i'}\}$  are interchanged. We now perform a non-trivial coordinate transformation in virtual space with the relation  $x^{i'} = x^{i'}(x^j)$ , which gives us a metric  $g_{ij}$ . Since we are still in empty space, the corresponding Maxwell equations are given by (2.42)-(2.45). Again, the core idea of TO is to apply a coordinate transformation in (empty) virtual space and reinterpret the resulting metric as the constituting parameters of the effective medium in physical space.

To complete the task that we have set, let us now write the inverse metric  $g^{ij}$  in Eq. (2.60) in terms of the inverse metric  $g^{i'j'}$  of virtual space:

$$\varepsilon^{ij} = \mu^{ij} = \pm \frac{\sqrt{g}}{\sqrt{\gamma}} g^{i'j'} J^i_{i'} J^j_{j'}. \quad (2.61)$$

Remembering the matrix notation of the transformation of the metric in Eq. (2.16), taking the determinant of it in Eq. (2.17), and finally taking the square root of this determinant, we arrive at

$$\sqrt{g'} = \sqrt{g} |\det \mathbf{J}|. \quad (2.62)$$

With this, we eliminate  $\sqrt{g}$  from Eq. (2.61). Subsequently, we write Eq. (2.61) in matrix form, where we can remove the  $\pm$ -sign and the absolute value sign of  $|\det \mathbf{J}|$ , since the sign of  $\det \mathbf{J}$  is a measure of the handedness for itself. The final result is

$$\boldsymbol{\varepsilon} = \boldsymbol{\mu} = \frac{\sqrt{g'}}{\sqrt{\gamma}} \mathbf{J}(\mathbf{g}')^{-1} \mathbf{J}^T. \quad (2.63)$$

This equation is the “cooking recipe” that TO provides in order to relate arbitrary coordinate transformations and their corresponding metrics with material parameters of actual media in the physical world.

There is one last hurdle to be taken. In general, the components of the material tensor  $\varepsilon^{ij}$  change upon changing the coordinate system in physical space, and so do the eigenvalues of the tensor. We want to find the principal values  $\varepsilon_l$  of those tensors. They point along a triad of eigenvectors (the principal axes) in the respective coordinate system and, importantly, have the same value in all coordinate systems. Without technical proof, we state that the

eigenvalues of the tensor  $\varepsilon^i_j$  are those wanted principal values. To get this tensor, we have to lower an index *via*

$$\varepsilon^i_j = \varepsilon^{ik} \gamma_{kj}. \quad (2.64)$$

In matrix notation, we simply multiply the metric  $\gamma$  with the matrix  $\varepsilon$  to get the desired material tensor

$$\varepsilon^* = \boldsymbol{\mu}^* = \gamma \varepsilon, \quad (2.65)$$

where the matrix  $\varepsilon^*$  is given by the tensor  $\varepsilon^i_j$  and the matrix  $\boldsymbol{\mu}^*$  by  $\mu^i_j$ .

As a last step, we want to add that we are not bound to start our transformation in *empty* flat virtual space. In fact, one can even start in an anisotropic medium with complex-valued parameters [34]. But if we start in a space that is filled with an isotropic homogeneous medium with a (scalar and real) permittivity  $\varepsilon_{\text{ref}}$  and permeability  $\mu_{\text{ref}}$ , Eq. (2.65) is simply modified to

$$\varepsilon^* = \gamma \varepsilon \varepsilon_{\text{ref}} \quad (2.66)$$

$$\boldsymbol{\mu}^* = \gamma \boldsymbol{\mu} \mu_{\text{ref}} \quad (2.67)$$

This introduces another scaling freedom into the formalism of TO, which will become important later on. Note that although the permittivity and permeability tensors are still proportional to each other, their eigenvalues differ by a factor of  $\mu_{\text{ref}}/\varepsilon_{\text{ref}}$  from each other.

All of the above considerations clearly show the symmetry of Maxwell's equations with respect to the electric and magnetic field. Therefore, it is no surprise to see that the permittivity tensor  $\varepsilon^{ij}$  and the permeability tensor  $\mu^{ij}$  necessarily have to be equal to each other in all components (for a transformation that starts in empty space). Equation (2.63) clearly shows that geometries of space manifest themselves as material parameters and optical materials establish a geometry for light. It is also clear that transformation media of this kind are always impedance-matched to vacuum (to the medium in the virtual space), since the impedance  $Z$  is always unity for  $\varepsilon = \boldsymbol{\mu}$  (equal to the impedance of the medium in virtual space). For simplicity, the vacuum impedance  $Z_0 \approx 376.7 \Omega$  is set to unity throughout this work. We have thus established how geometries of space appear (in general) as anisotropic impedance-matched media.

### Space-Time Transformations and Their Implications

Throughout this thesis, we restrict ourselves to purely spatial transformations. However, we want to show here that the formalism of TO also works for four-dimensional space-time geometries. The free-space Maxwell equations in an arbitrary space-time geometry can be shown to be equivalent to the macroscopic Maxwell equations in Cartesian coordinates.

Flat space is described by the Minkowski metric (2.21) and a general metric by  $g_{\alpha\beta}$ . Note that the determinant of the metric is negative due to the different signature of space and time.

For a coordinate-invariant (covariant) form of Maxwell's equations, we use the electromagnetic field tensor  $F_{\mu\nu}$ , which in terms of the fields  $\vec{E}$  and  $\vec{B}$  is given by

$$F_{\mu\nu} = \begin{bmatrix} 0 & -E_1 & -E_2 & -E_3 \\ E_1 & 0 & cB_3 & -cB_2 \\ E_2 & -cB_3 & 0 & cB_1 \\ E_3 & cB_2 & -cB_1 & 0 \end{bmatrix}. \quad (2.68)$$

In free space, Maxwell's equations [26, 31] read

$$\frac{\partial F_{\mu\nu}}{\partial x^\lambda} + \frac{\partial F_{\nu\lambda}}{\partial x^\mu} + \frac{\partial F_{\lambda\mu}}{\partial x^\nu} = 0 \quad (2.69)$$

$$\frac{\varepsilon_0}{\sqrt{-g}} \frac{\partial(\sqrt{-g}F^{\mu\nu})}{\partial x^\nu} = j^\mu, \quad (2.70)$$

where  $j^\mu = (\rho, j^i/c)$  is the four-current. Now, we have to match the form of Eqs. (2.69)-(2.70) with the macroscopic Maxwell equations. If a quantity  $H^{\mu\nu}$  is defined by

$$H^{\mu\nu} = \varepsilon_0 \sqrt{-g} F^{\mu\nu}, \quad (2.71)$$

we can drop the indices of  $F^{\mu\nu}$  by

$$H^{\mu\nu} = \varepsilon_0 \sqrt{-g} g^{\mu\lambda} g^{\nu\rho} F_{\lambda\rho} \quad (2.72)$$

and therefore

$$F_{\mu\nu} = \frac{1}{\varepsilon_0 \sqrt{-g}} g_{\mu\lambda} g_{\nu\rho} H^{\lambda\rho}. \quad (2.73)$$

If we regard  $H^{\mu\nu}$  depending on the fields  $\vec{D}$  and  $\vec{H}$  as

$$H^{\mu\nu} = \begin{bmatrix} 0 & D^1 & D^2 & D^3 \\ -D^1 & 0 & H^3/c & -H^2/c \\ -D^2 & -H^3/c & 0 & H^1/c \\ -D^3 & H^2/c & -H^1/c & 0 \end{bmatrix}. \quad (2.74)$$

and rescale the four-current by  $J^\mu = \sqrt{-g} j^\mu$ , the free-space equations read as

$$\frac{\partial F_{\mu\nu}}{\partial x^\lambda} + \frac{\partial F_{\nu\lambda}}{\partial x^\mu} + \frac{\partial F_{\lambda\mu}}{\partial x^\nu} = 0 \quad (2.75)$$

$$\frac{\partial H^{\mu\nu}}{\partial x^\nu} = J^\mu. \quad (2.76)$$

Note that in this equation,  $F_{\mu\nu}$  has the form (2.73). Equations (2.75) and (2.76) now have the form of the macroscopic Maxwell equations in right-handed Cartesian coordinates.

From this, we can derive the constitutive equations in matrix form (for technical proofs, we refer the reader to the book of Leonhardt and Philbin [26]):

$$\vec{D} = \varepsilon_0 \boldsymbol{\varepsilon} \vec{E} + \frac{1}{c} \vec{w} \times \vec{H} \quad (2.77)$$

$$\vec{B} = \mu_0 \boldsymbol{\mu} \vec{H} - \frac{1}{c} \vec{w} \times \vec{E}. \quad (2.78)$$

Here, the vector  $\vec{w}$  is given by

$$w_i = \frac{g_{0i}}{g_{00}} \quad (2.79)$$

and, importantly, the optical parameters read

$$\varepsilon^{ij} = \mu^{ij} = -\frac{\sqrt{-g}}{g_{00}} g^{ij}. \quad (2.80)$$

It is interesting to see that for a non-vanishing vector  $\vec{w}$  (which has the physical dimension of a velocity here), the electric and magnetic fields are mixing. This is the case when the geometry mixes spatial and temporal components, *i.e.*,  $g_{0i} \neq 0$ . Therefore, a space-time geometry manifests itself as a magneto-electric medium, or in other words, a *moving* medium. This becomes apparent when we consider that Lorentz transformations mix electric and magnetic fields in a moving frame of reference [33]. From a different perspective, a moving dielectric medium can implement a four-dimensional space-time geometry [35].

## Considerations for the Magnetic Response

As we have seen, performing a transformation on empty space necessarily yields identical values for the permittivity  $\boldsymbol{\varepsilon}$  and the permeability  $\boldsymbol{\mu}$ , all tensor components are equal to each other. This is not a problem for any theoretical design of a device. But when it comes to an experimental realization of the optical parameters, this issue turns out to be one of the largest yet unsolved problems, especially at optical frequencies. No material in nature exhibits a magnetic response at such high frequencies. Therefore, a metamaterial with a substructure has to be tailored to create the magnetic response. This is possible for microwave frequencies, but it becomes very hard to implement such a substructure into the often times very demanding layouts of transformation optical devices at optical frequencies. However, if we restrict ourselves to two-dimensional geometries, there is a workaround for this problem, and it often serves the purpose very good. Let us examine this case by looking at the electromagnetic wave equations in a dielectric medium with permittivity  $\boldsymbol{\varepsilon}$  and permeability  $\boldsymbol{\mu}$ . We will describe the propagation in a Cartesian coordinate system, where a plane wave travels in the  $xy$ -plane with the wave vector pointing in the  $x$ -direction. For the two linear polarizations of light, TE (electric field

along the  $z$ -axis) and TM (magnetic field along the  $z$ -axis), the wave equations for the electric field read

$$\left( \Delta - \frac{\varepsilon_z \mu_y}{c_0^2} \frac{\partial^2}{\partial t^2} \right) \vec{E} = 0 \quad \text{for TE} \quad (2.81)$$

$$\left( \Delta - \frac{\varepsilon_y \mu_z}{c_0^2} \frac{\partial^2}{\partial t^2} \right) \vec{E} = 0 \quad \text{for TM.} \quad (2.82)$$

It is obvious that the propagation of the electromagnetic wave is governed by the product of the corresponding principal values  $\varepsilon_i \mu_j$ . If a second medium can be found with different optical parameters  $\boldsymbol{\varepsilon}'$  and  $\boldsymbol{\mu}'$ , which yields the same product  $\varepsilon_i \mu_j = \varepsilon'_i \mu'_j$  in every point in space and time, the wave cannot differentiate between them and propagates in exactly the same fashion in both media. However, this use of so-called “reduced parameters” can in general only work for one polarization of light.

To clarify this, let us first consider the TM case assuming that the complete magnetic response vanishes, as desired. We can define the new response functions  $\varepsilon'_y = \varepsilon_y \mu_z$  and  $\mu'_z = 1$  without changing their product (for a wave traveling in the  $y$ -direction, it would be  $\varepsilon'_x = \varepsilon_x \mu_z$ ). The TM-polarized wave will behave exactly the same as before. However, in the case of the TE-polarized wave, the new response function would have to be  $\varepsilon'_z = \varepsilon_z \mu_y$  with  $\mu'_y = 1$  for wave propagation in  $x$ -direction, or  $\varepsilon'_z = \varepsilon_z \mu_x$  with  $\mu'_x = 1$  for wave propagation in  $y$ -direction. Both terms can (in general) only be true simultaneously when  $\mu_x = \mu_y$ , which means that the ideal (non-reduced) parameters were isotropic in the propagation plane in the first place. This is generally not the case for arbitrary transformations, which limits this approach to one polarization. However, devices based on isotropic transformations, such as (quasi-)conformal transformations, can be free of a magnetic response using reduced parameters.

In three dimensions, where we also have to consider wave propagation out of the plane, the above argument implies that the material has to be completely isotropic, drastically narrowing down the number of useful transformations. However, if a locally isotropic three-dimensional device *can* be designed, it should be independent of the polarization.

Although applicable in some cases, there is another drawback to the procedure of “reducing parameters”. An important property of the medium is changed along with the rescaling of the parameters – the impedance  $Z$ . The impedance in both media (in the TM-polarized case) reads

$$Z = \sqrt{\frac{\mu_z}{\varepsilon_y}} \quad (2.83)$$

$$Z' = \sqrt{\frac{\mu'_z}{\varepsilon'_y}} = \sqrt{\frac{1}{\varepsilon_y \mu_z}}. \quad (2.84)$$

The first medium is impedance-matched to free space, as are all transformation media that are derived directly from a spatial coordinate transformation (starting in empty virtual space). Thus, it shows no Fresnel reflections at the interface. The second medium, however, obviously shows a different impedance  $Z' \neq 1$ . Fresnel reflections at the interface of the transformation medium are the price to pay for using a non-magnetic material. Often, these reflections can be neglected or do not disturb the functionality of the device too much. Yet, they have to be born in mind.

### 2.1.5. Exemplary Transformation Procedure

To clarify the calculation of optical parameters from a coordinate transformation, let us explicitly perform the complete transformation procedure step by step at a well-known simple example: a cylindrical cloak [21]. For further insight into this structure and to test its experimental feasibility, this cloak has also been studied numerically during the course of this thesis (see Appendix A.1). In the case of a cylindrical cloak, it is self-evident to use coordinates that reflect the symmetry. This simplifies the calculations and representations drastically. Figure 2.2 illustrates the general concept of the transformation.

Let us start in physical space. Here, we choose cylindrical coordinates  $\{r, \theta, z\}$  with the corresponding metric  $\gamma_{ij}$ . The metric of a cylindrical coordinate system can easily be derived, or we can simply look at the line element  $ds^2$  in Eq. (2.22), since the pre-factors of the differentials make up the components of the metric tensor. The metric reads

$$\boldsymbol{\gamma} = \begin{bmatrix} 1 & 0 & 0 \\ 0 & r^2 & 0 \\ 0 & 0 & 1 \end{bmatrix}. \quad (2.85)$$

The determinant of this metric is

$$\det \boldsymbol{\gamma} = \gamma = r^2. \quad (2.86)$$

Let us now turn to virtual space, where we choose cylindrical coordinates  $\{r', \theta', z'\}$  and the corresponding metric  $g_{i'j'}$ . Note that the metric is the same as in physical space, except that  $\{x^i\} \leftrightarrow \{x^{i'}\}$ . Therefore, it reads

$$\boldsymbol{g}' = \begin{bmatrix} 1 & 0 & 0 \\ 0 & r'^2 & 0 \\ 0 & 0 & 1 \end{bmatrix} \quad (2.87)$$

with the determinant

$$\det \boldsymbol{g}' = g' = r'^2. \quad (2.88)$$

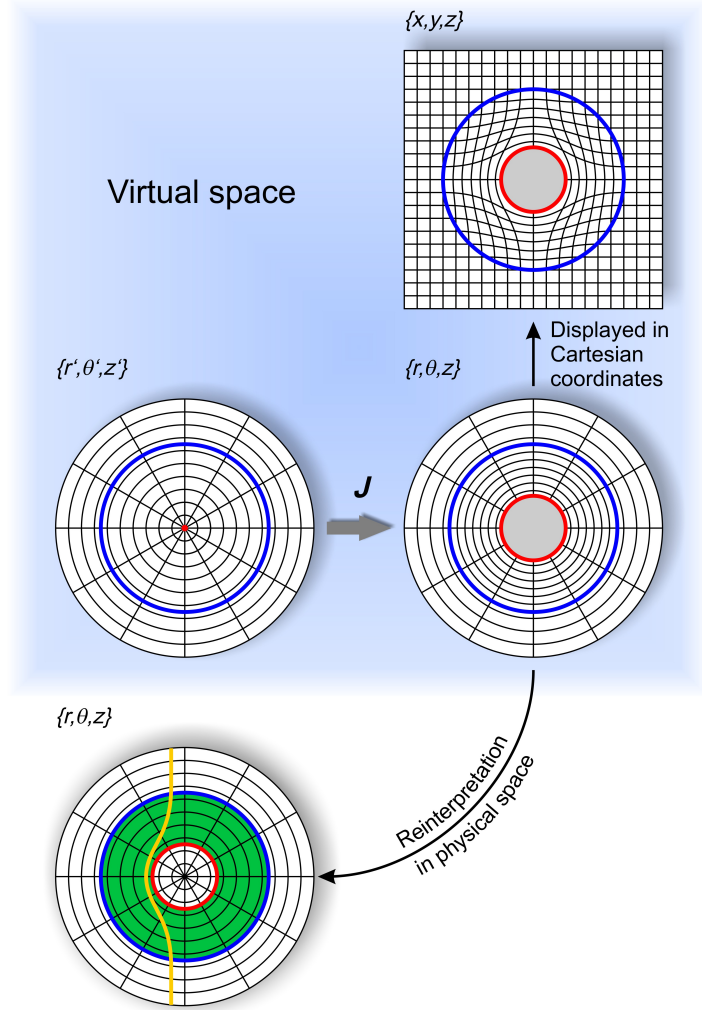


**Figure 2.2.:** Derivation of the optical parameters for the cylindrical invisibility cloak. In *virtual* empty space (blue area), a transformation with the Jacobian matrix  $\mathbf{J}$  is performed to transform from cylindrical coordinates  $\{r', \theta', z'\}$  to a new set of coordinates  $\{r, \theta, z\}$ . Here, the origin (red dot) has been expanded to a circle with radius  $a$  (red circle) and the surrounding medium has been compressed. The blue circle with radius  $b$  is mapped onto itself and forms the outer interface of the cloak. Note the gray area in the middle. An object that is placed here cannot interact with light from outside. This is better visualized when the transformed space is displayed in a Cartesian coordinate system (top). The geodesics (and thus the light trajectories) “flow” around the inner core. The metric of the transformed system is then reinterpreted as constituting the material parameters in *physical* space (bottom). A medium with these parameters (shown in green) acts on the light in the same way as the geometry of empty transformed space. An exemplary light trajectory is depicted in yellow.

The inverse matrix of  $\mathbf{g}'$  is easily calculated as

$$(\mathbf{g}')^{-1} = \begin{bmatrix} 1 & 0 & 0 \\ 0 & \frac{1}{r'^2} & 0 \\ 0 & 0 & 1 \end{bmatrix} \quad (2.89)$$

In virtual space, we perform a transformation of the radial coordinate which maps a circle with radius  $r' = b$  onto itself and the origin at  $r' = 0$  onto a circle with radius  $r = a$ . In other words, we compress a disc into a shell. The simplest transformation is a linear one and reads

$$r = \frac{b-a}{b}r' + a \quad (2.90)$$

$$\theta = \theta' \quad (2.91)$$

$$z = z' \quad (2.92)$$

with the corresponding Jacobian matrix  $J_{\nu}^i$  given by

$$\mathbf{J} = \begin{bmatrix} \frac{b-a}{b} & 0 & 0 \\ 0 & 1 & 0 \\ 0 & 0 & 1 \end{bmatrix}. \quad (2.93)$$

The determinant of this Jacobian is simply

$$\det \mathbf{J} = \frac{b-a}{b}. \quad (2.94)$$

Since the Jacobian matrix is diagonal in this case, its transpose matrix is identical to it, so  $\mathbf{J} = \mathbf{J}^T$ . We have all ingredients for the recipe and can now start “cooking”. Inserting Eqs. (2.86), (2.88), (2.89), (2.93), and (2.94) into Eq. (2.63), we derive the optical parameters as

$$\boldsymbol{\varepsilon} = \boldsymbol{\mu} = \begin{bmatrix} \frac{(b-a)r'}{br} & 0 & 0 \\ 0 & \frac{b}{(b-a)rr'} & 0 \\ 0 & 0 & \frac{br'}{(b-a)r} \end{bmatrix}. \quad (2.95)$$

We have to remember to lower one index of  $\varepsilon^{ij}$ , since we are in a non-Cartesian coordinate system and, therefore,  $\boldsymbol{\gamma}$  is *not* the unit matrix. The result for the material parameters is

$$\boldsymbol{\varepsilon}^* = \boldsymbol{\mu}^* = \boldsymbol{\gamma}\boldsymbol{\varepsilon} = \begin{bmatrix} \frac{(b-a)r'}{br} & 0 & 0 \\ 0 & \frac{br}{(b-a)r'} & 0 \\ 0 & 0 & \frac{br'}{(b-a)r} \end{bmatrix} \quad (2.96)$$

Of course, we want to display the result in the coordinates  $\{r, \theta, z\}$  of the physical system in which we (and the transformation medium) are situated. Using Eqs. (2.90)-(2.92), we get the final result

$$\boldsymbol{\varepsilon}^* = \boldsymbol{\mu}^* = \begin{bmatrix} \frac{r-a}{r} & 0 & 0 \\ 0 & \frac{r}{r-a} & 0 \\ 0 & 0 & \left(\frac{b}{b-a}\right)^2 \frac{r-a}{r} \end{bmatrix}. \quad (2.97)$$

Note that these optical parameters are singular, *i.e.*, they go to zero and infinity, respectively. As stated in the introduction, the Jacobian matrix (which is the main “ingredient” for the derived optical parameters) is directly connected to the transformation and is a purely mathematical entity with no physical constraints. This leads to the possibility of such singularities. An implication of this fact will be discussed in the next section.

With regard to the considerations of curvature that we made in Section 2.1.3, it should be noted that this transformation, although curvilinear coordinates are involved, is *not* accompanied by any curvature of space itself. If one calculates the Riemann curvature tensor, one finds that it is actually zero and the space is intrinsically flat.

### 2.1.6. Considerations on Dispersion and Superluminal Propagation

In this section, we want to comment on some (possibly problematic) properties of the TO approach, and we will shed some light on the dispersion characteristics of transformation devices. Although we have treated TO only for an empty virtual space or a virtual space containing an isotropic lossless dielectric so far, the approach is capable of treating anisotropic media in virtual space without problems [34]. In the case of dispersive media, however, the transformation procedure can only be considered to be valid for one frequency or a narrow frequency band [34].

To clarify this last statement, let us consider an example. Since we are already familiar with the cylindrical cloak, we will use its higher-dimensional “brother”, the spherical cloak, as an example. For this cloak, the idea is similar, namely inflating a point into a sphere with a proper transformation. Here, the material parameters [21] in spherical coordinates  $\{r, \theta, \phi\}$  are

$$\varepsilon_r = \mu_r = \frac{b}{b-a} \frac{(r-a)^2}{r} \quad (2.98)$$

$$\varepsilon_\theta = \mu_\theta = \frac{b}{b-a} \quad (2.99)$$

$$\varepsilon_\phi = \mu_\phi = \frac{b}{b-a}. \quad (2.100)$$

Let us first consider the case of a monochromatic plane wave traveling through this cloak, and let us assume that we are in a medium without dispersion. From the parameters, we can directly see that the radial component of the phase velocity  $v_{\text{ph}}$  is constant [36]. It is also clear that both angular phase velocities tend to infinity when the inner radius  $a$  is approached. This makes sense when we consider that the inner sphere at radius  $a$  originated in a single mathematical point, and the time that a wave takes to cross a point is zero. Consequently, the phase at the complete inner sphere is constant. This is no contradiction to relativity or causality, since a superluminal phase velocity does not mean that energy or information is transported at superluminal speeds [37]. In fact, a plane

wave cannot transport any kind of information, since it exists for all times and occupies the complete space by definition. With the same argument, a plane wave is not capable of transmitting energy at superluminal speeds, although its phase advances faster than the speed of light in vacuum. Therefore, a superluminal phase velocity is clearly not a problem. The entity which might pose a problem is a superluminal energy velocity, since this contradicts causality. In the dispersion-free medium in which we still are, we can construct superpositions of monochromatic plane waves to create a pulse, and we have to consider the corresponding energy velocity (which in this case turns out to be equal to the phase velocity). In general, it is given by [36]

$$v_e = \frac{|\vec{S}|}{W} = \frac{\left| \frac{1}{2} \vec{E} \times \vec{H}^* \right|}{\frac{\varepsilon_0}{4} \frac{\partial(\omega\varepsilon)}{\partial\omega} |\vec{E}|^2 + \frac{\mu_0}{4} \frac{\partial(\omega\mu)}{\partial\omega} |\vec{H}|^2}, \quad (2.101)$$

where  $\vec{S}$  is the Poynting vector and  $W$  is the electromagnetic energy density. As we have seen, the propagation velocity of the phase fronts in the transformation medium easily exceeds the speed of light in vacuum, and, consequently, so would the energy velocity. This would lead to acausal behavior. Importantly, we have derived this grave consequence under the assumption of a dispersion-free medium. However, nature does not provide any dispersion-free media apart from vacuum. In fact, if we consider a dispersive medium (a “real” material), it can be shown [36] that the energy velocity in Eq. (2.101) is always *smaller* than the speed of light in vacuum (while the phase still advances at superluminal speeds). In this case, the cloak ceases to function properly.

Nature does not provide any materials without dispersion, since this is equivalent to saying that there are no losses in the medium at any frequency. All media in the real world show losses. Whether they might be large or small, they are definitely non-zero at some frequency. For a medium to obey causality, it has to follow the Kramers-Kronig relations [33] (and all media do so). These relations connect the real and imaginary part of any complex analytic response function  $\Psi(\omega) = \Psi_1(\omega) + i\Psi_2(\omega)$  via

$$\Psi_1(\omega) = 1 + \frac{2}{\pi} \mathcal{P} \int_0^{+\infty} \frac{\Psi_2(\omega')}{\omega'^2 - \omega^2} d\omega' \quad (2.102)$$

$$\Psi_2(\omega) = -\frac{2\omega}{\pi} \mathcal{P} \int_0^{+\infty} \frac{\Psi_1(\omega') - 1}{\omega'^2 - \omega^2} d\omega' \quad (2.103)$$

using the Cauchy principal value

$$\mathcal{P} \int_{-\infty}^{+\infty} f(x) dx = \lim_{\epsilon \rightarrow 0} \left( \int_{-\infty}^{x_0 - \epsilon} f(x) dx + \int_{x_0 + \epsilon}^{+\infty} f(x) dx \right). \quad (2.104)$$

Obviously, the real part of the function can only be a constant for all frequencies, if the imaginary part is zero for all frequencies. This argument also applies to the optical response functions  $\varepsilon = \varepsilon_1 + i\varepsilon_2$  and  $\mu = \mu_1 + i\mu_2$ . Therefore, *all* materials show dispersion and losses.

These studies [34, 36] show that the spherical cloak would actually be detectable by an interferometric measurement. In a sense, nature resolves the problem of a superluminal energy velocity derived by the TO approach on its own by only providing materials which ensure that causality is obeyed.

Strictly speaking, TO is therefore only valid for a single frequency, since it neglects dispersion completely. Devices that are designed by TO will simply not work for all frequencies or for arbitrary pulses. However, since there are materials that exhibit a nearly flat dispersion and very low losses, the TO approach can often be applied to a frequency band in good approximation.

## 2.2. Devices Based on Transformation Optics

Since the research in the field of TO was started [21, 22], a variety of new devices and optical components have been proposed. One of the many advantages of using TO as a design tool is the freedom and flexibility in the design process. The propagation of light can be controlled in a very precise way, and even uncommon propagation behavior is achievable. For example, unusual guiding of light in waveguides including sharp  $90^\circ$  turns has been proposed [38–42], as well as bending of waves under nearly arbitrary angle [40]. TO can also be used to enhance known and established devices, such as Eaton lenses [43] and its relatives, by applying transformations which can get rid of singularities in the device’s optical parameters. One of those devices, an omni-directional  $90^\circ$  beam-bending sphere [44, 45], was studied numerically *via* ray tracing during the course of this thesis (see Appendix A.2).

All of this sophisticated control over light propagation is highly desirable for applications including integrated optics on a chip. For optical components of such devices, it is advantageous to provide the desired function independent of its shape (for a simple example, see Fig. 2.1). All kinds of operations can be performed on a beam of light, such as expansion or lateral shifting [46]. A propagating electromagnetic field can even be locally rotated [47, 48]. Further interesting possibilities in manipulating light include high control over the polarization of the field [49, 50].

Another promising subject for transformation devices is light harvesting. A structure which can work over a wide spectral range and guide light from all directions onto a desired target area is sometimes called an optical black hole [51–57] or perfect absorber [58, 59]. Another example are light concentrators [60, 61]. These designs might prove useful in enhancing the efficiency and practicability of solar energy conversion. Furthermore, the opposite case has also been addressed, namely transmitting electromagnetic radiation in a very directed fashion using focusing antennae [62, 63].

Often TO introduces new kinds of degrees of freedom into existing optical elements. One example is a retro reflector, which normally consists of several mirrors. These reflectors have a finite acceptance angle. TO allows for designing omni-directional retro reflectors. Normally, these omni-directional reflectors exhibit singular optical parameters, but a coordinate transformation, a “transmutation” of these singularities, is able to get rid of them by introducing anisotropy into the system [64–66]. With the aid of TO, existing designs can be extended and improved, for example lenses in a large variety [67–74].

A special lens, namely the “perfect lens”, was proposed in 2000 by J. B. Pendry [17]. It makes a perfect (although unmagnified) image of an object, with no constraints on the resolution - thus breaking Abbe’s diffraction limit. The lens consists of a region of space that is filled with a negative index material ( $\varepsilon = \mu = -1$ ). Although it was originally conceived before the ideas of TO were fully developed, it can, in retrospective, be described and understood using coordinate transformations, namely a so-called folded-geometry transformation. The perfect lens can also be examined under a different aspect. The fact that one region of space is complementary to another with regard to its optical parameters (meaning that they have opposite sign but the same absolute value) is described as a “complementary medium”. These media can also be used to form super scatterers - scatterers which exhibit a largely enhanced scattering cross section compared to their geometrical size [75, 76]. In other words: objects appear larger than they are. This can be utilized to create so-called “hidden gateways” [77, 78]: Light cannot penetrate the gateways due to their apparent size and large scattering cross section, while in fact the scattering object itself is smaller and lets room for small particles to pass through.

Consequently, TO can also be used to make things appear different. Even shapes of objects can be modified and things can be disguised. The term “illusion optics” has been coined for such structures [79, 80]. The ultimate illusion, however, is to make things disappear – an invisibility cloak. The first example of such a cloak was the cylindrical invisibility cloak [21, 81, 82] (see Appendix A.1), followed by the very successful carpet cloak described in this thesis.

In a more general context, TO has also made its way back to its roots of Einstein’s relativity, paving the way to test the electromagnetic analogs of relativistic effects such as the event horizon of a singularity [83] or wormholes [84].

Finally, we want to emphasize that although TO was conceived and applied in the context of electromagnetism and Maxwell’s equations, the underlying ideas are not restricted to that area. Any set of wave equations can be treated in the same way, as long as they remain invariant under coordinate transformations. The concepts of TO have been successfully applied to acoustic waves [85–88], elastic waves (under certain special conditions) [89–91], matter waves [92, 93], and linear (liquid) surface waves [94, 95].

TO has been developed into a versatile tool to design and analyze a plethora of novel phenomena in a variety of different physical systems.

## 2.3. Carpet Cloak

TO is a powerful new approach to ray and wave optics and their connection to the geometry of space. It allows for designing intriguing new devices, some of which have been discussed in the previous section. A major drawback of some of the designs derived from TO is the feasibility when it comes to the actual experimental realization, since most designs require anisotropic, inhomogeneous and often singular values of the optical parameters. Furthermore, strong magnetic responses are necessary, since a general transformation yields  $\epsilon \propto \mu$  (see Section 2.1). The carpet cloak [96–105, 105–120], introduced by J. Li and J. B. Pendry [96], poses an exception to that rule. Here, anisotropy can be eliminated, there are no singular values, and the permeability is unity - one is left with an inhomogeneous refractive-index distribution. Another way of looking at the carpet cloak is as an exotic GRIN lens, which corrects for aberrations introduced by the object that is to be hidden.

Let us start by describing the general idea of the carpet cloak (shown schematically in Fig. 2.3). Here, an arbitrarily shaped object is hidden underneath a reflecting carpet. The result is a mirror with a bump in it, under which the object is concealed. The bump is immediately visible to an observer simply by looking at it, since the reflected images in the mirror are distorted. This effect is known to everyone who has ever stood in front of a fun house mirror. Naturally, measuring the intensity distribution (or even more sensitive, the phase fronts) of the reflected light before and after placing the object under the carpet mirror will definitely reveal the presence of the bump. Once the carpet cloak (which is sometimes also called “ground-plane cloak”) is placed on top of the bump, the reflected images are reconstructed completely - the mirror again looks flat. An observer cannot distinguish the hidden object covered by the cloak from a bare flat reflecting surface. If the cloak works perfectly, the intensity distribution and the phase of the reflected light is that of a flat surface. Another perspective is provided by using geometrical optics: A parallel bundle of rays that is incident on the bump is heavily distorted and broken up. After being reflected at the bump, the rays are strongly divergent. The carpet cloak corrects for that and bends the rays such that they emerge again from the cloak as a parallel bundle.

As mentioned before, there is an infinite number of transformations that perform the given task. It is up to the experimenter to choose a specific one, depending on his intentions and, most importantly, the material system at hand. In the following, we want to present two types of transformations that qualify as a carpet cloak and discuss their advantages and disadvantages, before describing our approach using a quasiconformal mapping in detail in Section 4.1.

One possibility of mapping one grid to another is a conformal transformation. This class of two-dimensional transformations maps the entire complex plane onto Riemann sheets (Riemann mapping theorem [26, 121]). Every analytical function in the complex

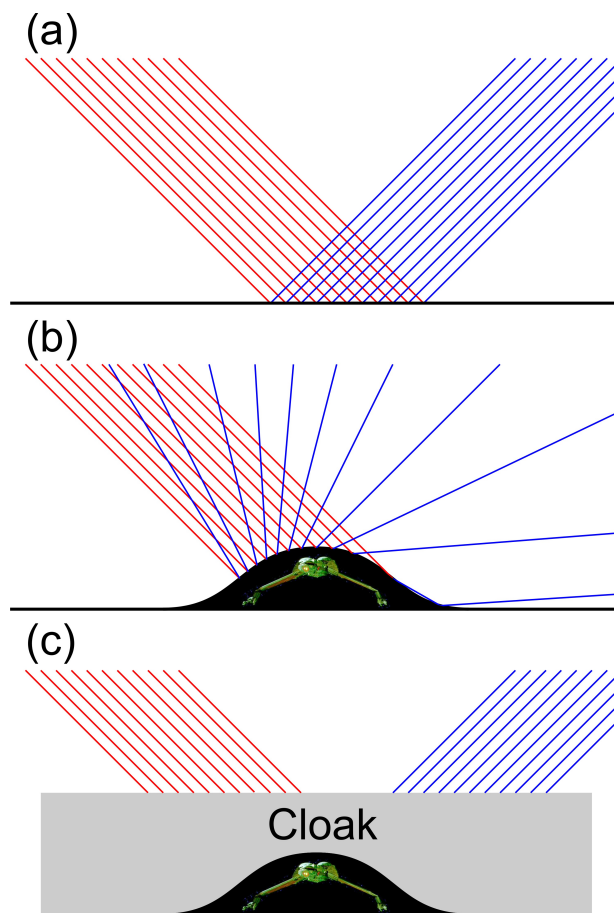


**Figure 2.3.:** Simple schematic drawing of the basic idea of the carpet cloak. **(a)** An incoming parallel bundle of rays (red) is reflected at a flat mirror. The reflected rays (blue) also form a parallel bundle and exit under the same angle as the incident rays. **(b)** A bump, under which an arbitrarily shaped object can be concealed, is introduced into the mirror. The reflected bundle is heavily perturbed and depicts a large angle spread. **(c)** The carpet cloak (gray) is placed on top of the bump. The incident rays follow curved lines inside the cloak (see ray-tracing calculations in Fig. 4.6) and are redirected such that they exit the cloak with the same physical properties as in (a) - the mirror appears to be flat and the bump including the object is invisible to an observer.

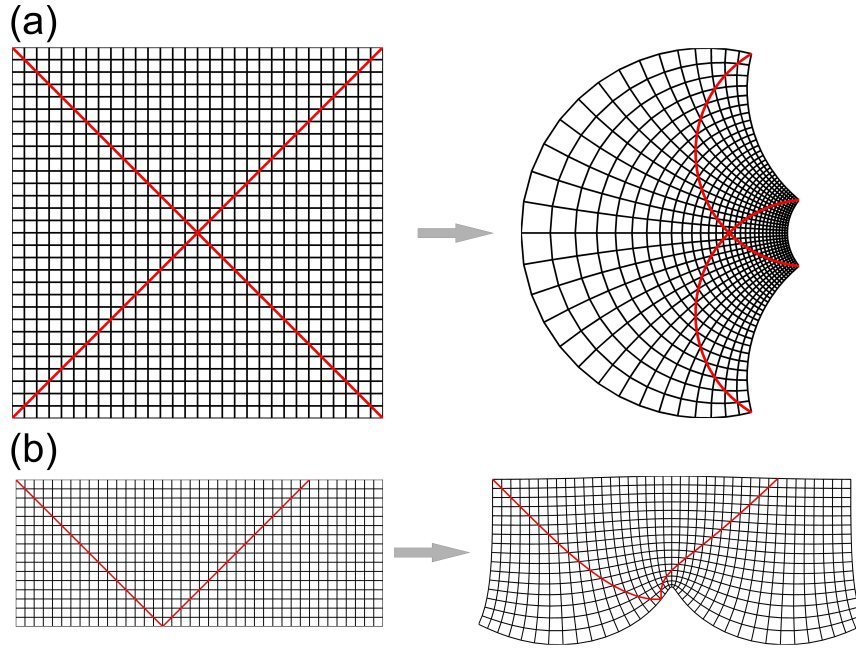


**Figure 2.4.:** Conformal transformations. **(a)** Möbius transformation, which maps the Cartesian grid on the left onto the curved grid on the right. Note that although the measure of distance in space is changed, all angles are preserved. The two red lines intersect orthogonally in both grids. **(b)** Conformal transformation for a carpet cloak. The same ray is shown in red in both grids.

plane  $w = f(z) = f(x + iy) = u(x, y) + iv(x, y)$  is conformal. A function in the complex plane is said to be analytical, if it satisfies the Cauchy-Riemann equations given by

$$\frac{\partial u}{\partial x} = \frac{\partial v}{\partial y} \quad \text{and} \quad \frac{\partial v}{\partial x} = -\frac{\partial u}{\partial y}. \quad (2.105)$$

To illustrate the properties of conformal transformations, we examine the well-known example of a “Möbius transformation”

$$w = \frac{az + b}{cz + d}, \quad (2.106)$$

with complex constants  $a, b, c, d$ . It is depicted in Fig. 2.4(a) for a random set of parameters. Importantly, a conformal transformation generally changes the measure of distance in space, but it preserves all angles and the shapes of infinitesimally small figures. Note that the red lines intersect orthogonally in both coordinate systems. Therefore, conformal transformations do not introduce any anisotropy. This property makes them interesting for designing devices with TO [22, 110, 112, 122, 123]. In Fig. 2.4(b), we depict a conformal transformation for a carpet (or in this case “grating”) cloak of the type described in Ref. [112]. A ray (red line) that reflects off of the ground is shown in the Cartesian grid. The same ray is also depicted in the transformed space. It exits the cloak at the same

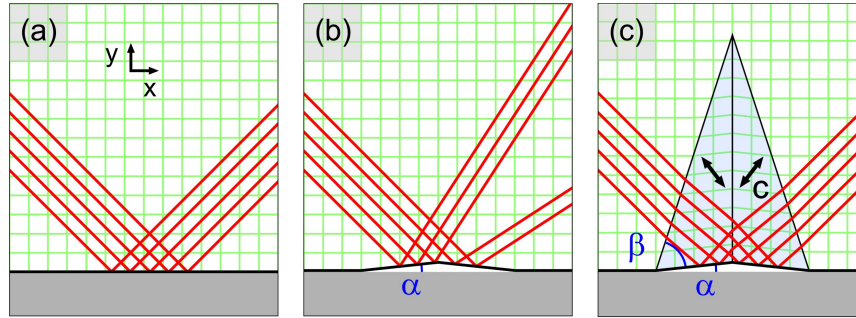


**Figure 2.5.:** (a) A parallel ray bundle entering from the top left is reflected at the mirror floor. (b) A triangular-shaped bump is introduced into the mirror. The bundle splits into two. (c) Two calcite crystals with crystallographic axes  $c$  are cut and glued together to form the cloak. Each crystal segment is homogeneous and anisotropic [124].

point and under the same angle as in the Cartesian case, which makes the curvature of the mirror disappear. With regard to the carpet cloak, a conformal transformation can get rid of certain undesired aspects of the cloak, which are sometimes summarized under the term “ostrich effect” (see also Section 4.3.2). This term describes the fact that the cloak hides the object to be hidden, yet the cloak itself is detectable to some extent. One of these aspects is that a carpet cloak, which is derived using a *quasiconformal* method (see Chapter 4.1), exhibits a lateral shift of the reflected ray bundle [109]. As we will see later, a small but finite anisotropy is dropped in the quasiconformal approach. This leads to the fact that the reflected rays shift by a magnitude that is on the order of the height of the hidden object [109]. Since a conformal transformation yields a locally isotropic distribution of the optical parameters by definition, it is also free of any shifts. A drawback of the conformal transformation is that, strictly speaking, it has to be performed on the complete plane, whereas the quasiconformal transformation is done on a subset of it. Nevertheless, it has been shown [112] that the conformal map can be truncated in order to produce a finite-sized cloak and still show very good performance similar to or even better than the results obtained by a cloak using a quasiconformal map. By the choice of the truncation and the conformal transformation itself, the lateral shift can at least be reduced [112]. A major advantage of the conformal mapping is that it is a purely analytical approach. The derived refractive-index distribution is a closed analytical expression and involves no numerical calculations, which makes it far easier to handle, both for theoretical and experimental purposes. A small drawback of that analyticity is that the form of the bump that is to be hidden cannot be chosen arbitrarily - it is directly connected to the transformation. The quasiconformal approach, on the other hand, allows for an initial free shaping of the bump and the subsequent calculation of the corresponding map.

After discussing the conformal approach using an isotropic medium, let us now turn to a second possibility: a transformation that compresses space in only one direction using a triangular-shaped bump [113, 118]. This choice of transformation will inevitably lead to

anisotropic material parameters. Yet, importantly and in contrast to both conformal and quasiconformal transformations, they are homogeneous. In this approach (see Fig. 2.5), only the  $y$ -coordinate is transformed following  $y \rightarrow y'(x, y) = a|x| + by$  with  $b < 1$ . The cloak consists of two parts with a vertical separation in the middle. In each segment, the principal axes of the medium's refractive index do not coincide with the coordinate axes any more. Since the refractive index is anisotropic but homogeneous, and shows constant local principal axes, calcite crystals can be used to form the transformation medium. Two pieces of calcite with selected principal axes are cut and glued together. Because such media are relatively easy to fabricate, these carpet cloaks can be made in macroscopic size. Here, the cloak is three orders of magnitude larger than the wavelength of light, and it also works at visible frequencies. A drawback of these anisotropic cloaks is that they only work for one polarization of light, which practically makes them two-dimensional devices. Furthermore, they are restricted to triangular-shaped bumps and cannot be used for bumps with nonlinear slopes. For this, the transformation medium additionally would have to be inhomogeneous.

The most widely used transformation for designing a carpet cloak has been the quasiconformal map. Almost all experimental realizations rely on it, whether they may be two-dimensional [97–100, 105, 115] or three-dimensional [106, 108, 114, 119, 120]. Since this work is based on the quasiconformal approach, a detailed description will be given in Section 4.1 and its numerical implementation will be discussed .



## 3. Materials and Fabrication

### 3.1. Metamaterials

In Chapter 2, we have introduced the concepts of TO and the basic idea of the carpet cloak. It was shown that devices that are based on TO often exhibit exotic and demanding optical parameters, most of which are not found in natural materials. Therefore, it is necessary to develop a way to implement such parameters in an experiment. Obviously, we have to create materials with those tailored properties artificially.

The first idea towards what we call “metamaterial” today came from J. B. Pendry and coworkers [8, 9] in the late 1990’s. In their work [8], they described a three-dimensional cubic lattice of thin metallic wires and harvested the plasmonic properties of this structure to assign a largely reduced effective plasma frequency to the material. Here, the emphasis lies on the word “effective”. We quote from Pendry’s work: “*In other words, as far as external electromagnetic radiation is concerned, this structure appears as an effectively homogeneous dielectric medium whose internal structure is only apparent insofar as it dictates  $\epsilon_{\text{eff}}$* ” [8]. In a second paper, the authors continued to “[...] *show that microstructures built from nonmagnetic conducting sheets exhibit an effective magnetic permeability  $\mu_{\text{eff}}$ , which can be tuned to values not accessible in naturally occurring materials [...]*” [9]. These two quotes already contain some of the most important properties of a metamaterial: It is described by a set of effective optical parameters, and naturally occurring materials can be structured and combined to give rise to extraordinary optical parameters in such metamaterials. The term “metamaterial” was coined shortly after Pendry’s publications by D. R. Smith [125] and R. M. Walser [126], respectively (depending on the source). The term is derived from the Greek word “ $\mu\epsilon\tau\acute{\alpha}$ ” meaning “after” or “beyond”, and reflects the fact that these materials pave the way to plunge into the realm that lies “beyond” materials provided by nature.

But what enables metamaterials to outperform conventional natural materials? With regard to naturally occurring media, we take the fact for granted that they are made of small building blocks – atoms and molecules. In optics, we are used to treating these materials with the macroscopic Maxwell equations (see Eqs. (2.46)-(2.49)). They imply that effective optical parameters can be assigned to the material, so that we don’t have to concern ourselves with the microscopic substructure. The light does not “see” the building

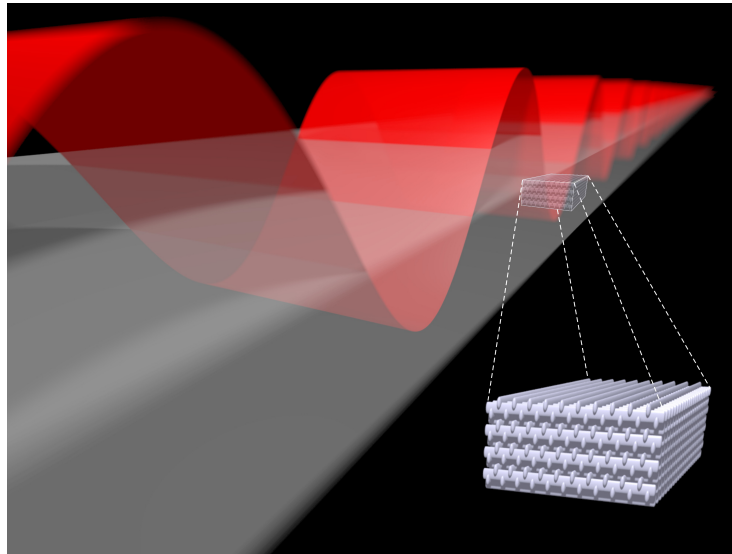


**Figure 3.1.:** Artist’s view of an electromagnetic wave propagating through a seemingly homogeneous medium with effective optical parameters. The wave does not resolve the building blocks of the structured metamaterial.

blocks, it rather averages over the local structure. This principle is illustrated in Fig. 3.1 and holds as long as

$$a \ll \lambda, \quad (3.1)$$

where  $\lambda$  is the wavelength of the electromagnetic radiation and  $a$  is the characteristic dimension of the material, for example the lattice constant of a crystal. Since the effective optical parameters are governed by the microscopic properties of the medium on an atomic scale, it is worth to try to replace the atoms in a material by larger man made structures – “artificial atoms”. As long as Eq. (3.1) holds, the material should be describable by effective parameters. The exciting advantage of these artificial atoms is that their electric and magnetic response can be tailored by the choice of the constituent materials and, more importantly, by their geometry. This introduces a completely new degree of freedom into the design of optical elements.

To illustrate the impact that metamaterials have on the accessible range of optical parameters, Fig. 3.2 shows a plot of all values of the permittivity and permeability (to be precise: the real parts of these quantities). All areas shown in gray can be populated by naturally occurring materials. The most commonly known region is the upper right quadrant, where both optical parameters are positive simultaneously. We call these media double-positive materials or DPS. At optical frequencies, on which the focus of this work lies, this quadrant basically collapses to a horizontal line at  $\mu = 1$ , since the magnetic polarization of natural materials vanishes at these frequencies. On this line, dielectrics give rise to permittivity values above unity. Plasmas or metals above the plasma frequency exhibit values below unity. The quadrant on the upper left is populated by plasmas and metals below the plasma

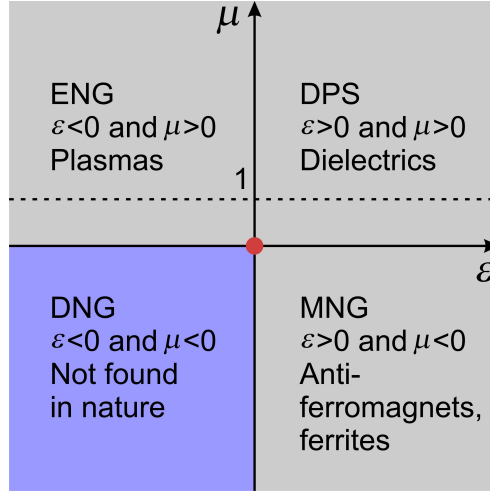


**Figure 3.2.:** Plot of all possible values of (the real parts of) the permittivity  $\varepsilon$  and the permeability  $\mu$ . The gray areas are found in naturally occurring materials under some circumstances and at certain frequencies. However, the blue quadrant, where both parameters are negative simultaneously, can only be accessed by using artificially created metamaterials. The red dot marks the “zero-index condition”, where the refractive index  $n = \sqrt{\varepsilon\mu}$  vanishes.

frequency. Thus, we call these media  $\underline{\varepsilon}$ -negative materials or ENG. The last quadrant that can be accessed by natural materials is the lower right. From the symmetry of Maxwell’s equations, a magnetic plasma is expected here. Due to the non-existence of free magnetic monopoles, such a plasma does not exist naturally. Nevertheless, some antiferromagnets and ferrites exhibit a negative permeability at certain frequencies. We call these media  $\underline{\mu}$ -negative materials or MNG. Finally, the optical parameters in the blue quadrant are not realized by any known natural material, both  $\varepsilon$  and  $\mu$  are negative. These materials are called double-negative materials or DNG. Here, exciting behavior emerges from the fact that the refractive index becomes negative.

Let us examine the index of refraction and the corresponding propagation behavior of an electromagnetic wave in these four quadrants. The electromagnetic wave equations [33] in an isotropic linear medium with static optical parameters are solved by the plane wave *ansatz*

$$\vec{E}(\vec{r}, t) = \vec{E}_0 e^{i(\vec{k}\vec{r} - \omega t)} \quad (3.2)$$

$$\vec{B}(\vec{r}, t) = \vec{B}_0 e^{i(\vec{k}\vec{r} - \omega t)}. \quad (3.3)$$

After solving for  $\vec{k}$ , we easily obtain

$$\vec{k} = n\vec{k}_0 \quad (3.4)$$

with

$$n = \pm\sqrt{\varepsilon\mu}, \quad (3.5)$$

### 3. Materials and Fabrication

---

where  $\vec{k}_0$  is the free space wave vector and  $n$  is the refractive index. At this point, we have to decide which sign to choose for the square root in Eq. (3.5). The permittivity  $\varepsilon = \varepsilon_1 + i\varepsilon_2 = |\varepsilon|e^{i\phi_\varepsilon}$  and the permeability  $\mu = \mu_1 + i\mu_2 = |\mu|e^{i\phi_\mu}$  are (in general) complex-valued quantities, and so is the refractive index  $n = n_1 + in_2 = |n|e^{i\phi_n}$ . Consequently, the square root yields

$$n = \pm \sqrt{|\varepsilon||\mu|} e^{i\frac{\phi_\varepsilon + \phi_\mu}{2}}. \quad (3.6)$$

The imaginary part of the refractive index describes losses ( $\text{Im}(n) > 0$ ) and gain ( $\text{Im}(n) < 0$ ), respectively. In the case of a passive medium,  $\text{Im}(n) \geq 0$  must hold, which fixes the complex square root to [127]

$$n = \sqrt{|\varepsilon||\mu|} \exp \left[ \frac{i}{2} \left( \text{arccot} \frac{\varepsilon_1}{\varepsilon_2} + \text{arccot} \frac{\mu_1}{\mu_2} \right) \right]. \quad (3.7)$$

It is apparent from this equation, that the imaginary parts of the permittivity and the permeability, respectively, also contribute to the choice of the sign. Nevertheless, the most desirable situation is one where both real parts of  $\varepsilon$  and  $\mu$  are negative while the imaginary parts are as small as possible, simultaneously.

Let us turn to the propagation behavior. If we evaluate Eq. (3.7) for all four quadrants in Fig. 3.2, we find that DPS support propagating waves, as one would expect from transparent dielectrics. As commonly known, the wave vector  $\vec{k}$  forms a right-handed tripod with  $\vec{E}$  and  $\vec{H}$ , and so does the Poynting vector  $\vec{S} = \frac{1}{2}\vec{E} \times \vec{H}^*$ . The propagation of the phase fronts (or the direction of the phase velocity  $v_{\text{ph}}^{\vec{h}}$ ) is in the same direction as the energy flow. For both ENG and MNG, the situation is different. Here, the wave vector  $\vec{k}$  becomes imaginary, which leads to exponentially decaying waves and evanescent modes. Although the wave vector still points in the same direction as the Poynting vector, energy is not transmitted. This is the common behavior of plasmas below their plasma frequency, for example metals at infrared or optical frequencies. In the case of DNG, we again find propagating waves. However, the propagation differs from the DPS behavior in a key aspect. Now, the wave vector points in the opposite direction than the Poynting vector and forms a left-handed tripod with  $\vec{E}$  and  $\vec{H}$  (for this reason, negative-index materials are also called left-handed materials). This becomes apparent when considering the refraction of a light wave at an interface between a material with  $n_1 = 1$  and another material with  $n_2 = -1$ . Due to conservation of momentum of the parallel component across the interface, the normal component has to switch sign. Additionally, the wave bends “to the wrong side” of the normal upon refraction at the interface.

Although metamaterials may be most renowned for the negative index of refraction, it is by far not the only potential of those structures. In a nutshell, optical devices that have been thought to be impossible for a long time can now be designed using TO and realized with metamaterials.

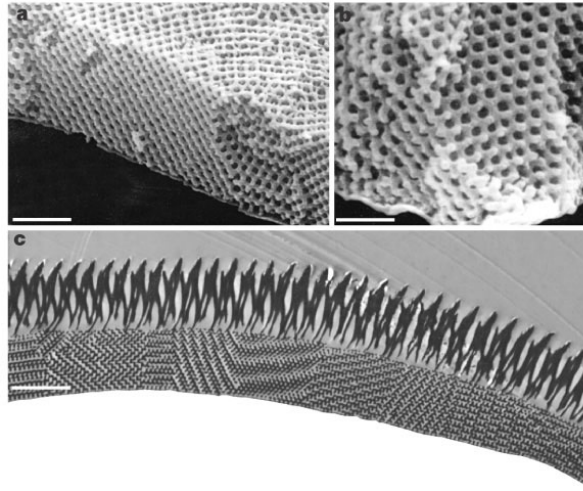


**Figure 3.3.:** The wing of the butterfly species *parides sesostris* consists partially of a three-dimensional photonic crystal. The scale bars correspond to a)  $2.5\ \mu\text{m}$ , b)  $1.2\ \mu\text{m}$ , and c)  $750\ \mu\text{m}$ . Taken from [128].

## 3.2. Photonic Crystals

In this chapter, we briefly want to discuss the fundamentals of photonic crystals, especially a three-dimensional type, the woodpile photonic crystal. Although we do not make use of its photonic crystal properties in this thesis but rather use it as an effective medium or metamaterial, we want to present its properties here and discuss the implications for this work.

A photonic crystal is a material which is endowed with a periodic modulation of its optical parameters  $\varepsilon$  and/or  $\mu$  on a length scale comparable to the wavelength of light. It is called “crystal”, since it shows a periodicity, and the name “photonic” indicates a light-matter interaction. Dependent on the number of dimensions in which one finds a periodicity, the structure is called a one-, two-, or three-dimensional photonic crystal. Photonic crystals are mostly artificial structures, although there are examples found in nature (see Fig. 3.3). Similar to crystals in solid-state physics (“electronic crystals”), where the periodic potential of the ions leads to a band structure that can exhibit band gaps, photonic crystals can inhibit the propagation of light in certain directions and at certain frequencies. These frequency regions are called stop bands, and they will become important later on.

In the late 1980’s, S. John [129] and E. Yablonovitch [130] pioneered the field of photonic crystals. The latter studied the suppression of the spontaneous emission of a two-level system through nano-structured materials. Such a manipulation of transition rates can lead to higher efficiencies in solar cells, for example. This would be particularly interesting for visible wavelengths of light, but although almost 25 years have passed since the

proposal, the fabrication of photonic crystals remains a challenge, especially in the three-dimensional case. But why is it so difficult? The answer lies in the associated length scale on which a material has to be structured in order to act as a photonic crystal. We can estimate the involved scales when we consider the onset of strong light-matter interaction in periodic structures. If we consider a one-dimensional case, namely a stack of layers with alternating optical parameters and period  $a$ , the Bragg formula describes the diffraction of the impinging electromagnetic radiation. The formula for normal incidence reads as

$$a = \frac{m\lambda}{2}, \quad (3.8)$$

where  $m \geq 1$  is an integer number that gives the diffraction order and  $\lambda = \lambda_0/n$  is the wavelength in the medium with a refractive index  $n$  and a free-space wavelength  $\lambda_0$ . From this, it is clear that the periodicity of the structure has to be of the same order as the wavelength. For three-dimensional photonic crystals at optical frequencies, this means controlled structuring on a scale of a few hundred nanometer in all spatial directions. In the following, we only want to give a very brief introduction into the physics of photonic crystals. For a detailed description, we refer the reader to the book of J. Joannopoulos *et al.* [131].

In a photonic crystal, the constitutive materials are heterogeneously but periodically distributed in space. Let us assume that the constitutive materials themselves are homogeneous and isotropic. Furthermore, we want to study the special case for which the frequency  $\omega$  is fixed and all fields exhibit a harmonic time dependence. Therefore, the permittivity  $\varepsilon(\vec{r})$  and the permeability  $\mu(\vec{r})$  are scalar functions only of space. Under these assumptions, the Maxwell equations in their time-harmonic form [33] (and without free charges and currents) read

$$\nabla \cdot (\mu(\vec{r})\vec{H}(\vec{r})) = 0 \quad (3.9)$$

$$\nabla \cdot (\varepsilon(\vec{r})\vec{E}(\vec{r})) = 0 \quad (3.10)$$

$$\nabla \times \vec{E}(\vec{r}) - i\omega\mu_0\mu(\vec{r})\vec{H}(\vec{r}) = 0 \quad (3.11)$$

$$\nabla \times \vec{H}(\vec{r}) + i\omega\varepsilon_0\varepsilon(\vec{r})\vec{E}(\vec{r}) = 0. \quad (3.12)$$

Using Eqs. (3.11) and (3.12), we can derive the wave equation (also known as master equation)

$$\nabla \times \left( \frac{1}{\varepsilon(\vec{r})} \nabla \times \vec{H}(\vec{r}) \right) = \left( \frac{\omega}{c_0} \right)^2 \mu(\vec{r})\vec{H}(\vec{r}), \quad (3.13)$$

where we used the speed of light in vacuum  $c_0 = 1/\sqrt{\varepsilon_0\mu_0}$ . In the wave equation (3.13), we can assign an operator  $\hat{\Theta}$  acting on  $\vec{H}$  via

$$\hat{\Theta}\vec{H} = \nabla \times \left( \frac{1}{\varepsilon(\vec{r})} \nabla \times \vec{H}(\vec{r}) \right), \quad (3.14)$$

so that the wave equation now reads

$$\hat{\Theta}\vec{H} = \left(\frac{\omega}{c_0}\right)^2 \mu(\vec{r})\vec{H}(\vec{r}). \quad (3.15)$$

This eigenvalue equation contains the eigenvectors  $\vec{H}$ , which are the spatial patterns of the photonic modes, and the eigenvalues, which are proportional to the squared frequencies. Note again that for all natural materials,  $\mu(\vec{r})$  is unity at optical frequencies, so that we can drop it. After solving for  $\vec{H}$ , we can then recover  $\vec{E}$  from Eq. (3.12):

$$\vec{E}(\vec{r}) = \left(\frac{i}{\varepsilon_0\varepsilon(\vec{r})\omega}\right) \nabla \times \vec{H}(\vec{r}). \quad (3.16)$$

In order to find solutions for  $\vec{H}$  in a photonic crystal, we can use the fact that the optical parameters are modulated periodically in space:

$$\varepsilon(\vec{r} + \vec{R}) = \varepsilon(\vec{r}), \quad (3.17)$$

where  $\vec{R}$  is the lattice vector of the crystal:

$$\vec{R} = \sum_i c_i \vec{a}_i. \quad (3.18)$$

Here,  $\vec{a}_i$  are the fundamental lattice vectors of the unit cell. Similar to what is done in solid-state physics, we can then use a Bloch-*ansatz* [132]

$$\vec{H}(\vec{r}) = \vec{u}_{\vec{k}m}(\vec{r})e^{i\vec{k}\vec{r}} \quad (3.19)$$

with  $\vec{u}_{\vec{k}m}(\vec{r})$  being a vectorial function that is periodic with  $\vec{R}$ . In the same manner as in solid-state physics, we can plot the eigenvalues (frequencies)  $\omega_m(\vec{k})$  with the band index  $m$  as a function of the wave vector  $\vec{k}$  in the irreducible Brillouin zone. The result is the band structure of the photonic crystal.

Let us now introduce the type of photonic crystal that is used throughout this work. It is called a “woodpile photonic crystal” [133], since its structure resembles a pile of wooden logs. A schematic illustration of the woodpile is depicted in Fig. 3.4. It consists of subsequent layers of polymer rods with lateral distance  $a$ , where the layers are rotated and shifted with respect to each other. After four layers, the structure repeats itself with a lattice constant  $c$  in the axial direction. The ratio  $c/a$  dictates the symmetry of the woodpile. For  $c/a = \sqrt{2}$ , one obtains a face-centered-cubic (fcc) translational lattice, for  $c/a = 1$  a body-centered-cubic (bcc) translational lattice. The woodpiles used in this work show an fcc symmetry by design. Note that although the unit cell shown in Fig. 3.4 is easy to understand and visualize, it is not the primitive unit cell of the woodpile, but rather a super cell. The primitive cell has the shape of a parallelepiped with only two perpendicular rods in it.

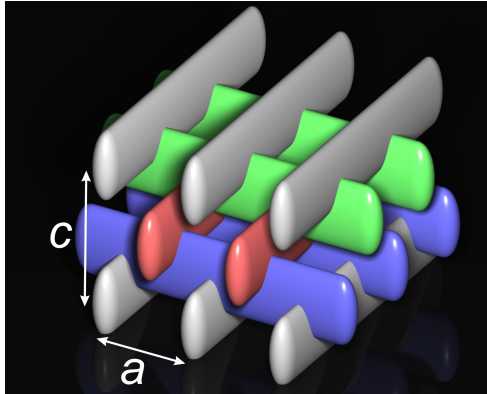


**Figure 3.4.:** Schematic illustration of a three-dimensional woodpile photonic crystal. The woodpile is composed of a first layer (gray) of periodically arranged dielectric rods with spacing  $a$ , a second orthogonal layer (blue), a third layer (red) displaced by half the rod spacing with respect to the first layer, and a fourth layer (green) displaced by half the rod spacing with respect to the second layer. This pattern is repeated and leads to an axial lattice constant  $c$  [120].

In Fig. 3.5, we depict the band structure (calculated with the *MIT Photonic-Bands (MPB)* package [134]) of a three-dimensional woodpile photonic crystal made of polymer ( $n = 1.52$ ) and air ( $n = 1$ ) with fcc symmetry. The aspect ratio (height/width) of the rods has been chosen to be 2.7 and the lateral width of the rods is  $0.3a$ , where  $a$  is the rod distance. Most importantly, we want to emphasize that in the long-wavelength limit ( $|\vec{k}| \rightarrow 0$ ), the photonic crystal depicts a linear dispersion. Here, we can assign an effective refractive index  $n_{\text{eff}}$  to the medium – the photonic crystal acts as an effective medium, since the electromagnetic wave does not resolve the local structure. It is in this regime that we use the photonic crystal in this work. It is our goal to tailor the local structure of the photonic crystal by changing the filling fraction of the constitutive materials in a unit cell. This gives rise to a spatially varying effective refractive index. We can derive the refractive index by linearly fitting the dispersion relation for  $|\vec{k}| \rightarrow 0$  (this regime is marked gray in Fig. 3.5), since the group velocity in the medium is given by

$$v_g = \frac{\partial \omega}{\partial |\vec{k}|} = \frac{\partial \omega}{n_{\text{eff}} \partial |\vec{k}_0|} = \frac{c_0}{n_{\text{eff}}}. \quad (3.20)$$

In this linear regime, the group velocity  $v_g$  is actually equal to the phase velocity  $v_p$  of the light:

$$v_p = \frac{\omega}{|\vec{k}|} = c = \frac{c_0}{n_{\text{eff}}}. \quad (3.21)$$

Naturally, a different size or shape of the rods will lead to a different filling fraction of the woodpile, which results in a different slope of the linear dispersion regime. We have calculated band structures for several filling fractions and performed the fitting procedure

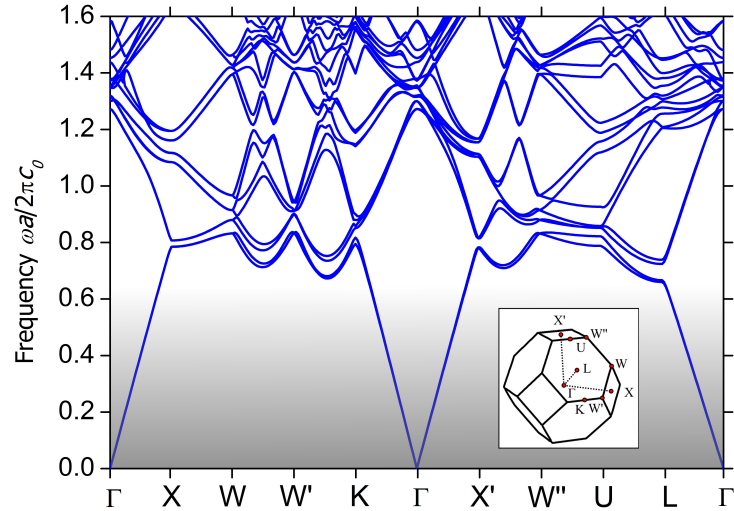


**Figure 3.5.:** Photonic band structure of a polymer ( $\varepsilon = 2.3$ ) fcc woodpile photonic crystal. We follow a path through the Brillouin zone along the symmetry points (see inset, taken from [135]). The long-wavelength limit of the woodpile is marked in gray. In this linear dispersion regime, an effective refractive index can be assigned to the structure. The index is found by fitting a line to the band structure and extracting the slope.

subsequently. With this, we are able to map the filling fraction of the woodpile onto an effective refractive index of the structure.

Another aspect of the woodpile becomes apparent in the band structure: it is almost isotropic (the slopes of the linear fits around the  $\Gamma$ -point are nearly equal). To verify this, we have calculated a complete octant of the Brillouin zone on a  $100 \times 100 \times 100$  grid. From this, we can evaluate the isofrequency surface of the woodpile, which turns out to be nearly spherical (see Fig. 5.2 in Section 5.1).

The woodpile photonic crystal is therefore well-suited to serve as a locally controllable metamaterial with effective refractive index properties, as long as it is used in the long-wavelength limit. Since our group has years of experience in the fabrication of these structures, it is the natural choice.

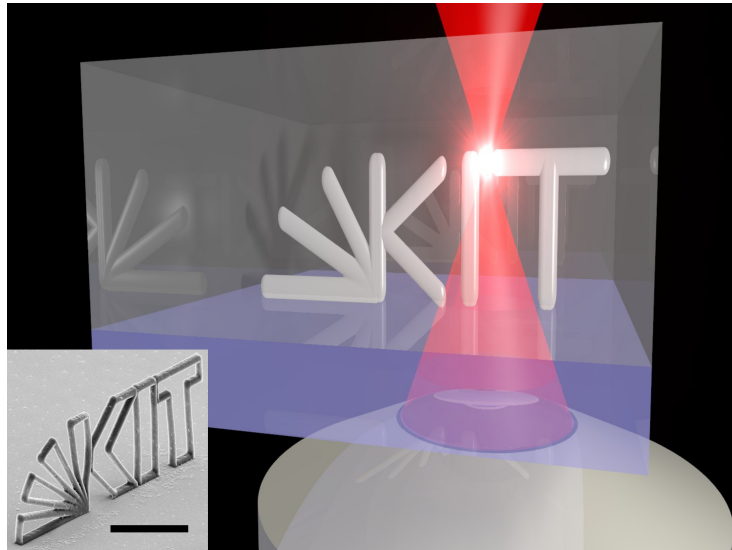


**Figure 3.6.:** Artist's illustration of the DLW process. A laser beam (red) is tightly focused into a photoresist (transparent gray) through a glass substrate (transparent blue). The resist is polymerized in the focal volume only. After development, the three-dimensional polymer structure (white) remains. The inset (by courtesy of M. Thiel) shows an electron micrograph of an actual structure. The scale bar corresponds to  $40\ \mu\text{m}$ .

## 3.3. Fabrication Techniques

At this point, we have introduced the concepts of TO, the carpet cloak and the possibility to create tailored optical parameters using a woodpile photonic crystal as a metamaterial. In this section, we briefly want to review the fabrication techniques used in this thesis, and we will demonstrate how the aforementioned woodpile structure can be realized experimentally.

### 3.3.1. Direct Laser Writing

Direct laser writing (DLW) [136–140] is a lithography technique that has a major advantage over most other lithography techniques such as electron-beam or deep ultraviolet lithography: it is capable of producing nearly arbitrary shapes in three dimensions. Nowadays, it is a well-established technique and has even found its way into a commercial product [141]. We use such a commercial machine (Photonic Professional, Nanoscribe GmbH) to fabricate some of the structures that will be presented later in this thesis.

The working principle of DLW is fairly easy to understand (see Fig. 3.6). A pulsed laser is tightly focused into a photoresist that has been deposited onto a glass substrate. The

resist consists of a monomer and a photoinitiator. While the photoresist is transparent at the laser’s fundamental frequency, it absorbs at twice that frequency. The high local intensities in the focal volume give rise to two-photon absorption and other nonlinearities. If the deposited light dose is above a certain threshold, a chemical polymerization reaction in the photoresist is started. Since the polymerization is confined solely to the focal volume, a single three-dimensional pixel (“voxel”) with ellipsoidal shape is created. The sample is then scanned *via* a computer-controlled piezo stage with respect to the laser focus, creating a pre-programmed trace of arbitrary three-dimensional shape. After the exposure of the complete structure, the photoresist is developed and the unpolymerized monomer is removed. The final result is a free-standing three-dimensional polymer structure.

However, there are limitations to this technique when it comes to decreasing the structural dimensions. Since a focused laser is used for the polymerization, the size of the smallest achievable voxel is limited by diffraction. Ernst Abbe stated in his famous formula that the smallest distance which can be resolved by a microscope at a given free-space wavelength  $\lambda$  is given by

$$d = \frac{\lambda}{2\text{NA}}, \quad (3.22)$$

where  $\text{NA} = n \sin \alpha$  is the numerical aperture with the refractive index  $n$  and the opening angle  $\alpha$  of the light cone. For a DLW setup with  $\text{NA} = 1.4$  and  $\lambda = 810 \text{ nm}$ , this translates [142] into a lateral center-to-center distance of

$$d_{\text{lateral}} = \frac{\lambda}{2\sqrt{2}\text{NA}} = 205 \text{ nm}, \quad (3.23)$$

assuming Gaussian profiles and two-photon absorption. The lateral dimension of a single voxel is on the order of 80 nm. This seemingly sub-diffraction feature size is due to the fact that the deposited dose is proportional to the squared intensity, not the intensity itself. Furthermore, when the dose is just above the polymerization threshold, the width further decreases. However, such structures tend to be mechanically unstable. Importantly, the axial voxel dimension is at least worse by a factor of 2.5, and it is in fact the axial resolution which mainly inhibits further miniaturization of fabricated structures.

Nevertheless, this regular DLW setup is fully capable of creating stable woodpile photonic crystals of good quality with a rod center-to-center distance of 800 nm. This is used for the fabrication of the three-dimensional carpet cloak operating at infrared wavelengths (see Section 5.1).

### 3.3.2. Stimulated-Emission-Depletion-Inspired Direct Laser Writing

Since the diffraction limit formulated by Abbe can not be simply switched off, one has to “play tricks” to break this diffraction barrier in order to further shrink the accessi-

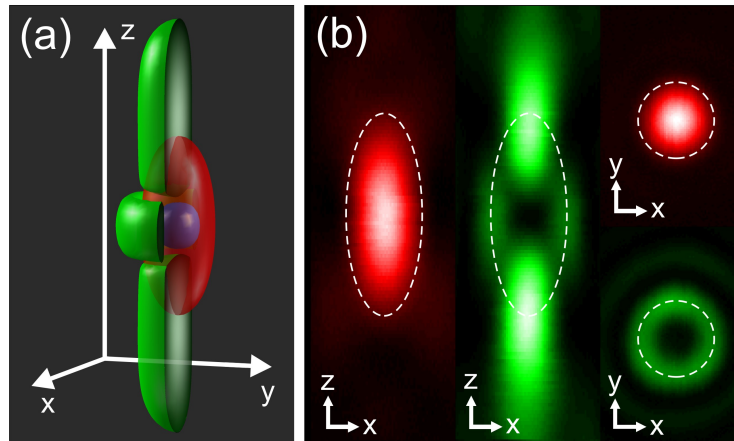


**Figure 3.7.:** Principle of STED-DLW. **(a)** Calculated iso-intensity surfaces of the foci of the excitation (red) and depletion (green) laser. The overlap reduces the effective exposure volume (blue), both in lateral and axial direction. The depletion focus is “cut open” to allow better view on the interior. **(b)** Measured intensity profiles. Taken from [142].

ble feature size and resolution of DLW. One of these tricks was developed in the field of fluorescence microscopy by S. Hell in 1994 [143, 144] and adapted for DLW lithography about 15 years later [145–147]. The technique is called stimulated-emission-depletion-inspired DLW (STED-DLW). The idea is as follows: The non-linear processes that lead to the polymerization of the photoresist occur in a small confined volume, the voxel. Yet, the volume size is limited by diffraction. If one could selectively block the polymerization inside the voxel, the effective polymerization volume would decrease and change shape. Importantly, the process would have to be reversible, so that a volume that was blocked once can be polymerized at another time. The way to do this is to overlap a second so-called depletion laser operating at a different frequency on top of the excitation laser that starts the polymerization. The excitation focus has a Gaussian shape, so that the depletion focus has to be shaped differently in order to suppress the polymerization selectively. The excitation and depletion foci are shown in Fig. 3.7. The shaping is achieved by using a phase mask, which forms the depletion focus so that it has zero intensity at the focal point and increasing intensity in all directions in its vicinity. In this way, the excitation laser will polymerize only a smaller effective volume around the vicinity of the focal point.

But how does the suppression work? The excitation laser brings the photoinitiator molecules from the ground state to an excited state. From there, non-radiative decay or fluorescence can relax the molecule to the ground state again. However, there is a third channel, the inter-system crossing. In fact, this is the channel that starts the polymerization. Therefore, the goal is to suppress this channel. This is done by bringing in the depletion laser. Its frequency is selected such that it can induce stimulated emission from the excited state to

the ground state. However, other photo-induced depletion mechanisms can contribute as well.

In principle, the effective polymerization volume can be made smaller and smaller by increasing the intensity of the depletion laser (which makes the intensity gradient around the focal point steeper). However, the depletion laser itself can be absorbed in the excited state. This and other undesired effects caused by the depletion laser will lead to unwanted polymerization at some point. The optimal balance between excitation and depletion beam has to be found.

In the case of the setup that was used for the fabrication of the structures in this work (see Section 5.3), the excitation laser is a femtosecond-pulsed laser at 810 nm (Mai Tai HP, Spectra Physics), and the depletion laser is a continuous-wave laser at 532 nm (Millennia Xs., Spectra Physics). As a photoresist, we use 7-diethylamino-3-thenoylcoumarin dissolved in the monomer pentaerythritol tetraacrylate. The STED-DLW process has been developed by Joachim Fischer in our group.

In order to compare the performance of regular DLW to STED-DLW, Joachim Fischer has fabricated a grid of fcc woodpile photonic crystals (see Fig. 3.8), where each woodpile has a footprint of  $20\ \mu\text{m} \times 20\ \mu\text{m}$  and consists of 24 layers in the axial direction. The rod distance has been varied from  $a = 250\ \text{nm}$  to  $a = 450\ \text{nm}$ . Notably, the structures fabricated *via* STED-DLW (Fig. 3.8(b)) show brighter colors and appear to be more homogeneous compared to those made by regular DLW (Fig. 3.8(a)). The colors are a sign of a high-quality, open structure and originate in Bragg-reflections. Obviously, STED-DLW is a significant improvement over regular DLW. This visual impression is supported by the optical spectra (normal incidence, unpolarized light) of the woodpiles (Fig. 3.8(c) and (d)). Where the structures fabricated *via* STED-DLW show pronounced stop bands, the DLW structures lack this feature.

Important to our work is the fact that STED-DLW significantly improves the axial resolution, leading to smaller aspect ratios of the voxel. This is a key aspect in the fabrication of extremely small features.

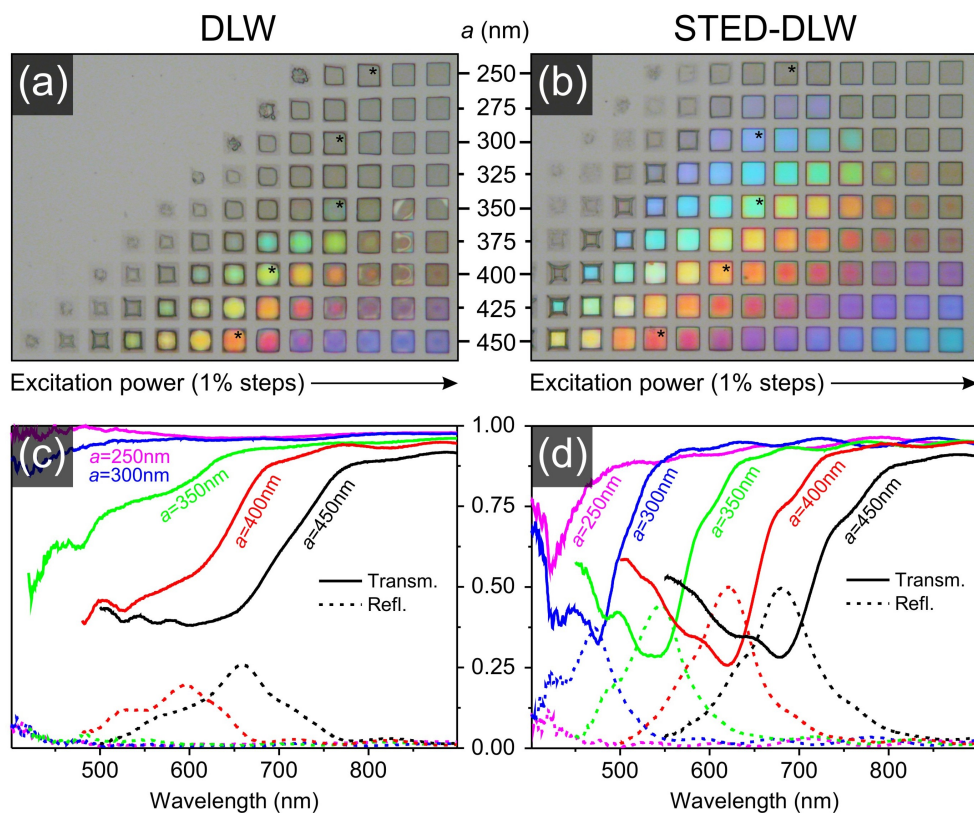


**Figure 3.8.:** (a) True-color reflection mode optical micrographs of woodpile photonic crystals fabricated *via* regular DLW, where  $a$  is the rod spacing. (b) Same as (a), but using STED-DLW. (c) and (d) Selected (see asterisks in (a) and (b)) transmittance (solid) and reflectance (dashed) spectra for DLW and STED-DLW, respectively. Taken from [142].

## 4. Numerical Calculations

### 4.1. Calculation of the Cloak's Index Distribution: Quasiconformal Mapping

In order to perform numerical calculations or experiments on the carpet cloak, it is necessary to derive the needed refractive-index distribution. As mentioned in Chapter 2, there is an infinite number of transformations that solve this problem. In contrast, the number of transformations that are feasible in terms of experimental realization is limited. As shown in Section 2.3, there are several ways of hiding a bump. From these options, the quasiconformal mapping has been the most used and most successful so far. The reason for this is simple: In the quasiconformal map, the local anisotropy of the calculated refractive-index distribution can be minimized to an extent where it becomes neglectable. A locally isotropic index profile remains, which is far easier to create in an experimental situation. Furthermore, this approach allows for arbitrarily shaped bumps.

For our calculation of the quasiconformal map, we follow the lines of the original theoretical description of the cloak by J. Li and J. B. Pendry [96]. Here, a rectangular virtual space with a width  $u$  and a height  $v$  is mapped onto a physical space with the same width and height, but with the bump in it. As before, we denote the coordinates in the virtual space with  $\{x^i\}$ , whereas the coordinates in physical space are denoted with  $\{x^i\}$ . If we restrict ourselves to a two-dimensional wave problem with the electric field pointing in  $z$ -direction, *i.e.*, out of the propagation plane (TE), the  $z$ -coordinate remains unchanged and a general transformation is given by

$$x = x(x', y') \quad (4.1)$$

$$y = y(x', y') \quad (4.2)$$

$$z = z'. \quad (4.3)$$

The corresponding Jacobian matrix is simply

$$\mathbf{J} = \begin{bmatrix} \frac{\partial x}{\partial x'} & \frac{\partial x}{\partial y'} & 0 \\ \frac{\partial y}{\partial x'} & \frac{\partial y}{\partial y'} & 0 \\ 0 & 0 & 1 \end{bmatrix}. \quad (4.4)$$

#### 4. Numerical Calculations

---

The general transformed values for the optical parameters (compare Eqs. (2.66)-(2.67)) in the physical space are

$$\boldsymbol{\varepsilon} = \frac{\mathbf{J}\mathbf{J}^T}{\det \mathbf{J}} \boldsymbol{\varepsilon}_{\text{ref}} = \frac{\mathbf{J}\mathbf{J}^T}{\sqrt{g}} \boldsymbol{\varepsilon}_{\text{ref}} = \frac{\varepsilon_{\text{ref}}}{\sqrt{g}} \begin{bmatrix} \frac{\partial^2 x}{\partial x'^2} + \frac{\partial^2 x}{\partial y'^2} & \frac{\partial x \partial y}{\partial x'^2} + \frac{\partial x \partial y}{\partial y'^2} & 0 \\ \frac{\partial x \partial y}{\partial x'^2} + \frac{\partial x \partial y}{\partial y'^2} & \frac{\partial^2 y}{\partial x'^2} + \frac{\partial^2 y}{\partial y'^2} & 0 \\ 0 & 0 & 1 \end{bmatrix} \quad (4.5)$$

$$\boldsymbol{\mu} = \frac{\mathbf{J}\mathbf{J}^T}{\det \mathbf{J}} = \frac{\mathbf{J}\mathbf{J}^T}{\sqrt{g}} = \frac{1}{\sqrt{g}} \begin{bmatrix} \frac{\partial^2 x}{\partial x'^2} + \frac{\partial^2 x}{\partial y'^2} & \frac{\partial x \partial y}{\partial x'^2} + \frac{\partial x \partial y}{\partial y'^2} & 0 \\ \frac{\partial x \partial y}{\partial x'^2} + \frac{\partial x \partial y}{\partial y'^2} & \frac{\partial^2 y}{\partial x'^2} + \frac{\partial^2 y}{\partial y'^2} & 0 \\ 0 & 0 & 1 \end{bmatrix}. \quad (4.6)$$

Note that in our case,  $\boldsymbol{\gamma}$  and  $\mathbf{g}'$  are the unit matrix, since we start in Cartesian coordinates (compare Eq. (2.63)), and therefore  $\boldsymbol{\varepsilon}^* = \boldsymbol{\varepsilon}$ . We also take advantage of the scalability of the transformation by using a start medium in virtual space with a permittivity of  $\varepsilon_{\text{ref}}$  and a unit permeability, *i.e.*, a dielectric.

We can find the principal values  $\varepsilon_i = \mu_i \varepsilon_{\text{ref}}$  of the optical parameter matrix. Since we are only considering TE polarization for now, the optical parameters of interest are  $\mu_1$ ,  $\mu_2$ , and  $\varepsilon_3$ . The electric component is easy to see from Eq. (4.5) and reads

$$\varepsilon_3 = \frac{\varepsilon_{\text{ref}}}{\sqrt{g}}. \quad (4.7)$$

For the two magnetic principal values, the relationship

$$\mu_1 \mu_2 = 1 \quad (4.8)$$

follows in general after some algebra. The corresponding refractive indices along the two principal axes in the  $xy$ -plane are

$$n_1 = \sqrt{\mu_2 \varepsilon_3} \quad (4.9)$$

$$n_2 = \sqrt{\mu_1 \varepsilon_3}. \quad (4.10)$$

For the purpose of the quasiconformal transformation, it is convenient to introduce a measure for the anisotropy (which we are trying to get rid of). It is given by the anisotropy factor  $\alpha$ :

$$\alpha = \max \left( \frac{n_1}{n_2}, \frac{n_2}{n_1} \right). \quad (4.11)$$

By inserting Eqs. (4.9)-(4.10) into Eq. (4.11) and using Eq. (4.8), we get

$$\alpha = \max (\mu_2, \mu_1). \quad (4.12)$$

It becomes apparent that the minimization of the anisotropy to the lowest possible value, namely unity, also relieves us from the necessity of a magnetic response. This is a very interesting fact. By using a quasiconformal technique, the demands on the material for

an experimental realization have been lowered significantly. Now, a purely dielectric and isotropic material with a permeability equal to unity suffices. Due to the local isotropy, the cloak also becomes independent of the light polarization, which is a crucial prerequisite for a three-dimensional practical cloak. It should also be mentioned that the quasiconformal map approaches the strictly conformal map (see Section 2.3), if the size of the computational domain goes to infinity.

Obviously, we want to minimize the anisotropy ( $\alpha \rightarrow 1$ ). Since Eq. (4.12) holds, it is straightforward to minimize the term

$$\alpha + \alpha^{-1} = \mu_1 + \mu_1^{-1} = \mu_2 + \mu_2^{-1}, \quad (4.13)$$

which has a minimum value of 2 for the isotropic case. After some algebra, we can find that this equation is connected to the metric of space *via*

$$\alpha + \alpha^{-1} = \frac{\text{Tr}(\mathbf{g})}{\sqrt{g}}. \quad (4.14)$$

Furthermore, we define a (geometrically) averaged refractive index by

$$n = \sqrt{n_1 n_2}. \quad (4.15)$$

Using Eqs. (4.9)-(4.10), (4.8), and (4.7), we find

$$n^2 = \sqrt{\mu_1 \mu_2} \varepsilon_3 = \frac{\varepsilon_{\text{ref}}}{\sqrt{g}}. \quad (4.16)$$

This allows for the description of the complete system solely by the anisotropy factor  $\alpha$  and the local refractive index  $n$ .

For a quasiconformal map, we want to reduce the anisotropy to a point where we can simply drop it, *i.e.*, set it to unity. In order to create such a transformation, we again examine Eq. (4.14). This equation relates the current transformation or local compression and deformation of space to the corresponding anisotropy. To calculate the quasiconformal map, we use the squared right-hand side of the equation to create the Modified-Liao functional [148]

$$F = \frac{1}{vu} \int_0^u dx' \int_0^v dy' \frac{\text{Tr}(\mathbf{g})^2}{g}, \quad (4.17)$$

which then has to be minimized. Here,  $u$  and  $v$  are the width and height of the area that is to be transformed. Slipping boundary conditions are used, which means that the outer edges of the transformed area are mapped onto the specified boundaries in the non-transformed area up to a sliding freedom. This sliding freedom introduces a small mismatch of the cloak's refractive-index distribution at the edges and the surrounding refractive index, which turns out to be neglectable for the experiments.

In terms of the numerics, this leads to the following strategy: A Cartesian grid (shown schematically in Fig. 4.1(a)) is defined, which is deformed by “pushing” the bump into the

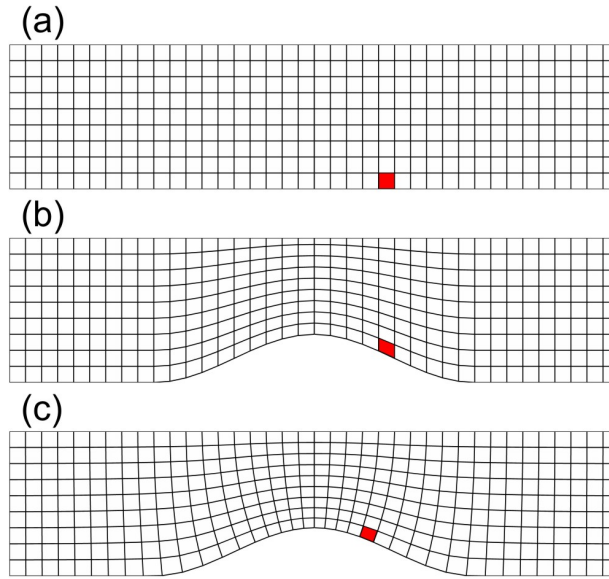


**Figure 4.1.:** Exemplary computation domain for the quasiconformal map. One unit cell (same in (a),(b), and (c)) is marked in red. **(a)** Cartesian start grid. **(b)** Grid after deformation by the bump. Here, only vertical coordinates are changed. Note the anisotropy of the map expressed in the non-orthogonality of the grid lines. **(c)** Final quasiconformal grid after optimization procedure. The local anisotropy is minimized to a point where it can be neglected (see quadratic shape of the unit cells).

domain's bottom (Fig. 4.1(b)). Here, only the vertical coordinates are changed while the horizontal coordinates remain untouched. To illustrate this process, a unit cell is marked in red in Fig. 4.1. Note the transition of the unit cell from a square in Fig. 4.1(a) to a parallelogram in Fig. 4.1(b). This corresponds to a local anisotropy of the refractive index at that position. After optimization, the unit cell in the final grid (Fig. 4.1(c)) is a good approximation of a square again, yet with a smaller area corresponding to a higher refractive index. Importantly, local isotropy is reached. For the optimization process, the local metric  $\mathbf{g}$  of a unit cell in the transformed space is evaluated (it is the scalar product of the local basis vectors:  $g_{ij} = \vec{e}_i \cdot \vec{e}_j$ ) and along with it the corresponding value of the argument of functional  $F$ . The integration of the functional in Eq. (4.17) is replaced by a summation over all unit cells of the area and normalized by the overall number of unit cells:

$$F' = \frac{1}{N_x N_y} \sum_{a=0}^{N_x} \sum_{b=0}^{N_y} \frac{\text{Tr}((\mathbf{g})_{ab})^2}{(g)_{ab}}. \quad (4.18)$$

Note that in this equation,  $(\mathbf{g})_{ab}$  denotes the metric tensor at the computational grid position (a,b). The same holds for its determinant  $g$ . The spatial coordinates of the grid points are free parameters in the minimization of  $F'$ . We calculated the quasiconformal map on a grid consisting of  $160 \times 40$  points. The inner points are completely free to be

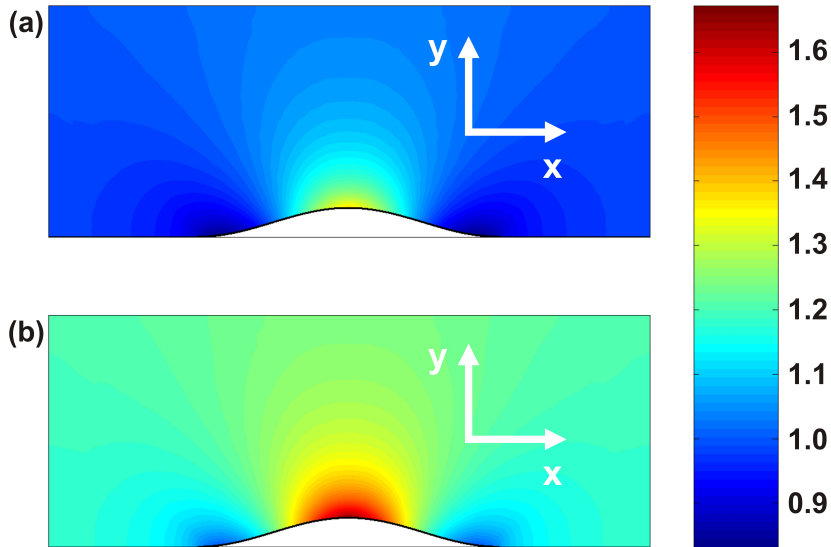


**Figure 4.2.:** Refractive-index distributions of the carpet cloak calculated by means of quasiconformal mapping. **(a)** Initial distribution derived from empty space. Here, refractive index values below unity are found. **(b)** Final distribution derived from a dielectric material with reference refractive index  $n_{\text{ref}} = 1.18$ . The reference refractive index is chosen such that all values of the map are above or equal to unity [104].

moved, the outer points are “stuck” in one direction (slipping boundary condition), respectively. This yields a minimization problem with roughly 12000 free parameters. In order to solve this large problem, we used the genetic algorithm. After the calculation, the map is interpolated to resolutions up to  $16000 \times 4000$  points, depending on the purpose.

Importantly, the minimization of the functional  $F'$  does not only minimize the average anisotropy, but also its maximum. In our case, the average anisotropy factor of the final quasiconformal map is  $\bar{\alpha} = 1.02$ , while the maximum value is  $\alpha_{\text{max}} = 1.05$ . This is sufficiently small to be neglected.

The relevant refractive-index interval of the quasiconformal map depends on the scaling parameter  $\varepsilon_{\text{ref}}$ , on the choice of the bump's parameters (a larger height-to-width ratio means a larger refractive-index interval) and weakly on the size of the computational domain (a very small height of the domain increases the needed refractive index). If  $\varepsilon_{\text{ref}}$  is chosen to be unity, we start in an empty Cartesian space. Consequently, the map exhibits refractive index values below unity (compare “stretched” unit cells with increased area yielding a lower index at both sides of the bump in Fig. 4.1(c)). In terms of an experimental realization using a metamaterial, this again requires metal or resonant structures, which leads to inevitable losses at optical frequencies. Figure 4.2(a) shows the refractive-index distribution derived from the quasiconformal transformation of empty space. We can

evaluate the map for its minimum value  $\varepsilon_{\min}$  and assign a scaling parameter to a new map via  $\varepsilon_{\text{ref}} = 1/\varepsilon_{\min}$ . Here, it takes the value  $\varepsilon_{\text{ref}} = 1.39$ . Figure 4.2(b) shows the scaled version with no refractive-index values below unity. Naturally, the scaled version is based on the fact that the cloak is embedded in the mentioned dielectric medium. No reflections are expected at the interface between cloak and surrounding, if the correct embedding medium is in place. In this case, the border of the cloak is impedance matched. The refractive-index values that are needed to create the scaled version of the carpet cloak are easily accessible by using a structured dielectric material. This will be discussed in detail in Chapter 5.

The carpet cloaks described throughout this thesis consist of a carpet including a bump which is translationally invariant along the  $z$ -direction. Therefore, it can be considered as an extrusion of the  $xy$ -plane shown in Fig. 4.2 in the direction normal to that plane. The bump follows the function

$$y(x) = \begin{cases} h \cos^2\left(\frac{\pi x}{w}\right) & , \text{ for } |x| \leq w/2 \\ 0 & , \text{ otherwise.} \end{cases} \quad (4.19)$$

Here,  $w$  is the full width and  $h$  is the height of the bump.

For the parameters used in the experimental creation of the visible carpet cloak (see Chapter 5), the initial calculation of the quasiconformal map based on empty space yields a refractive-index interval of  $[0.85 \dots 1.32]$ . This translates into a reference refractive index of  $n_{\text{ref}} = 1.18$ . After scaling with this reference index, the index interval becomes  $[1.00 \dots 1.56]$ . This is accessible by a dielectric polymer photoresist. For this calculation, the width of the bump was  $w = 6 \mu\text{m}$  and the height was  $h = 0.5 \mu\text{m}$ . The computational domain has a width of  $u = 20 \mu\text{m}$  and a height of  $v = 5 \mu\text{m}$ .

## 4.2. Finite-Element Calculations of the Carpet Cloak

The functionality of the carpet cloak has been shown for the two-dimensional case in the original theoretical paper of Li and Pendry [96]. Here, the refractive-index distribution calculated using quasiconformal mapping was directly implemented as an effective medium. We reproduced these results (not shown). In order to assess the performance of a full geometry realization in an experiment, *i.e.*, a mapping of the index distribution onto a substructured composite material, we carried out finite-element calculations using the *Comsol Multiphysics* software package. Since Maxwell's equations are scalable, all lengths are given in units of the unit cell size  $a$ . The simulation domain for the calculations has a width of  $75a$  and a height of  $40a$ . The bump follows Eq. (4.19) with a full width of  $12.5a$  and a height of  $1.2a$  [96]. The impinging Gaussian beam is launched from a port, while the calculation domain is surrounded by perfectly matched layers to absorb the wave. The mesh consists of triangular-shaped elements which have a maximum size

of  $0.3a$  in the areas outside the cloak, while they have a size on the order of  $0.05a$  inside the cloak. The overall number of mesh elements is about  $2 \cdot 10^5$  and the total degrees of freedom solved for is about  $5 \cdot 10^5$ . The direct solver *UMFPACK* was used for solving.

### 4.2.1. Performance of the Full Geometry

In the beginning, the idea for an experimental realization of the carpet cloak included the use of a positive photoresist (AZ 9260, MicroChemicals). Here, the exposed parts of the photoresist are washed out during development, while the non-exposed volume hardens during development. Essentially, the idea was to write an array of “air channels” into a polymer, thus forming a metamaterial which exhibits locally controllable optical parameters. The local value of these parameters is tailored by changing the filling fraction or ratio of the constituent materials in the unit cell. If the wavelength of light is larger than the unit cell size, the wave averages over the substructure and “sees” an effective medium with effective optical parameters. We chose the simplest approach by describing the effective material parameters using the Wiener bounds [149]

$$\varepsilon_{\text{eff}} \leq f\varepsilon_1 + (1-f)\varepsilon_2 \quad (4.20)$$

$$\varepsilon_{\text{eff}} \geq \left( \frac{f}{\varepsilon_1} + \frac{1-f}{\varepsilon_2} \right)^{-1}, \quad (4.21)$$

where  $\varepsilon_1$  and  $\varepsilon_2$  are the permittivities of the constituent materials and  $f$  is the filling fraction. In fact, we chose Eq. (4.20) for the design, since both Wiener bounds only differ about 10% from each other for the chosen permittivities  $\varepsilon_1 = 1$  and  $\varepsilon_2 = 2.25$ . For the initial calculations, we used a square unit cell (with width  $a$ ) of polymer including a square air hole (with width  $d$ ). By changing the size of the air hole, a refractive-index interval from  $n = 1$  ( $d = a$ ) to  $n = 1.5$  ( $d = 0$ ) is accessible.

We did not succeed in producing samples with the targeted quality and operational wavelength due to resolution limitations of the positive photoresist. Nevertheless, it is instructive to look at the corresponding numerical calculations, since the design that we used later on for the cloak (a three-dimensional woodpile photonic crystal) is related. A three-dimensional structure can be created by an extrusion of the geometry in the direction normal to the two-dimensional design plane.

Figure 4.3 shows two-dimensional full-wave calculations of the carpet cloak. The structure is illuminated by a Gaussian beam entering from the top left. Here, we use TE polarization. The wavelength is  $4a$ , where  $a$  is the width of the unit cell of the cloak. The upper part of the simulation domain is air in this case. We depict the time-averaged total electromagnetic energy density. At the bottom, a perfect electric conductor serving as a mirror is placed. Figure 4.3(a) shows the reflection of the beam at a flat mirror. Here, a dielectric plate with a reference refractive index of  $n_{\text{ref}} = 1.3$  is placed on top of the mirror. Figure 4.3(b)

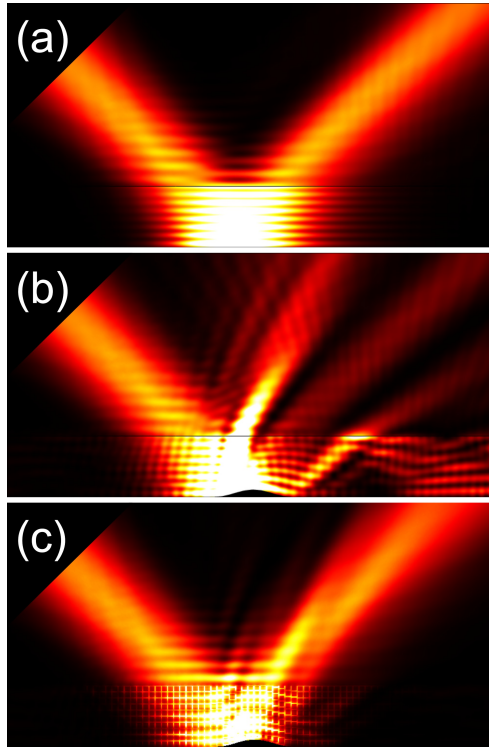


**Figure 4.3.:** Full-wave calculations of the carpet cloak under illumination with a Gaussian beam (entering from the top left) and TE polarization. The time-averaged total electromagnetic energy density is shown. The wavelength of the incoming light is  $4a$ , where  $a$  is the width of the unit cell. **(a)** Reflection of the beam at a flat mirror. **(b)** Reflection at the bump. Note the strong distortion of the reflected beam due to the bump. **(c)** Carpet cloak in full geometry (“air-hole design”). The reflected beam is reconstructed to a large extent.

depicts the strong perturbations introduced to the reflected beam by placing the bump in the mirror. In Fig. 4.3(c), the carpet cloak in the “air hole design” is placed on top of the bump. To a large extent, the original reflected beam is reconstructed. Note the small but finite shift of the beam with respect to the original beam. This effect is due to the quasiconformal mapping of the cloak and has already been mentioned in Section 2.3. In summary, the used composite metamaterial shows a good performance in terms of the cloaking effect.

### 4.2.2. Wavelength Dependence

With later experiments in mind, it is instructive at this point to look at the wavelength dependence of the cloak. Since there is a lower limit for the smallest feature size that can be

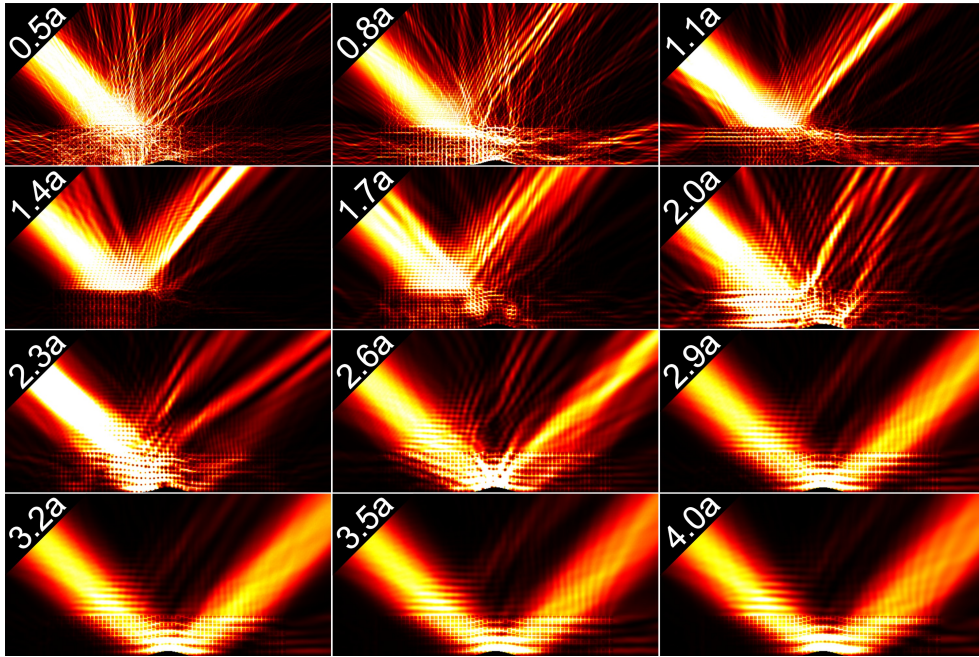


**Figure 4.4.:** Full-wave calculations of the carpet cloak under illumination with a Gaussian beam and TE polarization for a fixed angle of incidence of  $45^\circ$ . The time-averaged total electromagnetic energy density is shown. The wavelength of the incoming light is given in multiples of the unit cell size  $a$  (white numbers).

produced using DLW (which is accompanied by a lower limit for the unit cell size  $a$ ), there will also be a lower limit for the wavelength at which the effective medium approximation breaks down. We performed calculations of the full geometry of the carpet cloak for different wavelengths and for both TE and TM polarization. In the following calculations, the upper part of the calculation domain is glass with a refractive index of  $n = 1.5$ . The results are shown in Fig. 4.4. The wavelength for each individual calculation is noted in units of the unit cell size  $a$  in white numbers. For TE polarization and a wavelength of  $0.5a$ , the incoming light is strongly scattered and diffracted inside the cloak, the result being a wide angle scattering pattern. In principal, the cloak “lights up”. For larger wavelengths, more and more light is reflected at the air/cloak interface. This effect reaches its maximum at a wavelength of about  $1.4a$ . Here, almost no light can enter the cloak and a prominent reflection is visible. Notably, the reflection angle coincides with the incident angle. This behavior is typical for a stop band in a photonic crystal. For even longer wavelengths, we exit the stop band and light can again enter the cloak. Still, diffraction and scattering are dominant processes. Only at around  $2.6a$ , a clear reflected beam starts to form, until finally for wavelengths larger than  $3.0a$  the cloaking effect is very good. Here, we obviously have reached the effective medium limit. The calculations for TM polarization can be found in Appendix A.3. They only differ in details, which means that the cloaking effect for this structure is almost independent of the polarization.

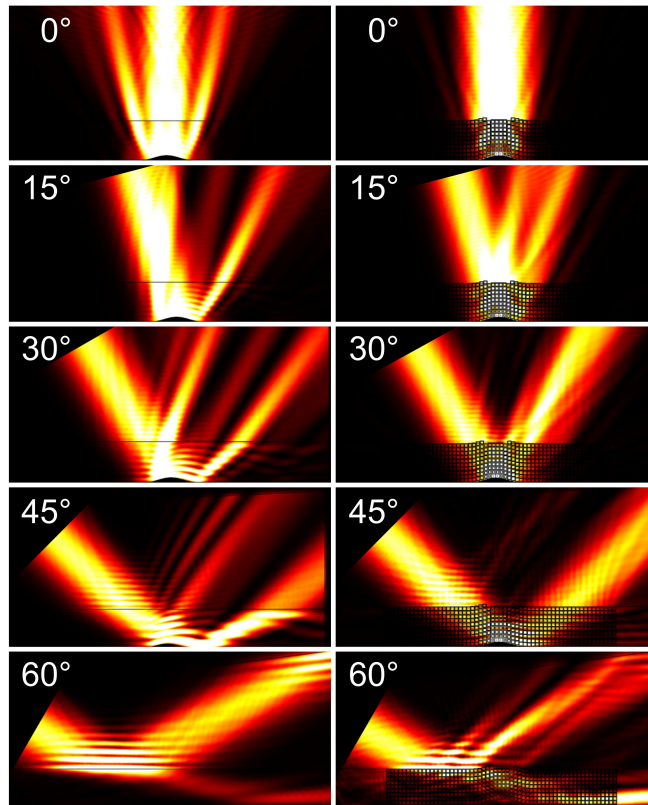


**Figure 4.5.:** Full-wave calculation of a Gaussian beam (TE-polarized) hitting the carpet cloak for different angles of incidence (depicted as white numbers). The left column shows results without cloak, the right column with the cloak in place.

It is noteworthy that it is difficult to assess the overall cloak performance (especially in a far-field imaging situation) from these calculations. For example, we found that the effective medium limit for our experimental woodpile photonic crystal cloak can be shifted more aggressively to shorter wavelengths (see Chapter 5) than one might take from our initial considerations. In other words, the woodpile carpet cloak is more forgiving than we initially guessed.

### 4.2.3. Angle Dependence

After studying the wavelength dependence in the last section, let us now turn to the angle dependence of the cloak. Given the transformation and the resulting quasiconformal mapping, the cloaking effect should be observable for all incident angles [96]. In fact, experiments with microwaves that showed even horizontal propagation of the incident light wave have been performed [101]. In order to check these results, we use the same calculation domain and parameters as in the last section, but vary the angle of incidence. Figure 4.5

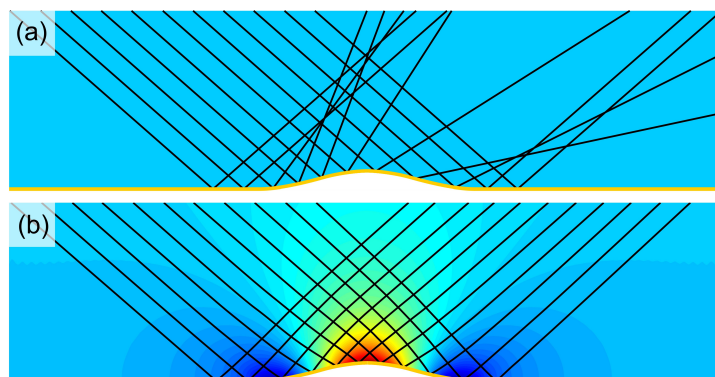


**Figure 4.6.:** Ray-tracing calculations of actual light trajectories **(a)** inside a reference structure with constant refractive index and **(b)** inside the carpet cloak. A parallel bundle of rays enters from the top left in both cases.

depicts numerical results for incident angles ranging from normal incidence ( $0^\circ$  with respect to the vertical axis) to a situation where light is totally internally reflected at the glass-cloak boundary ( $60^\circ$  with respect to the vertical axis). Here again, TE polarization is shown. For all angles below the critical total internal reflection angle, the carpet cloak performance is good and the reflected beam is reconstructed. Even the total internal reflection at an angle of incidence of  $60^\circ$  at the cloak/glass boundary shows that the cloak is still “perceived” as an effective medium by the light wave. Upon comparing both polarization (see Appendix A.3 for the results in the TM case), only minor differences are visible. This is expected for a (nearly) isotropic metamaterial.

With these calculations, we could confirm that the cloak is essentially independent of the incident angle and the polarization of light. Furthermore, we demonstrated that a dielectric photonic-crystal-like geometry can serve as a suitable metamaterial for the design of a cloak. Based on these results and the setback in the fabrication of the “air-hole” design, we created the cloak using a three-dimensional dielectric woodpile photonic crystal using a negative photoresist (see Chapter 5).

### 4.3. Ray Tracing

Before we start with the fabrication of the cloak, it is crucial to assess the functionality and performance numerically. In the last section, we have done so using full-wave finite-element calculations in two dimensions. However, we are interested in a three-dimensional device. But since the full-wave treatment of the cloak solving Maxwell’s equations in three dimensions is out of reach for us, we have to refer to a different method. We use ray tracing, which is capable of describing the cloak (and the measurement setup, if needed) as an effective medium in the geometrical optics limit. Fig 4.6 shows the actual ray-traced

trajectories inside the cloak that were calculated with the numerical procedure presented in this section. They agree qualitatively with the finite-element calculations shown before. We have programmed two different ray tracing codes to perform different tasks, namely the creation of images of virtual macroscopic environments and the comparison of experimental measurement results with theory. In the following, we will explain the concepts of ray tracing and present how such calculations are carried out.

### 4.3.1. General Principle

Nowadays, ray tracing [150] is a rather common technique in geometrical optics to create images with a computer, both for artistical and scientific purposes. Starting in the late 1960's and 1970's [151, 152], the idea of ray tracing has evolved to a point where it is possible to create images which are hardly distinguishable from reality. The general idea of ray tracing (in its simplest form) is the following: In real life, light rays are emitted by a light source, interact with objects and finally hit the observer's eye, which creates the image. Since only a tiny fraction of all the light rays emitted from the light sources involved in a scenery actually would hit the observer's eye, the light path is reversed in ray tracing ("backward" raytracing). This is more efficient by orders of magnitude compared to following all rays emitted by the light source. A point observer is placed in a virtual three-dimensional environment (see Fig. 4.7). A virtual image plane is placed in front of the observer and each pixel is hit by one ray emitted by the observer. For each pixel, the corresponding ray is intersected with the objects in the scenery. Upon hitting the closest intersection point, the ray interacts with the corresponding object. This interaction depends on the properties of the object (reflecting, absorbing, refracting, *etc.*). Afterwards, the ray (which can now have a different direction) is again intersected with all objects and the complete interaction process is repeated. This continues until the ray is absorbed at some point. This ray (and therefore the corresponding pixel in the virtual image plane) then takes on the color value of the absorbing object. The complete image is composed by tracing all rays for all pixels of the image plane.

### 4.3.2. Photorealistic Images of a Macroscopic 3D Carpet Cloak

Section 4.2 analyzed in detail the performance of the carpet cloak with full-wave simulations of the complete structure, yet the calculations were done in a two-dimensional geometry. Therefore, we were interested to see whether a device originally designed for a two-dimensional world would operate in three dimensions and how good the performance would be. Since the cloak's underlying principles are scalable, we choose a macroscopic setting. With this, we arrive at the calculation of photorealistic images of a macroscopic three-dimensional carpet cloak [104] in a real-world scenery. Ray tracing of devices derived from TO is still mainly done "by hand", meaning that a dedicated piece of code is written to perform the task [23, 104, 116, 153]. Available open-source ray-tracing software such as

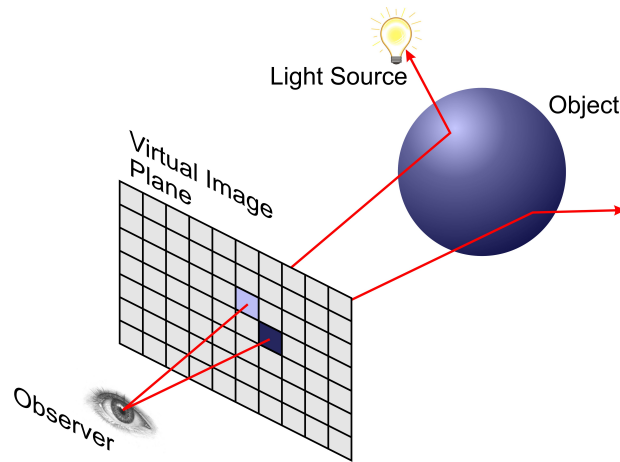


**Figure 4.7.:** General principle of ray tracing. A ray is “shot” from the observer through every image pixel and traced through the scenery.

“POV-Ray” [154] is capable of producing photorealistic images of certain metamaterials, for example materials with a negative refractive index [155]. Yet, it is not able to describe continuously varying refractive-index distributions, which is necessary to model the carpet cloak. Of course, a continuously varying distribution can be discretized in small unit cells in space. The result is an extremely large number of interfaces between these unit cells, all of which have to be intersected. “POV-Ray” is only able to intersect a maximum of 256 interfaces, which is nowhere near the needed number. Thus, a corresponding dedicated computer program was developed (mainly by J. C. Halimeh in the course of his Master’s thesis). The program discretizes the cloak and the continuous refractive-index profile into about  $10^7$  cuboids and traces each ray through the scenery. Snell’s law is applied at every intersection of an external or internal interface. Furthermore, it accounts for reflections from ideal metal surfaces as well as for angle-dependent Fresnel reflections at the outer boundary of the dielectric cloaking structure. Since we assume unpolarized light, the effective intensity reflectance becomes the average of the intensity reflectance of s- and p-polarized light. It is justified to neglect secondary reflections, *i.e.*, rays that get reflected twice or more, since even the primary reflections are quite weak and do not contribute to the images strongly. Reflections at internal interfaces inside the inhomogeneous cloaking structure are also neglected as they should not occur at all for a continuously varying refractive-index profile.

First, let us consider the scenery in which the bump and eventually the cloak is placed. Figure 4.8(a) shows a museum niche with paintings of famous physicists. Lights are placed at the ceiling and the floor can either be non-reflecting and gray, reflecting, reflecting with bump (indicated green in Fig. 4.8), or reflecting with bump and covered by the cloak (indicated red in Fig. 4.8). An observer camera is placed at the end of the room and takes pictures of the niche. Figure 4.8(b) shows the ray-traced image the camera sees for a non-reflecting flat gray floor.

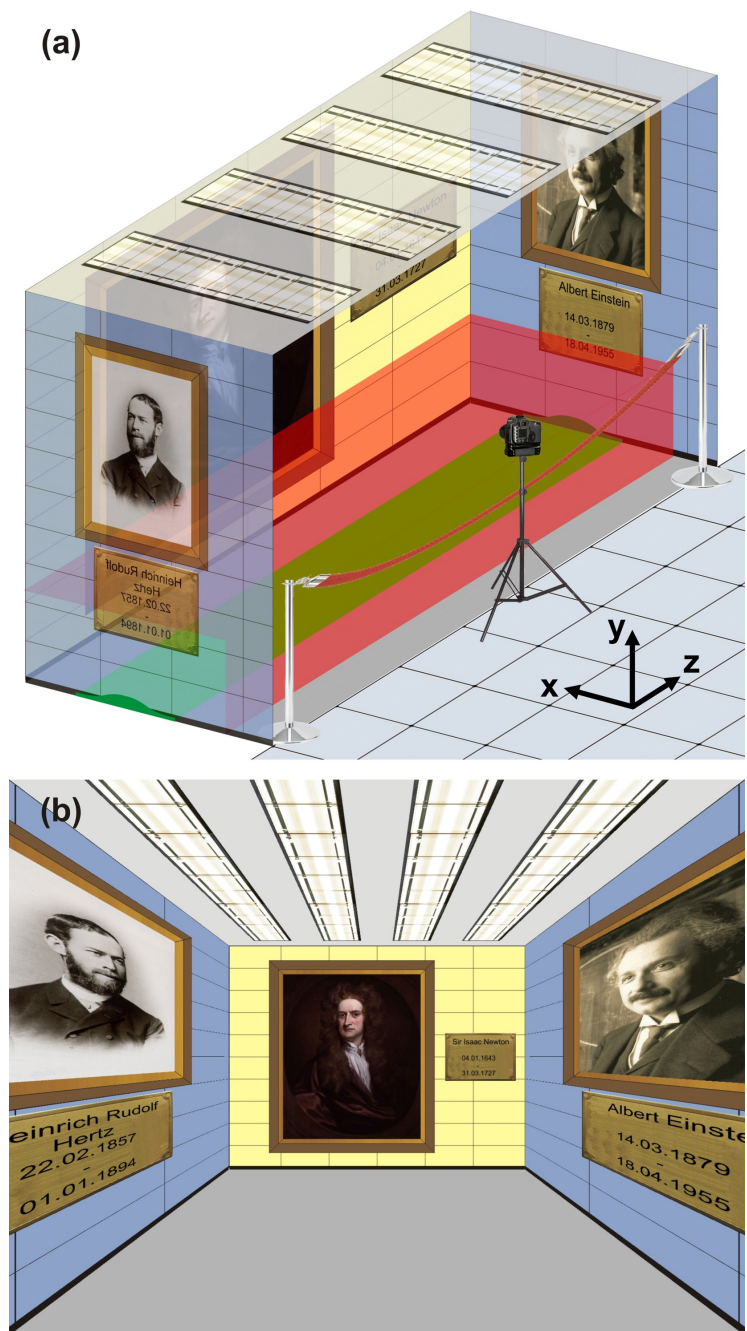


**Figure 4.8.:** (a) Artist's view of the scenery. A virtual camera with large field-of-view images a niche in a museum with portraits of famous scientists representing geometrical optics (Sir Isaac Newton), wave optics and electromagnetic waves (Heinrich Hertz), and quantum optics and general relativity (Albert Einstein), respectively. The bump on the floor (green) and the boundaries of the dielectric cloaking structure (red) are highlighted. (b) Resulting calculated image for a gray floor (*i.e.*, no bump, no cloak, and no mirror) [104].

At this point, it is important to define the field of view (FOV) of the observer camera, since the choice of a certain FOV has a large influence on the images taken. For example, the human total field of view in vertical (lateral) direction in one eye is about  $130^\circ$  ( $169^\circ$ ), but this includes peripheral and ambient areas in the eye image where the eye does not focus. The consciously perceived sharp field of view is much smaller. Since we want to study the performance of the cloak in a fully three-dimensional environment, we do not restrict ourselves to a small FOV, although such small-FOV images would look more realistic in the sense of the human perception. For all images in this section, we choose a vertical (lateral) FOV of about  $118^\circ$  ( $131^\circ$ ) for the camera. This essentially corresponds to a wide-angle lens on the camera. Figure 4.8(b) shows an example for a gray non-reflecting floor without bump.

As described in Section 4.1, the refractive-index distribution of the cloak is scalable. To reflect the character of a possible real-world realization of the cloak, we choose a reference refractive index of  $n_{\text{ref}} = 1.2$ . This avoids index values below unity for the complete cloak, making it possible to construct such a cloak from purely dielectric materials with no or neglectable losses. However, there is one drawback of the scaling procedure. The scaled cloak is now designed to work in a surrounding with refractive index  $n_{\text{ref}} = 1.2$ , yet it is still placed in the room with the refractive index of air being  $n_{\text{air}} = 1$ . Thus, the cloak is perceived as a seemingly homogeneous transparent dielectric plate, since the interface cloak/air leads to refraction and Fresnel reflections. This means that neither the hidden object nor the position of the bump can be seen, yet the cloak itself is visible to some small extent. This effect has been referred to in the literature as the “ostrich effect” [156]. (The ostrich is a large flightless bird native to Africa that is said to sometimes stick its head into the sand, leaving the rest of its body visible.)

To allow for comparison with previous work [101], we choose a bump that follows the known form given in Eq. (4.19) with a ratio of height to width of  $h/w = 9.6\%$ . The overall extent of the entire cloaking structure is  $2w$  in the  $x$ -direction and  $10w/13$  in the  $y$ -direction. The used refractive-index distribution is derived as shown in Section 4.1. Since it was calculated on a mesh with  $104 \times 40$  points, we interpolate the map to a grid with  $5200 \times 2000$  points. This resolution is high enough to serve as a good approximation of the desired continuous distribution. We have carefully checked this assumption and the convergence of the ray tracer by using a test refractive-index distribution which can be analyzed analytically and comparing these results with the numerical outcome. The test distribution has the form  $n(y) = H/y$  for  $0 < y < H$  and  $n = 1$  otherwise, where  $y = 0$  is the floor and  $y = H$  is the top of the structure (see Fig. 4.9). The horizontal displacement  $\Delta x$  at the top of the structure along the  $x$ -direction of a ray under oblique incidence can be found using Fermat’s principle. The analytic result is

$$\Delta x = \frac{2H(1 - \cos \alpha)}{\sin \alpha}. \quad (4.22)$$

Here,  $\alpha$  is the angle of incidence with respect to the surface normal. The numerically computed and the exact analytically calculated displacement are compared for a bundle

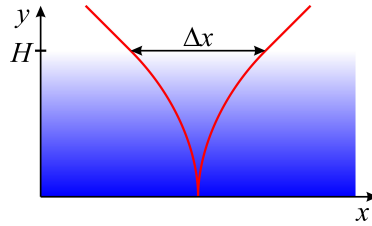


**Figure 4.9.:** Illustration of the distribution that is used for convergence testing. The ray displacement  $\Delta x$  can be derived analytically and compared to the numerical result.

of 470 rays in the  $xy$ -plane with angles of incidence relative to the surface normal between  $31^\circ$  and  $70^\circ$ . We find that the mean relative error asymptotically scales with the number of layers  $N$  according to  $\propto 1/N$ . For example, for  $N = 2000$ , the mean relative error of  $\Delta x$  becomes  $3.44 \cdot 10^{-4}$  (with a standard deviation with respect to the bundle of rays of  $1.8 \cdot 10^{-4}$ ).

The discretization cells for the carpet cloak are translationally invariant in the  $z$ -direction and fill out the complete room in this direction (compare Fig. 4.8). Furthermore, a frequency dependence of the locally varying refractive index (*i.e.*, dispersion) is completely neglected, allowing for color images. This approximation is quite reasonable under the presented circumstances because dielectrics with more or less constant indices in the range of  $n = 1$  to  $n = 2$  are readily available at around visible frequencies. If dispersion would be significant, the sceneries rendered below should simply be viewed as monochromatic images.

It is interesting to compare the performance of two different carpet cloaks with different reference refractive index  $n_{\text{ref}}$ . Figure 4.10 shows rendered images for a reference refractive index of  $n_{\text{ref}} = 1$ . This is the index distribution which directly follows from the quasiconformal mapping without any scaling. On the one hand, no ostrich effect at all is expected in this version of the cloak. On the other hand, the index distribution clearly has values below unit refractive index. For a real-world implementation, this would mean the use of metals or resonant materials, which definitely would lead to larger losses compared to a purely dielectric structure. Figure 4.10(a) simply shows a metallic, hence reflecting, floor. The expected reflections of Newton’s painting are observed without any perturbations. This is what a perfect carpet cloak would look like. Figure 4.10(b) also shows a reflecting floor, but now the bump is introduced. The extent of the bump is outlined with a dashed green line (also compare Fig. 4.8(a)). The effect of the bump’s presence are drastic: Newton’s image is highly compressed and the main visible feature is now the reflection of the ceiling lamps.

On the left and right, the two paintings of Hertz and Einstein, respectively, become visible, and they are strongly distorted. Additionally, the black ribbon at the bottom of the walls is covered by the bump and thus appears disconnected. The cloaking structure is

added in Fig. 4.10(c). This largely recovers the original view in (a). For example, the ceiling (a very obvious distortion) is completely replaced by Newton's painting again. Yet, certain distortions do remain even for a view straight ahead onto Newton's face, which appears slightly shifted. This aspect is likely partly due to the approximation of a locally isotropic refractive index underlying the carpet cloak design. An ideal cloak would require an anisotropic index distribution and even a magnetic permeability different from unity. In fact, small distortions of the carpet cloak are also visible in previously published wave-optics calculations [96]. However, we cannot completely exclude an influence of the finite precision of the refractive-index profile in our numerical calculations. In contrast, we have carefully checked that the ray-tracing is fully converged (see discussion above). The images rendered by ray-tracing simply turn out to be extremely sensitive to even minute details of the refractive-index profile.

As expected from the carpet cloak's original two-dimensional design [96], the cloak should only work perfectly for rays that travel in the vertical  $xy$ -plane (see Fig. 4.8(a)). Only a small portion of rays fulfill that condition in our scenery. For rays that include a large angle with the  $xy$ -plane, the distortions are expected to be larger, which they are indeed. For example, the (originally straight) edges of Newton's name plate are curved in their reflections on the floor. Intuitively, part of these distortions originate from the fact that rays impinging under an angle effectively experience a wider bump, hence a different height-to-width ratio of the bump, leading to an effectively incorrect refractive-index profile. Furthermore, the black ribbon at the bottom of the wall remains disconnected in the shape of the bump. This stems from the fact that light simply cannot hit this part of the scenery due to the presence of the bump, which means that it is impossible to reconstruct that particular part of the image. Nevertheless, the carpet cloak still performs well even under these wide-angle conditions. This surprisingly good performance in a three-dimensional environment sparked the idea for the experimental realization of the carpet cloak, which lead to the first reported three-dimensional cloak (see Chapter 5) at optical frequencies.

Let us now turn to the case of a reference refractive index of  $n_{\text{ref}} = 1.2$ . Here, as discussed before, the ostrich effect is expected to play a certain role in the images. First, one should consider how a perfect cloak would look like. Figure 4.11(a) shows that case. It looks like a homogeneous dielectric plate with a refractive index of  $n = 1.2$ . Thus, the bottom of the rear wall looks bent due to refraction at the air/plate interface. Furthermore, faint (primary) Fresnel reflections are visible, for example just below the name plates of Einstein and Hertz. Therefore, even an ideal cloak (with refractive-index values larger than unity) would reveal its presence. The bump again introduces strong distortions into the reflected image (Fig. 4.11(b)). In the case of the cloak (Fig. 4.11(c)), distortions similar to the unreferenced case remain. Nevertheless, the overall performance of the cloak is still remarkably good.

A tool such as this visualizing ray-tracing code can also be used to investigate further aspects of the carpet cloak. Recently, simplified versions of the carpet cloak have been

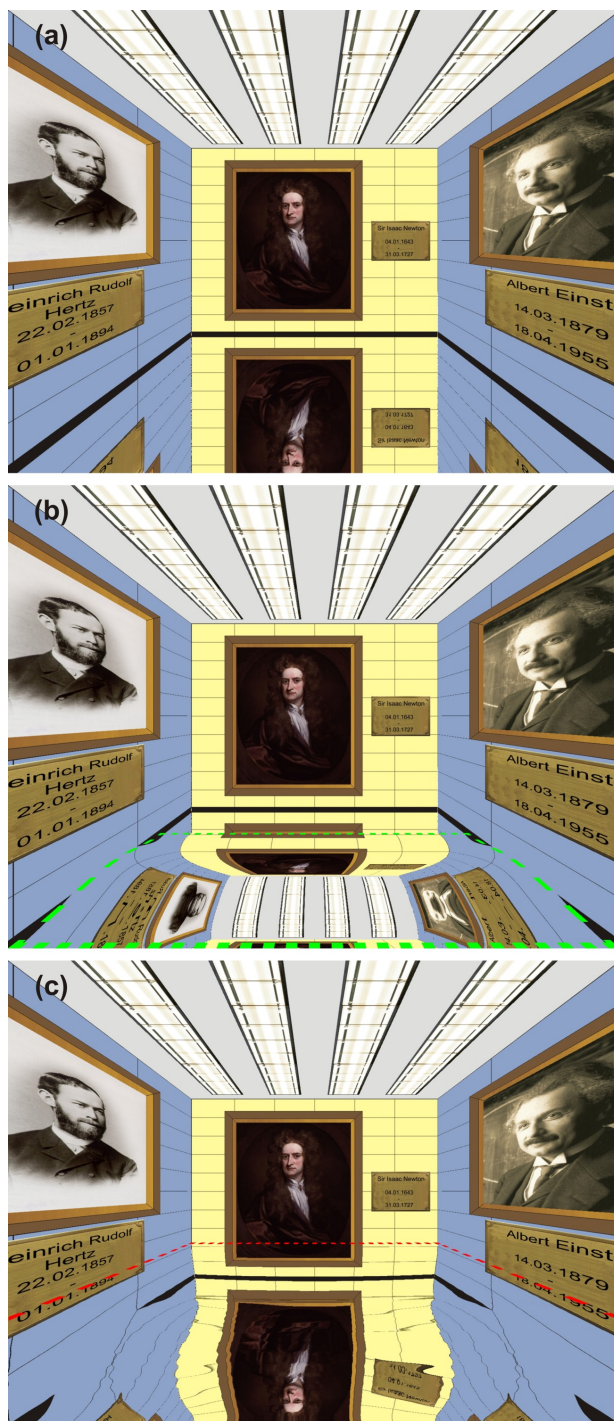


**Figure 4.10.:** Rendered images seen by the virtual camera of Fig. 4.8(a). (a) Metallic (hence reflecting) floor. (b) Same as (a), but with a bump whose edges are outlined in green (see also green outline within cloak in Fig. 4.8). (c) Same as (b), but with the cloaking structure added (top outlined in red). The index distribution is scaled to a reference index of unity [104].

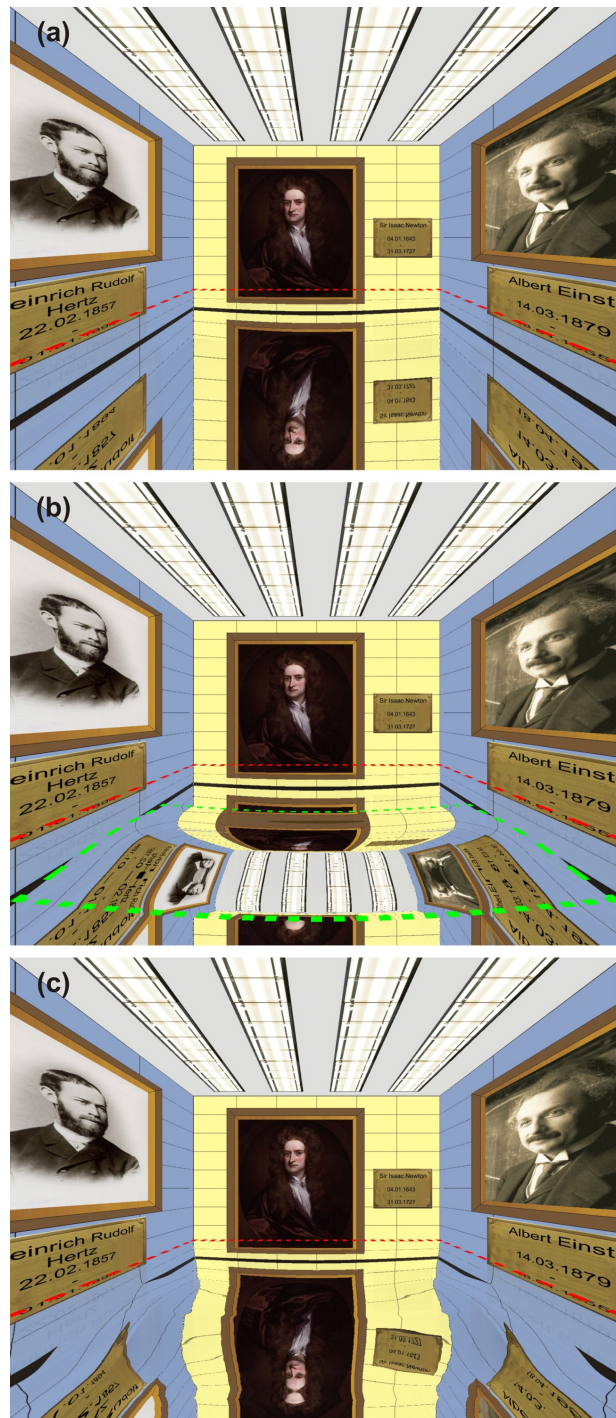


**Figure 4.11.:** As Fig. 4.10 but for a cloaking structure with a reference index equal to 1.2. Unlike in Fig. 4.10, both (a) and (b) include a dielectric plate with the reference index of 1.2 and with the same height as the cloak. In (a)-(b) and (c), the tops of the dielectric medium and the cloak, respectively, are outlined in red [104].

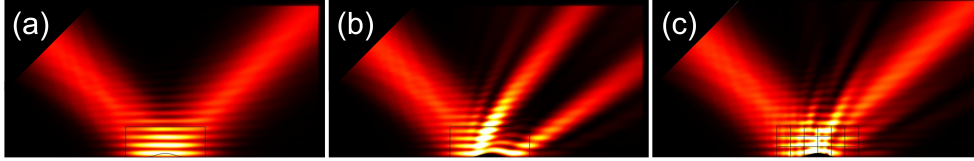


**Figure 4.12.:** Finite-element calculation (*COMSOL Multiphysics*) of the time-averaged total electromagnetic energy density for a simplified carpet cloak under illumination with a Gaussian beam entering from the top left. **(a)** Reflection at a flat mirror. **(b)** Reflection at the bump without cloak. **(c)** Reflection at the bump covered by a simplified cloak consisting of 18 blocks of constant refractive index, respectively.

proposed [102, 103]. Here, the refractive-index distribution that is delivered by the quasi-conformal mapping is approximated by a very coarse grid, leading to only a few “blocks” of different dielectric materials covering the bump. In the mentioned wave-optics calculations [102], the performance of the cloak was rather good. We could reproduce the results with a similar simplified cloak (see Fig. 4.12). Yet, it has to be mentioned that the wavelength of light was comparable to or even larger than the size of the constituent blocks of the cloak. Thus, the light wave tends to average over the structure and is not sensitive to the details. Our ray-optics treatment stands in sharp contrast to that. Since geometric optics is the limit of zero wavelength of light, it is not surprising that our ray-tracing calculations of such a simplified cloak yield a drastically different result. Figure 4.13(a) shows a simplified version (consisting of six blocks) of the full quasiconformal map with a reference refractive index of  $n_{\text{ref}} = 1.2$ . The values of the constant refractive index of each block was calculated by averaging over the corresponding area in the full map. The corresponding rendered image is shown in Fig. 4.13(b). Clearly, the performance of the cloak is rather poor (compare with Fig. 4.11(c)). The performance would be even worse, if partial Fresnel reflections at the interfaces of the blocks, *i.e.*, the interior of the cloak, had been taken into account.

In conclusion, ray-optics calculations are an interesting tool for studying complex media with exotic refractive-index distributions. Since wave-optics calculations for sceneries with sizes many orders of magnitude larger than the wavelength of light are currently way out of reach in terms of computational feasibility, a ray-optics-based approach is presently best suited for visualizing macroscopic sceneries including inhomogeneous media.

### 4.3.3. Ray Tracing of Microscope Images

In the last section, we have presented photorealistic calculations of the carpet cloak in a macroscopic virtual environment. To compare theory with actual experimental results, it is necessary to simulate a complete optical setup [107]. Throughout this section, we use the same parameters (distances, NA, focal length, *etc.*) as in the experimental setup

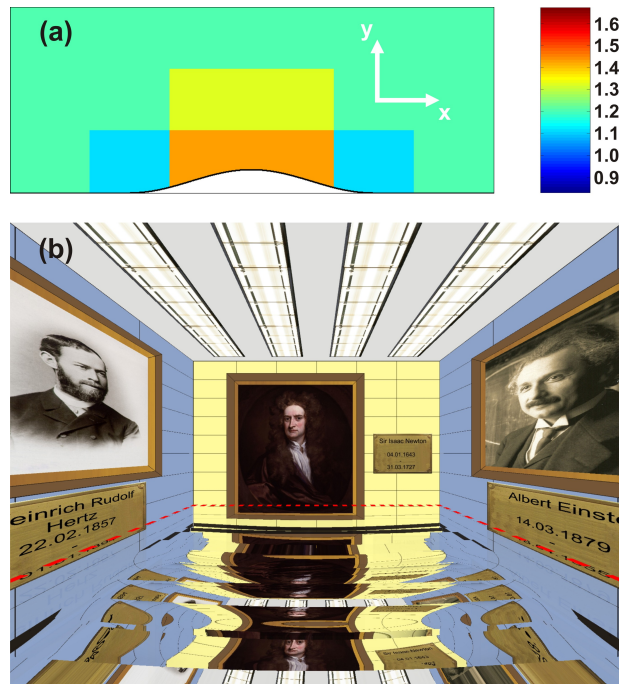


**Figure 4.13.:** (a) Simplified refractive-index distribution roughly mimicking the full quasiconformal map. The reference index is 1.2. (b) Corresponding rendered image [104].

(see Chapter 5). In the ray-optics approximation for the optical elements and the effective-medium limit for the cloaking structure, we use ray tracing to create microscope images. The simulated structures are depicted in Fig. 4.14. Figure 4.14(a) shows the reference structure, which we calculate to be able to assess the effects of the uncloned bump. It has the same geometrical shape as the cloak, yet it exhibits a constant refractive index throughout the entire structure. Importantly, the cloaking structure in Fig. 4.14(b) is surrounded by regions of constant refractive index equal to the reference refractive index of  $n_{\text{ref}} = 1.2$ . This extension of the cloak is necessary to reflect the size of the experimental cloak, which is larger than the actual cloaking region to get rid of perturbing edge effects (see Chapter 5). Within both structures, the refractive-index distribution is constant along the  $z$ -direction. A three-dimensional illustration of the cloaking structure that is treated *via* ray tracing is shown in Fig. 4.14(c).

Although a ray tracer of the type used in the last section can give an impression of a virtual environment, it will not give results close to real experimental data, since it uses a point observer and no explicit illumination model. To be able to compare experimental microscope images (see Chapter 5) with theory, we had to develop a completely new code that was able to handle extended light sources, a variable geometry and optical elements such as lenses. We again used the software *Matlab* for the coding.

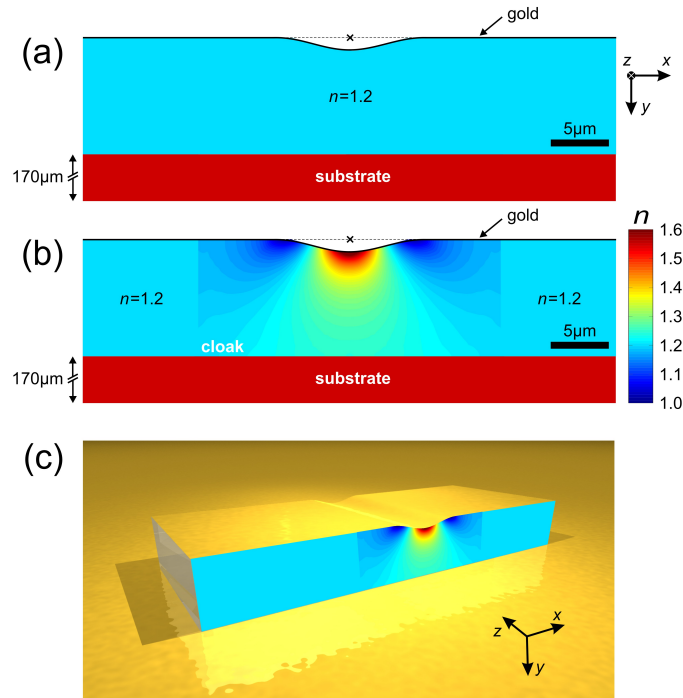


**Figure 4.14.:** (a) False-color representation of the refractive-index distribution of the reference structure within the  $xy$ -plane. Within the structure, the refractive index is constant along the  $z$ -direction. The structure is located on a thick glass substrate. A possible sample rotation axis is parallel to the  $z$ -direction and located at the depicted black cross. (b) Same as (a), but for the carpet cloak structure. On the left- and right-hand side, the cloaking structure is surrounded by regions of constant refractive index equal to the reference refractive index of  $n_{\text{ref}} = 1.2$ . (c) Three-dimensional illustration of the overall structure in (b). Note that the cloak is depicted “upside down” with respect to the last sections, since the image reflects the experimental situation [107].

## Modeling of the Optical Setup

This new piece of code is a statistical non-sequential forward ray tracer. The main idea is to emit light rays from a light source and to follow each ray on its path through a complete optical setup, including microscope objectives, lenses, glass substrate, cloaking structures and mirrors (see Fig. 4.15). On its path, the ray is refracted and reflected according to Snell’s law. The ray eventually hits an observer image plane (the “CCD chip” of this calculation), which has a Cartesian grid on it (“pixels” of the image). In those grid elements, the number of incoming rays is counted. The number of rays per element is a measure for the light intensity and allows for the construction of the final image. In contrast to the code used in the last section, this code is designed as a non-sequential ray tracer. This means that all rays are always intersected with all objects to find the

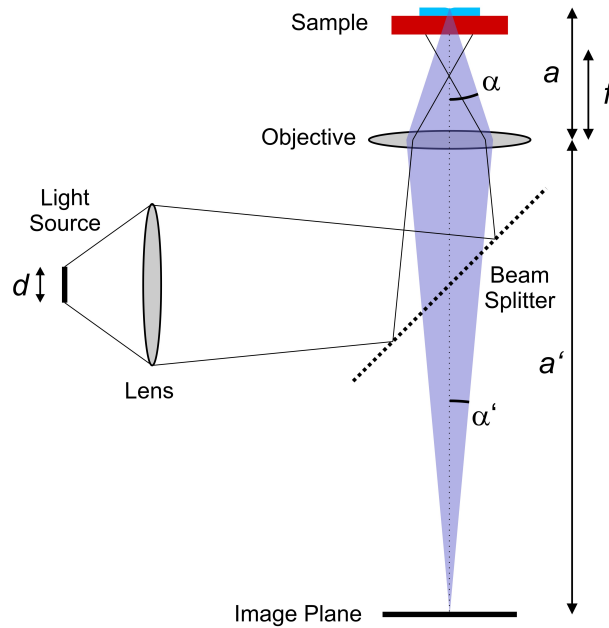


**Figure 4.15.:** Schematics of the optical setup. Note that we image the cloak through the glass substrate, so that the light propagates through the cloak [107].

nearest intersection point. From there on, the ray interacts with this object and the complete procedure is repeated. Such a ray tracer easily handles changes in the geometry of the scenery, in contrast to a sequential ray tracer, in which the order of interactions is predefined.

For the actual ray tracing, the light source can be modeled as a point source or an extended source. For a point source ( $d = 0$ ), the origin of all rays is located at the same point of the optical axis, yet the emission angle is randomly generated for each ray to reflect the properties of an isotropic emitter. For an extended light source, these isotropic emitters are randomly distributed on a disc with radius  $d$  normal to the optical axis. In contrast to the technique of ray tracing described in Section 4.3.1, where image pixels are scanned one after another, this ray tracer is a statistical one: The longer the calculation runs, the more rays are emitted, and the less noisy the calculated images get. The emitted light is collected by a first condenser lens and sent onto the sample via an objective lens. Both lenses are modeled as infinitely thin ideal lenses with no aberrations (see Fig. 4.16). For an ideal lens, any ray (with start point  $O$  and direction  $\vec{v}$ ) is intersected with the lens plane to find the point  $P$ . The direction  $\vec{v}$  of the ray behind the lens is found by constructing a “test ray” (green ray in Fig. 4.16) through the midpoint  $M$  of the lens. By definition, this ray passes the lens undisturbed and by using the lens equation

$$\frac{1}{g} + \frac{1}{b} = \frac{1}{f}, \quad (4.23)$$

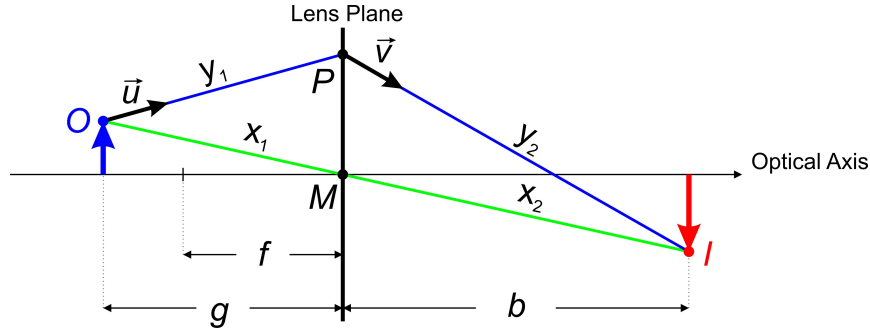


**Figure 4.16.:** Implementation of the lens equation into the ray-tracing code modeling an ideal infinitely thin lens with finite numerical aperture.

the image point  $I$  on this test ray is easily determined. The direction  $\vec{v}$  of the actual ray after the lens is then found by connecting points  $P$  and  $I$ , since all rays emitted from point  $O$  intersect in point  $I$  for an ideal lens.

The objective lens delivers a magnified image of the sample at the image plane. The distance  $a$  (see Fig. 4.15) is chosen such that the magnification factor  $m$  is

$$m = 1 - \frac{a'}{f} = -80, \quad (4.24)$$

which is the case for  $a = 5.4776$  mm. The calculation takes the finite diameters of both lenses into account, yielding a numerical aperture of  $\text{NA} = 0.3$  for the condenser lens and  $\text{NA} = 0.5$  for the objective lens. For the objective lens, which is crucial for the imaging process, this corresponds to a full opening angle of  $60^\circ$ . The  $t_s = 170 \mu\text{m}$  thick glass substrate with refractive index  $n_s = 1.545$ , on which the sample is situated, is also taken into account in our ray-tracing code. This glass substrate introduces a defocus into the system, which has to be corrected in order for the system to still yield a sharp image in the image plane. In real life, this corresponds to an adjustment of the “microscope knob”. For this, the sample has to be moved further away from the objective lens (*i.e.*,  $a \rightarrow a + a_s$ ) by a shift  $a_s$  along the optical axis. A straightforward calculation yields the result

$$a_s = t_s \left( 1 - \frac{\tan(\arcsin(\frac{\sin \alpha}{n_s}))}{\tan \alpha} \right), \quad (4.25)$$

where  $\alpha$  is the angle the ray includes with the optical axis. For rays that can be treated in the paraxial approximation, this expression collapses to

$$a_s = t_s \left( 1 - \frac{1}{n_s} \right). \quad (4.26)$$

For the given parameters, Eq. (4.26) leads to  $a_s = 60 \mu\text{m}$ . Naturally, this means that the glass substrate introduces spatial aberrations into the otherwise ideal optical microscope, which is a well known fact in microscopy.

In the same manner as the glass substrate, the cloaking structure or the reference structure, respectively, introduces an additional defocus. In analogy to Eq. (4.26), we get for the compensational shift

$$a_c = t_c \left( 1 - \frac{1}{n_c} \right). \quad (4.27)$$

For a cloak thickness of  $t_c = 10 \mu\text{m}$  and a reference refractive index of  $n_{\text{ref}} = 1.2$ , this yields  $a_c = 1.7 \mu\text{m}$ . The overall defocus of the system can then be corrected by replacing the original distance  $a$  (compare Fig. 4.15) by  $a \rightarrow a + a_s + a_c$ .

The distance from the illumination source centered on the optical axis to the condenser lens is 44 mm, the distance from the condenser lens to the objective lens is 400 mm. The bump (with and without cloak) is also centered with respect to the optical axis and embedded in a reflecting mirror surface. The bump again follows Eq. (4.19) with a height of  $h = 1.25 \mu\text{m}$  and a full width of  $w = 13 \mu\text{m}$ . Naturally, the bump is also translationally invariant along the  $z$ -direction. The outer dimensions of the complete structure are  $90 \mu\text{m}$  in the  $x$ -direction,  $10 \mu\text{m}$  in the  $y$ -direction, and  $30 \mu\text{m}$  in the  $z$ -direction. Again, this corresponds to the experimentally realized structure (see Chapter 5).

## Phase Tracing

This ray-tracing code is capable of calculating amplitude images using the ray statistics at the image plane. However, numerical treatment of the phase of light is also desirable. Although, strictly speaking, the phase of light has no meaning in the geometrical optics limit, we can attach a “phase” representing the traveled optical path to each ray. We call this “phase tracing”. Each ray has a “memory” of the optical length  $l$  it has traveled. The overall optical length for each ray is calculated by the piecewise summation of all straight geometrical path segments  $x_j$  from one refraction (or reflection) point to the next including the refractive index  $n_j$  in that volume:

$$l = \sum_{j=1}^M n_j x_j. \quad (4.28)$$

Here,  $M$  is the total number of path segments. For the phase tracing, the modeling of the ideal lens (see Fig. 4.16) also plays an important role. By definition, all rays emitted from point  $O$  must have the same phase in point  $I$  after traveling through the lens. The additional optical length  $l_m$  of the midpoint test ray from point  $O$  to point  $I$  is

$$l_m = x_1 + x_2 = \sqrt{(G^2 + g^2)} + \sqrt{\left( \frac{G(g-f)}{f} \right)^2 + \left( \frac{gf}{g-f} \right)^2}, \quad (4.29)$$

where  $G$  is the distance of point  $O$  from the optical axis. The additional path  $l_a$  of the actual ray is  $l_a = y_1 + y_2$ . In order to model an ideal lens, the optical paths for both rays

#### 4. Numerical Calculations

---

have to be the same, *i.e.*,  $l_m = l_a$ . With this, the traveled optical path  $l_r$  of the ray after exiting the lens (in other words, at point  $P$ ) has to be

$$l_r = y_1 = x_1 + x_2 - y_2. \quad (4.30)$$

$x_1$  and  $x_2$  are easily calculated from the test ray, and since we have calculated point  $P$ , the distance from  $P$  to  $I$  is also known and equal to  $y_2$ . From here on, the ray continues to propagate through the setup and picks up additional optical length.

To retrieve the final phase  $\Phi$  of an image plane grid element, a complex adding of all phases  $\phi_j$  (one for each ray  $j$ ) in that grid element is performed:

$$\Phi = \sum_{j=1}^N e^{i\phi_j} = \sum_{j=1}^N e^{i\frac{2\pi}{\lambda}l_j} \quad (4.31)$$

Here,  $N$  is the total number of rays that have hit the grid element,  $l_j$  is the optical length each rays has traveled, and  $\lambda$  is the wavelength of the light. Although it might seem strange to incorporate the wavelength of light (which is zero by definition in the ray optics approximation), it is necessary in order to relate the phase of the ray to the geometrical dimensions of the structure. Phase images retrieved from phase tracing will be compared with experimental data in Chapter 5.

### Propagation Inside the Cloak

The most important part of the ray-tracing code is the treatment of the cloak itself and the handling of reflections. The discretization of space for the cloak is the same as described in Section 4.3.2. Snell's law is applied at every interface and partial Fresnel reflections are neglected since they should not occur inside a structure consisting of a continuously varying refractive-index distribution. In Section 4.3.2, total internal reflections at the discretization interfaces did not occur due to the moderate angle distribution of the incoming rays. In contrast, they play an important role here. In fact, they *have* to be taken into account to model all ray paths correctly.

Figure 4.17 shows a ray that illustrates this necessity. The ray (red) enters from the left and propagates along the bump (black) horizontally. Without the cloak, this ray would obviously hit the bump and be reflected. With the cloak in place, the ray bends downwards and follows the shape of the bump. On arrival at the middle of the bump, which lies on the symmetry axis of the system (dashed line), it has to bend upwards again due to the gradient of the refractive-index profile along the vertical direction ( $n_1 > n_2$  in Fig. 4.17). Here, the index profile exhibits similar characteristics to a mirage, where rays are “deflected” at the decreasing refractive index towards the ground and make thirsty desert travelers believe to see water when in fact they are looking at the sky. The mentioned ray in Fig. 4.17 exits to the right again parallel to the metal film. This behavior is also obvious when the overall

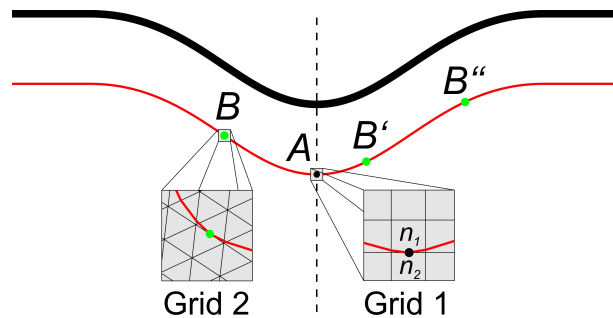


**Figure 4.17.:** A horizontal ray (red) travels along the bump (black) and has to obey mirror symmetry with respect to the symmetry axis of the system (dashed line). For this, the ray has to undergo total internal reflection at some point to “change direction”. The specific point and the occurrence of this effect depend on the type of discretization grid (two examples are shown). The overall trajectory of the ray has to be independent of the type of discretization as long as the mesh size is sufficiently small.

effect of the carpet cloak is considered: If it worked perfectly, all rays would have to exit the cloak as if there was no bump at all. For our ray, this means that it should travel a straight, horizontal line and exit on the same height as it has entered.

This can only be fulfilled if the ray propagating through the cloak undergoes total internal reflection at some point. Interestingly, the actual location of this event depends on the computational discretization of space. Figure 4.17 depicts two different variations of discretization grids or meshes. Grid 1 consists of squares which are aligned along the  $x$  and  $y$ -direction. For this mesh, the total internal reflection occurs at point  $A$  (black dot), as discussed in the above paragraph. For grid 2, which consists of triangles rotated by  $25^\circ$ , the total internal reflection occurs multiple times, namely at points  $B$ ,  $B'$ , and  $B''$  (green dots). In summary, the number of total internal reflections and the locations of these events depend on the discretization of space, yet the overall trajectory of the ray must not depend on it. This is fulfilled for sufficiently small mesh elements.

Finally, partial Fresnel reflections at the physical interfaces (cloak/air, cloak/glass, and glass/air) are neglected. As we have seen in Section 4.3.2, they are of minor importance. Total internal reflections at these interfaces, on the other hand, are important and accounted for. With this scheme, no ray disappears or splits into two. A ray is either completely transmitted or completely reflected at any of the interfaces. On a second note, the ray-tracing code is in principle able to handle multiple partial angle-dependent Fresnel reflections, but the computation time increases drastically.

At this point, it is interesting to discuss the effect of the bump itself, since this is the object to be hidden. More precisely, the distortion of the mirror image due to the bump has to be canceled by the carpet cloak. As will be shown, this characteristic “fingerprint” of the bump in an optical micrograph consists of two dark stripes with a bright maximum

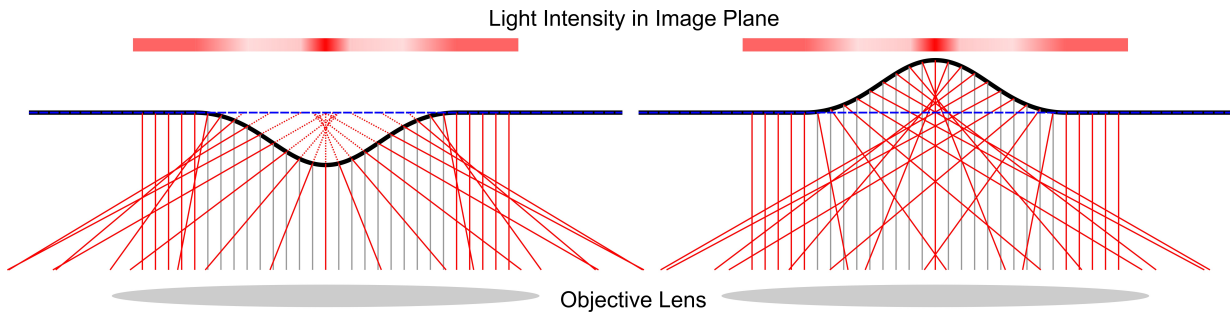


**Figure 4.18.:** *Left:* A metallic bump (black) reflects incoming rays (gray) with a constant spacing between them. This corresponds to a homogeneous illumination. The reflected rays (red) are traced back (dashed red lines) to the focal plane (dashed blue line) and intersected with it. When imaged onto the image plane, the reflected rays seem to originate at these intersection points. The ray density at the focal plane (and thus the image plane) is not constant anymore. Furthermore, some of the rays are not even collected by the objective lens due to the finite numerical aperture and radius. *Right:* Same configuration as on the left side, but for the inverse problem, a dent in a mirror. The effects are identical.

in between. There are two contributions leading to this “fingerprint”. Figure 4.18 shows a schematic drawing of a bump and a dent, which clarifies the origin of this characteristic structure. In the left part, a reflecting bump (black) is shown. A collimated bundle of rays (gray) enters from the bottom through the objective lens. The ray density is constant, *i.e.*, the illumination light intensity is homogeneous. After hitting the mirror, the rays are reflected under various angles (shown in red). The objective lens, which has already served for the illumination, collects those rays and images the focal plane (dashed blue line) onto the image plane. If one wants to know where a light ray will appear as an illuminated pixel in the image plane, one has to trace the ray back to its intersection with the focal plane, since the light ray seems to originate from that position. This is shown with dashed red lines. It is evident that the density of rays in the focal plane is not constant anymore. It is higher at the middle of the bump and lower at the slopes. This varying density of rays in the focal plane translates into a varying density (and thus intensity) in the image plane.

The second contribution to the fingerprint is more obvious: Due to the finite numerical aperture and radius of the objective lens, not all reflected rays hit the lens. These rays are simply not collected and therefore are “missing” in the image plane, leading to more pronounced dark stripes. This effect will be apparent when comparing different numerical apertures of the objective lens later on. Interestingly, the exact same argument also holds true for the inverse problem, a dent in a mirror (see right part of Fig. 4.18).

## Ray-Tracing Results

To familiarize ourselves with the typical distortion of the bump and the overall ray-optics images, Fig. 4.19 shows results for a  $\cos^2$ -shaped bump as described before together with a point light source as illumination and, importantly, without cloak. To make the origin of the double minimum structure even clearer, we also calculate a triangular-shaped bump following Ref. [108] (width  $13\ \mu\text{m}$  and height  $1.25\ \mu\text{m}$ ). Although a point light source does not describe the experimental situation appropriately, it is instructive to use it in the beginning to get an understanding of the image.

Let us start with the top left image in Fig. 4.19. The outline of the sample is clearly visible in the rendered images. This is due to the fact that light rays that are impinging nearly parallel to the optical axis can be totally internally reflected at the outer edges of the sample. Furthermore, a prominent dark double stripe including a bright maximum in the middle is visible. This is the fingerprint of the bump discussed before. For comparison, the top right image in Fig. 4.19 shows the triangular bump. In contrast to the  $\cos^2$ -shaped bump, the slope of the bump is obviously constant, leading only to a shift of a homogeneous “light plate” rather than to an inhomogeneous redistribution of the light intensity. These two plates (one for each side of the triangular bump) are both shifted towards the middle and overlap there, forming a maximum. Here, the intensity distribution in the maximum is homogeneous and larger by a factor of 2 compared to the surrounding. In contrast, the maximum for the  $\cos^2$ -shaped bump shows an inhomogeneous distribution with a maximum intensity value exceeding that of the triangular-shaped bump.

Now, let us examine the performance of the cloak when the sample is tilted. Every row in Fig. 4.19 corresponds to a tilt angle, which is denoted at the left side of the figure. The tilt axis is normal to the optical axis and parallel to the bump (compare small black cross in Fig. 4.14). Two important terms should be introduced at this point: the “bright-field mode” and the “dark-field mode”. Bright-field mode corresponds to a situation with untilted sample (tilt angle  $0^\circ$ ). The name stems from the fact that a flat mirror looks bright when inspected and illuminated at normal incidence, since all the light is directly reflected back and collected by the objective lens. When tilting the sample around the above mentioned axis, only a certain portion of the light will be collected by the lens. This is evident in the second row of Fig. 4.19 at a tilt angle of  $11^\circ$ . Here, the “edge” of the lens is visible. For angles equal to or larger than  $22^\circ$ , we have entered the dark-field mode. In this situation, the mirror deflects the light to the side, where it is not collected by the objective lens any more. Thus, a flat mirror looks completely dark. In our case, the bump is present in the mirror. The slope of the bump changes the angle distribution of the reflected rays. Therefore, even for the tilted case in dark-field mode, light that is reflected off of the bump is collected. The bump appears as a bright stripe (marked with a white arrow in Fig. 4.19). The additional bright stripe next to this bump reflection is again total internal reflection at the side walls of the structure. For a tilt angle of  $44^\circ$ , even

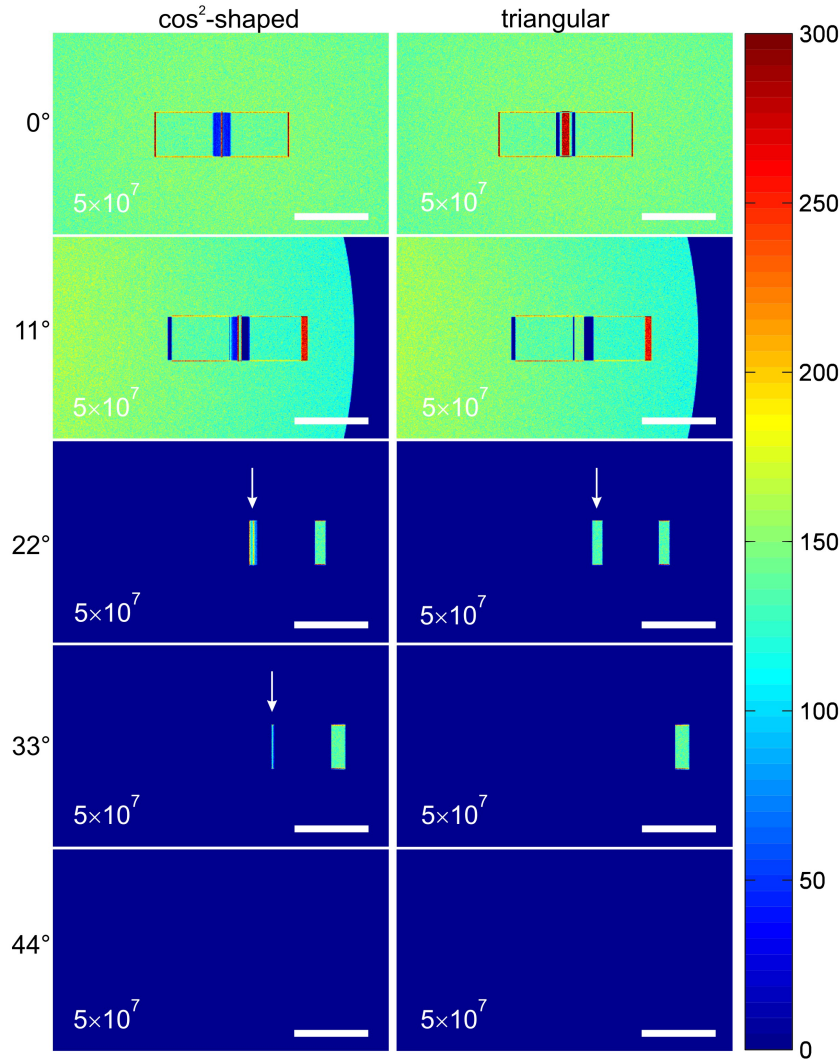


**Figure 4.19.:** Microscope images rendered by ray tracing for the geometry outlined in Fig. 4.15 and for the case of a bump without cloak (see Fig. 4.14a) and for point-source illumination. Images are shown for a  $\cos^2$ -shaped bump (left column) and for a triangular bump (right column). The five rows show different sample tilt angles increasing from top to bottom. Zero-degree tilt angle corresponds to the bright-field mode, large angles to the dark-field mode. The local image intensity is false-color coded. The values quoted on the right-hand side correspond to the total number of rays that have hit a square pixel element in the image plane, the area of which corresponds to  $0.5 \mu\text{m} \times 0.5 \mu\text{m}$  in the sample plane. The total number of rays that have illuminated the sample through the objective lens is given by the white number in the individual panels. The white scale bar shown in all panels corresponds to  $50 \mu\text{m}$  in the sample plane. The white arrows point to the scattering of light off the bump. Within the ray-optics approximation, the depicted images do not depend on wavelength at all [107].

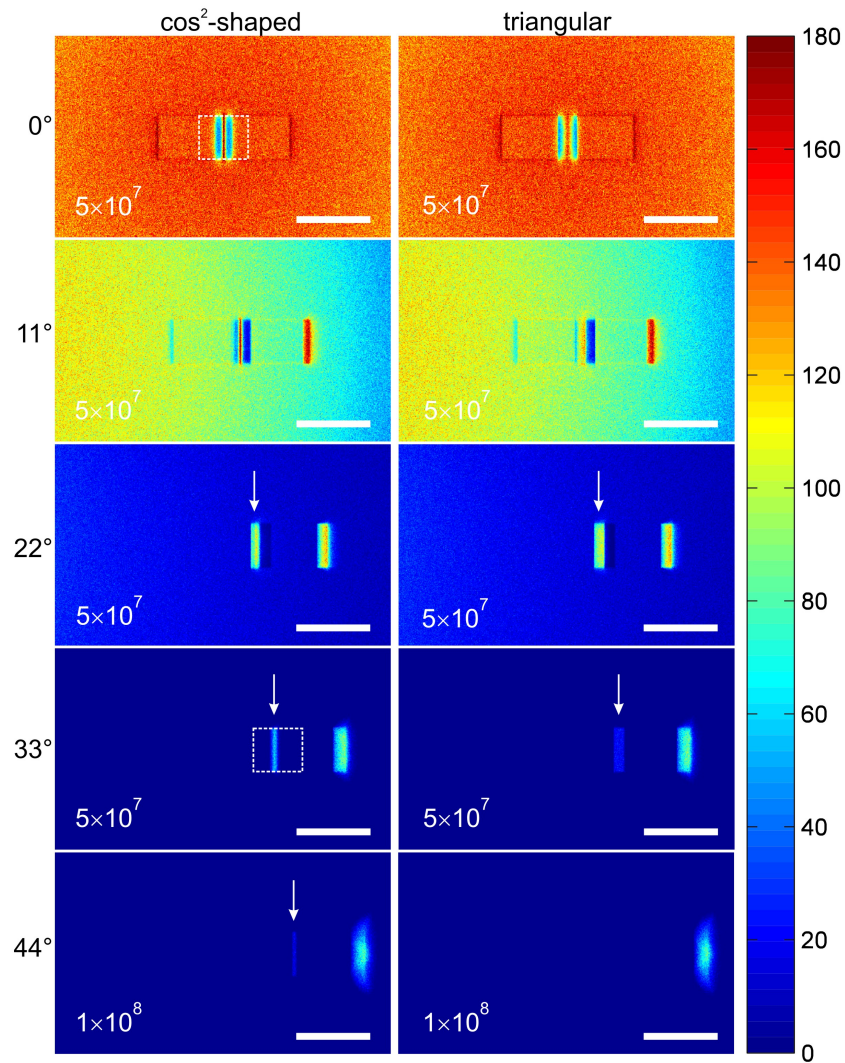


**Figure 4.20.:** Rendered microscope images as in Fig. 4.19, but for a finite disk-shaped light source with diameter  $d = 5$  mm (see Fig. 4.15) rather than for point-source illumination. The dashed white rectangles outline the depicted areas in Figs. 4.21 and 4.22 [107].

the light reflected at the bump slopes is not collected any more. Notably, the reflection for the triangular-shaped bump vanishes at smaller angles. This is consistent with the fact that the slope of the triangular-shaped bump is smaller than the maximum slope of the  $\cos^2$ -shaped bump by a factor of  $\pi/2$ .

All of the above considerations also hold true for the extended light source (see Fig. 4.20). Yet in this case, the features of the image are smeared out. Also, the triangular-shaped bump is still visible at  $33^\circ$  tilt, which is due to the fact that the angle distribution of the illumination rays is larger for the extended source. The same is true for the  $\cos^2$ -shaped bump at  $44^\circ$ .

After discussing the case without cloak, let us now consider the cloaked case. Fig 4.21 compares the cases with and without cloak for the bright-field mode and for the dark-field mode, respectively. To emphasize the important information, we restrict the images to the relevant central part with bump and cloak or the part that shows the bright scattering off of the tilted bump, respectively. The areas shown in Fig. 4.21 are outlined as dashed rectangles in Fig. 4.20. Furthermore, we only show the  $\cos^2$ -shaped bump.

To be able to compare the performance of the cloak, the first row in Fig. 4.21 shows the reference structure without cloak for the bright-field mode ( $0^\circ$  sample tilt) and for the dark-field mode ( $35^\circ$  sample tilt as in Ref. [106]). The second row shows the cloak. A perfect cloak would yield the image of a flat mirror, which in this case would be a homogeneously distributed light intensity. For the bright-field mode, it is apparent that the cloaking performance is very good. For the dark-field mode, the cloaking performance is excellent as well. The bright scattering off of the bump without cloak (marked with a white dashed line in Fig. 4.21) almost completely disappears with cloak. It is reduced by more than one order of magnitude and is therefore not visible on the depicted scale. The much dimmer bright stripe to the left of the bump in the cloaked case has a different origin. To be able to compare the ray-tracing calculations with experimental results (see Section 5), we extended the lateral dimensions of the structure by adding to the refractive-index profile derived from the quasiconformal mapping a region of constant refractive index (equal to the reference refractive index of 1.2) to the left and to the right (compare Fig. 4.14(b)). Since the quasiconformal map does not have the exact value of the reference refractive index at the boundaries of the map (slipping boundary conditions, see Section 4.1), there is a fairly small but finite refractive-index discontinuity. At these interfaces, total internal reflections of light rays that are nearly parallel to the optical axis can occur. These discontinuities are visible as small intensity variations on the left and right edges in bright-field mode.

Up to now, the numerical aperture of the objective lens for these calculations has been  $\text{NA} = 0.5$ , which corresponds to a full opening angle of  $60^\circ$ . Since it is very easy to change the numerical aperture in these calculations, it is interesting to ask whether it has any influence on the image. A larger numerical aperture means that the structure is probed by rays from more directions in three-dimensional space. Here, a numerical aperture of  $\text{NA} = 1$  would correspond to a full opening angle of the cone of light of  $180^\circ$ . The numerical

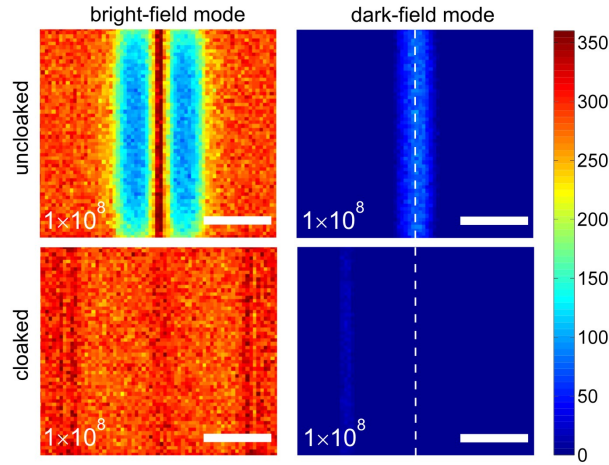


**Figure 4.21.:** Microscope images for the bright-field mode (left column) and the dark-field mode with  $35^\circ$  sample tilt (right column) without (first row) and with carpet cloak (second row), all rendered by ray tracing. The objective lens numerical aperture is  $NA = 0.5$  (see Fig. 4.15). The refractive-index distribution underlying the carpet cloak is shown in Fig. 4.14. A total number of  $10^8$  rays have illuminated each sample. The scale bar corresponds to a length of  $10 \mu\text{m}$  in the sample plane. The area of the image shown here is outlined in Fig. 4.20. The dashed white line marks the position of the bump reflection in both dark-field images [107].

aperture of the objective lens is controlled by simply changing its diameter. Figure 4.22 shows results for  $NA = 0.7$  (full opening angle of  $89^\circ$ ) and  $NA = 0.9$  (full opening angle of  $128^\circ$ ). All other parameters are identical to those in Fig. 4.21. We only show the bright-field mode in Fig. 4.22 because a flat mirror no longer appears completely dark for sample angles of  $35^\circ$  at such large numerical apertures. The contrast of the bump fingerprint obviously decreases with increasing numerical aperture from  $NA = 0.5$  in Fig. 4.21 to  $NA = 0.7$  and  $NA = 0.9$  in Fig. 4.22. As pointed out in previous paragraphs, the double minimum structure originates from two sources. Firstly, the light intensity is redistributed due to the slope of the bump. Secondly, some light rays are not collected by the finite-sized objective lens. The redistribution of light is unaffected by any changes in the numerical aperture. The second reason, on the other hand, is directly influenced by the numerical aperture. Therefore, a larger numerical aperture collects more light rays, which can “fill up” the minima. A numerical aperture of  $NA = 1$  would collect all reflected rays, leaving the redistribution of light intensity as the only source for the bump’s fingerprint. Obviously, the cloaking performance remains excellent for larger numerical apertures. However, one should also bear in mind that the spatial imaging aberrations introduced by the dielectric glass substrate in the optical path of the microscope are expected to play a certain role at such large numerical apertures. These aberrations may obscure the images to some extent.

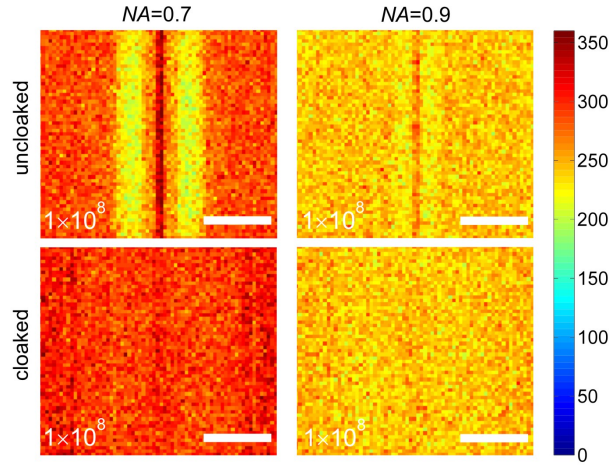


**Figure 4.22.:** Microscope bright-field images as in the left column of Fig. 4.21 (with  $NA = 0.5$ ), but for a numerical aperture of the objective lens of  $NA = 0.7$  and  $NA = 0.9$  as indicated. For these cases, the light samples a much larger fraction of all possible directions in three-dimensional space [107].

Finally, one might ask why the surrounding background intensity decreases for increasing numerical apertures. This is due to the fact that in order to get comparable results, all calculations in Figs. 4.21 and 4.22 were carried out with the same number of illumination rays, *i.e.*, the same number of rays that have hit the objective lens and traveled towards the sample. Since the diameter of the lens at larger numerical apertures is much larger, the fraction of rays that hit the lens but do not contribute to the region of interest also gets larger. Thus the overall lower intensity at higher numerical-aperture values.

In conclusion, the numerical calculations presented in this chapter have shown that the carpet cloak should in fact show a good performance as a fully three-dimensional structure. The ray-tracing calculations provide the means to compare theory with experiment, which will be shown in the next chapter.

## 5. Experimental Results

This chapter presents the main body of this work, namely the experimental realization of three-dimensional polarization-independent broadband invisibility cloaking devices and their characterization. We will start with the description of the cloaking structure itself and discuss its fabrication. Afterwards, we will present the optical setup that was used for the characterization of the cloak at infrared wavelengths, followed by the corresponding measurement results. In the subsequent section, we will turn to the second (miniaturized) version of the carpet cloak operating at visible wavelengths. The optical characterization of this “visible” cloak will be shown, including parameter studies of the cloak’s performance. We will study the wavelength dependence as well as angle and focus dependence of the cloaking effect. A comparison between the experimental data and numerical calculations will also be presented. Finally, we will end this chapter by demonstrating full-wave cloaking that includes not only the light amplitude, but also the light phase. This last step is a crucial and very sensitive test in order to assess the ability of the cloak to hide objects from external detection completely. As before, we will compare the measured cloaking of the light phase with numerical calculations.

### 5.1. Blueprint and Fabrication of an Invisibility Cloak at Infrared Wavelengths

For the fabrication of the carpet cloak, we use a commercially available negative photoresist (IP-L 44, Nanoscribe GmbH) and a commercial DLW (see Section 3.3.1) lithography instrument (Photonic Professional, Nanoscribe GmbH). The samples are fabricated on a  $22\text{ mm} \times 22\text{ mm}$  glass substrate with a thickness of  $170\text{ }\mu\text{m}$ . Most of the samples of the infrared carpet cloak were fabricated by Dr. Nicolas Stenger in our group.

Let us begin with the blueprint of the cloak shown in Fig. 5.1. The overall dimensions of the structure are  $90\text{ }\mu\text{m}$  in length ( $x$ -direction),  $10\text{ }\mu\text{m}$  in height ( $y$ -direction), and  $30\text{ }\mu\text{m}$  in width ( $z$ -direction). The bump follows the shape given in Eq. (4.19) with a width of  $w = 13\text{ }\mu\text{m}$  and a height of  $h = 1\text{ }\mu\text{m}$ . In order to get the best measurement results, we have extended the actual cloak along the  $x$ -direction and added a homogeneous surrounding. This provides us with a “longer carpet” for the measurement and avoids undesired effects due to the edge of the structure. The cloak itself is only  $26\text{ }\mu\text{m}$  long in the  $x$ -direction.

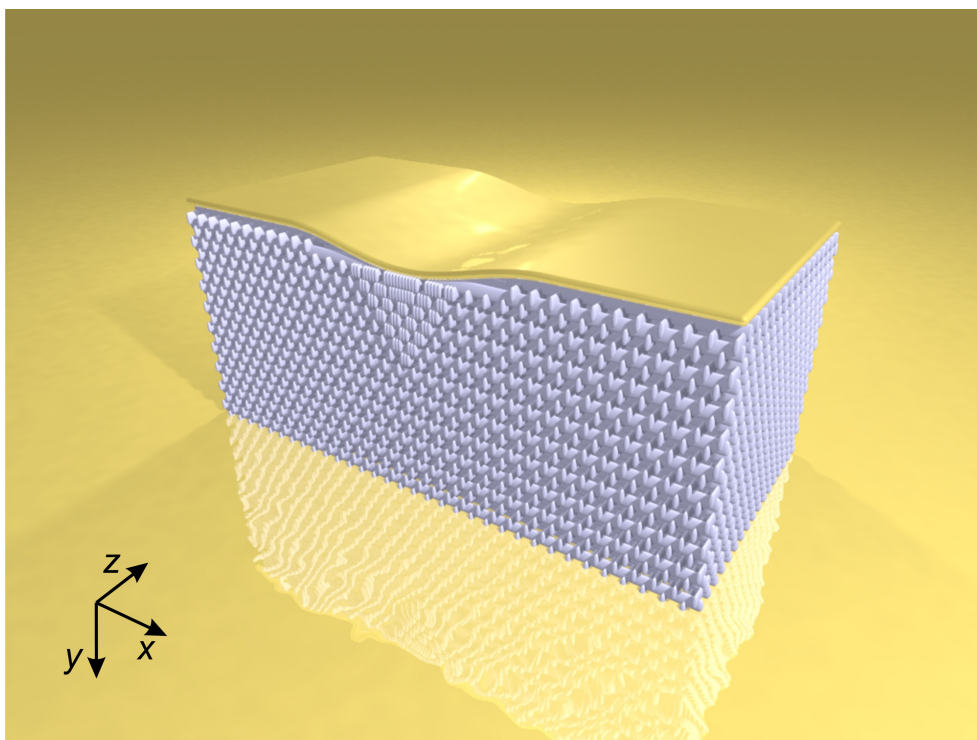


**Figure 5.1.:** Schematic illustration of the three-dimensional carpet cloak. A woodpile photonic crystal in the long-wavelength limit with varying local filling fraction of polymer and air is used as a metamaterial to implement the carpet cloak's optical parameters. Note the higher polymer content below the bump and the lower polymer content on its sides. The polymer cloak including the carpet and the bump are fabricated on a glass substrate *via* DLW and afterwards coated with 150 nm gold. Note that the structure is depicted as it is fabricated, *i.e.*, upside down with respect to the numerical calculations in Section 4.1. The cloak is actually measured from below, *i.e.*, through the glass substrate. For the measurement, we use a microscope objective with a numerical aperture of  $\text{NA} = 0.5$ , corresponding to a full opening angle of the collected light cone of  $60^\circ$ .

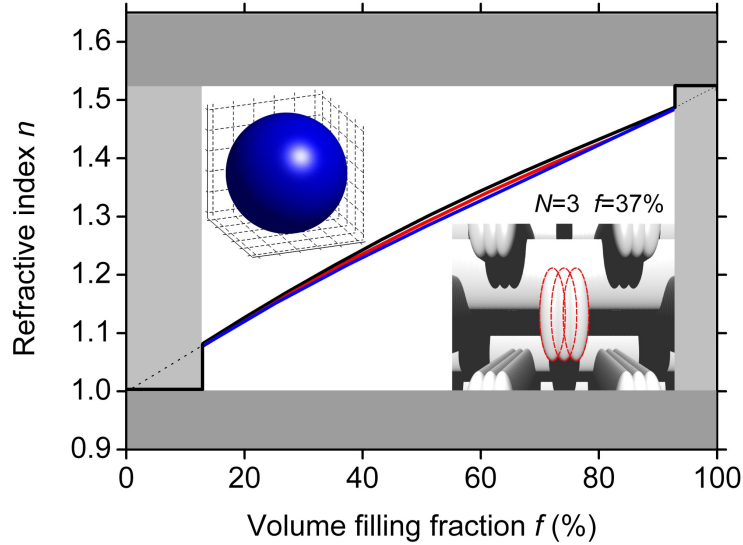


**Figure 5.2.:** Mapping of the polymer-air filling fraction  $f$  onto the effective refractive index  $n$  of the woodpile photonic crystal. Calculations were performed with the *MPB* package. The black, red, and blue curves correspond to a rod aspect ratio (= height/width) of 1, 2, and 3, respectively. The dark gray areas show the limits of the refractive index of the constituent materials, whereas the light gray areas show the limitations due to the intrinsic geometry of the woodpile. Different filling fractions are realized by the number  $N$  of voxels that are used to form one rod. The inset on the lower right shows an example for  $N = 3$  corresponding to  $f = 37\%$ . For this case and for a vacuum wavelength of  $2.4 \mu\text{m}$  and a rod spacing of  $800 \text{ nm}$ , the upper left-hand side inset depicts the nearly spherical isofrequency surface in wave vector space [106].

We compose the cloak of a dielectric fcc woodpile photonic crystal (see Section 3.2) with a rod distance  $a = 800 \text{ nm}$ . Here, each rod consists of overlapping line exposures (see right inset in Fig. 5.2). In the long-wavelength limit, the photonic crystal can be regarded as a metamaterial (see Section 3.1), since the electromagnetic wave averages over the substructure for sufficiently large wavelengths. We simply use the woodpile arrangement of polymer rods to control the local refractive index by changing the filling fraction  $f$  of polymer and air in a unit cell. The effective refractive index becomes  $n = 1.52$  for  $f = 1$  (bulk polymer) and  $n = 1.00$  for  $f = 0$  (air void). Intermediate values of  $f$  lead to intermediate values of the refractive index in the interval  $[1 \dots 1.52]$ . The filling fraction of each unit cell is controlled by the size of the rods. This size, on the other hand, is given by the number  $N$  of voxels written next to each other. Subsequently to the complete woodpile structure, we write a thin layer of polymer (the carpet) on top of it. After the lithography process (which takes about three hours for one structure), the samples are developed in

## 5. Experimental Results

---

isopropyl alcohol for 15 minutes and subsequently dipped into acetone to remove any remaining staining. The last step in the fabrication process is to deposit a 150 nm thick gold film onto the structure using a sputter coater (108 auto, Cressington). This metalizes the polymer carpet and turns it into a “carpet mirror”.

In order to map the filling fraction in a unit cell to the corresponding refractive index, we have evaluated the effective local refractive index of the woodpile on the basis of photonic-band-structure calculations using the *MPB* package [134]. For this, we did a linear fit to the first band around  $k = 0$  and derived the effective refractive index from the slope of this fit. Figure 5.2 shows the results of this calculation. The mapping of the filling fraction  $f$  onto the refractive index  $n$  has been done for three different aspect ratios (height/width) of the polymer rods. Since the focus of the laser in the DLW process is elongated along the axial direction (see Section 3.3.1) resulting in an elliptical cross section of the rods, we calculated with aspect ratios of 1, 2, and 3, respectively. We found that the influence of the actual aspect ratio on the effective refractive index is neglectable. In our case, the standard DLW procedure with the used photoresist and a single voxel usually results in an aspect ratio of 2.7. However, there are limitations to the implementation of the carpet-cloak refractive-index distribution (see Fig. 4.2) with the woodpile photonic crystal and the DLW technique. Obviously, the rods have to be connected to support each other and to give rise to a joined structure. Free-floating elements are not possible with the DLW technique. Therefore, a lower threshold exists for the accessible filling fraction. This is represented as a light gray area on the left side of Fig. 5.2. Additionally, the woodpile rods start to grow together at high filling fractions, preventing the encapsulated photoresist from being removed. This opposes another threshold at the upper boundary of the filling fraction, again shown in light gray on the right side of Fig. 5.2. This introduces discontinuous steps into the theoretically smooth mapping of the filling fraction to the refractive index. However, this is not a significant drawback, since the mapping is implemented in a stepwise fashion, anyway. In fact, we only use  $N \in \{0, 3, 4, 5, 6\}$  for this implementation. The inset in the lower right of Fig. 5.2 shows an example for  $N = 3$  voxels, resulting in a filling fraction of  $f = 37\%$ .

Furthermore, the *MPB* calculations revealed an important property of the woodpile photonic crystal: its isofrequency surfaces in wave vector space are nearly spherical in the long-wavelength limit. The isofrequency surface for a vacuum wavelength of  $2.4 \mu\text{m}$  and a rod-spacing of 800 nm is shown in the upper left inset in Fig. 5.2. This is important for the implementation, since the carpet cloak’s refractive-index distribution is isotropic. Therefore, the constituting metamaterial has to be isotropic as well.

In Fig. 5.3, we depict optical and electron micrographs of the cloaking structure. Note that there is always a second structure right next to the cloak. This is the reference sample, or just “reference”. It is fabricated as a measure of the distortion that the bump introduces to the light that is reflected at the mirror. With this, we make sure that the object that we are trying to hide (namely the bump) is actually visible, and we can also measure the distortion pattern of the uncloaked object. The reference consists of the same woodpile

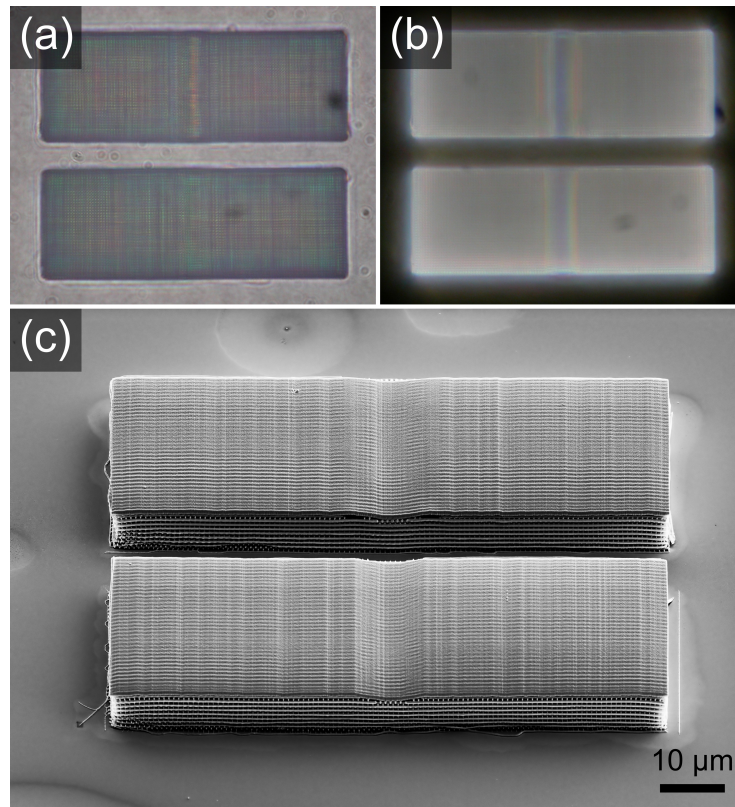


**Figure 5.3.:** Optical micrographs of the cloak (top) and the reference (bottom), as seen from the air side. **(a)** This image is taken in transmission mode before sputtering of the sample with gold. Note the homogeneity of the reference throughout the structure. For the cloak, the area around the bump is visible due to the gradient change in the filling fraction. **(b)** Same as (a), but for dark-field reflection mode of the microscope. Since only scattered light components are collected, the bump is now also visible for the reference. **(c)** Electron micrograph of the same structures as in (a) and (b), but after sputtering. The change in the filling fraction can only be seen when the structures are cut open to reveal the interior (see Fig. 5.4).

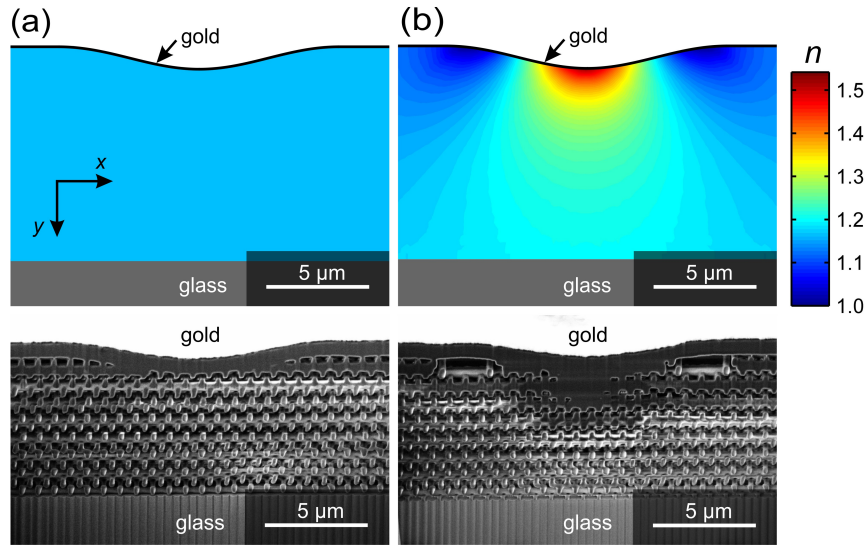


**Figure 5.4.:** The target refractive-index distributions for the fabricated structures are depicted in the top row. In the bottom row, electron micrographs of structures that have been cut open in the middle along the  $x$ -direction *via* focused-ion-beam milling are shown. (a) This column depicts the reference structure. Note the homogeneous filling fraction throughout the complete sample. The remaining inhomogeneity in  $y$ -direction is due to the angle of the FIB cut. (b) This column depicts the cloak. The mapping of the refractive index to the filling fraction is clearly visible by the higher polymer content below the bump and the air voids at both sides of the bump [106].

photonic crystal as the cloak with the exception that it has a constant filling fraction. This gives rise to a constant refractive index throughout the structure. We choose the index to be equal to the reference refractive index of the underlying quasiconformal map. The reference structure can simply be thought of as a nominally identical bump with a homogeneous dielectric on top of it, *i.e.*, no cloak. Figure 5.3(a) shows an optical micrograph *before sputtering* in transmission mode. The structure at the top is the cloak with the reference below it. At a rod distance of 800 nm, the woodpile structure and its horizontally and vertically aligned rods are clearly visible. Also note that the bump is barely visible in the case of the reference. For the cloak, the bump is much more prominent since the characteristics of the woodpile are changed in the vicinity of the bump due to the gradient filling fraction change. In Fig. 5.3(b), optical micrographs in dark-field reflecting mode are depicted, again before the sample was sputtered with gold. Since the dark-field mode only sees the scattered components of the reflected light, the bump is now also clearly visible for the reference. Finally, Fig. 5.3(c) shows electron micrographs of the same structures as in (a) and (b) after sputtering. Note that the sometimes imperfectly terminated outermost ending of the rods at the sides of the structures often obscure the view onto the actual distribution of polymer rods at the inside.

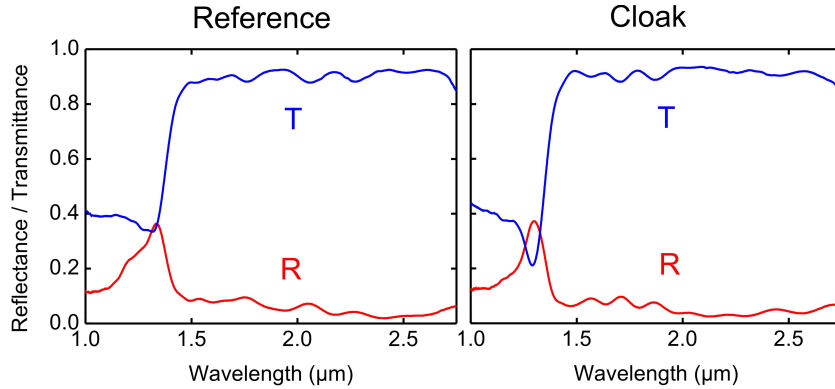


**Figure 5.5.:** Transmittance and reflectance spectra taken with a Fourier-transform microscope-spectrometer. Both reference and cloak show a pronounced stop band at around  $1.4\ \mu\text{m}$ . Only at wavelengths longer than that can the woodpile photonic crystal potentially act as an effective medium metamaterial. The oscillations in transmittance and reflectance are attributed to Fabry-Pérot resonances between the carpet and the glass surface.

To assess the polymer distribution, the structures have to be cut open *via* focused-ion-beam milling (FIB). This is shown in Fig. 5.4. In Fig. 5.4(a), the homogeneous refractive index of the reference structure is shown. Note that the thickness of the glass substrate is not to scale (it is  $170\ \mu\text{m}$  thick). Below, an electron micrograph of a reference structure is shown. It has been cut open *via* FIB along the  $x$ -direction to reveal the interior. As expected, the image shows that the woodpile photonic crystal has a constant filling fraction. The woodpile is open (which means that the rods are nicely separated without any residual photoresist in between) and the structure is highly periodic. These are signs for a good sample quality. In Fig. 5.4(b), the calculated refractive-index distribution for the cloak is shown. The electron micrograph of the cut-open cloak reveals the mapping to the polymer filling fraction. Below the bump, an area of thicker polymer rods up to small bulk polymer blocks is visible. This reflects the high-index area in the map. At the sides of the bump, small holes are visible. Here, the refractive index has to go to unity. Between these mentioned high-index and low-index areas, there is a gradual change of the filling fraction. Note that the polymer carpet has a finite thickness due to the fabrication technique, whereas in theory it should be infinitely thin.

Another way to assess the quality of the woodpile is to measure the optical transmission and reflection spectra. In a woodpile of good quality, pronounced stop bands should occur (also see Section 3.2). We measured the spectra of both cloak and reference. In both cases, we avoided measuring close to the bump, since this would influence the spectrum. In the case of the cloak, there is not even a well-defined photonic crystal here, since the filling fraction changes gradually. For the measurements, we used a commercial Fourier-transform microscope-spectrometer (Equinox 55, Bruker). The results are depicted in Fig. 5.5. Both reference and cloak clearly show a stop band at a wavelength of around  $1.4\ \mu\text{m}$ . Here,

the transmittance exhibits a dip while the reflectance peaks. At larger wavelengths, the woodpile is transparent with a transmittance of roughly 90%. Inside and below the stop band, it is clear that the woodpile cannot be used as an effective metamaterial any more. The effective medium limit is a crucial property that determines the performance of the cloak. The actual spectral position of this limit strongly depends on the system and its geometry. A conservative estimate that is usually considered is that the wavelength of light should be an order of magnitude larger than the period or lattice constant of the metamaterial. If we apply this estimate to our woodpile with a rod distance of  $a = 800$  nm and a lattice constant of  $c = \sqrt{2}a = 1.13$   $\mu\text{m}$  in stacking direction, we end up in the long-wavelength infrared or thermal imaging region around 11  $\mu\text{m}$ . The most optimistic approach that one can consider is the onset of diffraction in the periodic structure. Here, the metamaterial can certainly no longer be considered as a homogeneous effective material. If we want to estimate the involved wavelengths, we can consider light under normal incidence. Here, diffraction occurs when the material wavelength is equal to or smaller than the lattice constant. For a rod periodicity of  $a = 800$  nm and a glass-substrate refractive index of  $n = 1.5$ , diffraction is expected to occur at 1.2  $\mu\text{m}$  vacuum wavelength. This estimate using arguments of diffraction at a grating is one of the most aggressive ones. However, the decisive factor remains the spectral position of the stop band.

Note that for wavelengths above the stop band, oscillations in the transmittance as well as in the reflectance are clearly to be seen. We attribute these oscillations to Fabry-Pérot resonances in the small cavity that is formed between the carpet and the glass surface. These oscillations are more or less pronounced depending on the sample quality.

We can tell from the spectra of the woodpiles that they become transparent above 1.4  $\mu\text{m}$ . At which wavelengths they act as a good effective-medium metamaterial can only be determined when the cloaking effect itself is measured.

## 5.2. Setup and Measurement Results for the Infrared Cloak

### 5.2.1. Optical Setup

Let us start by describing the optical setup that is used for the measurements of the carpet cloak at infrared wavelengths. Fig. 5.6 shows a schematic drawing of this setup. We use an incandescent lamp and, therefore, unpolarized white light as illumination. The emission spectrum of the used light bulb is very close to the theoretical black-body radiation at a temperature of 1600 K. Since we are measuring with a broad spectrum, we have to make sure that chromatic aberrations are minimized. For this, we use calcium fluoride optics throughout the complete setup. This material has a very high transmission (around 95%

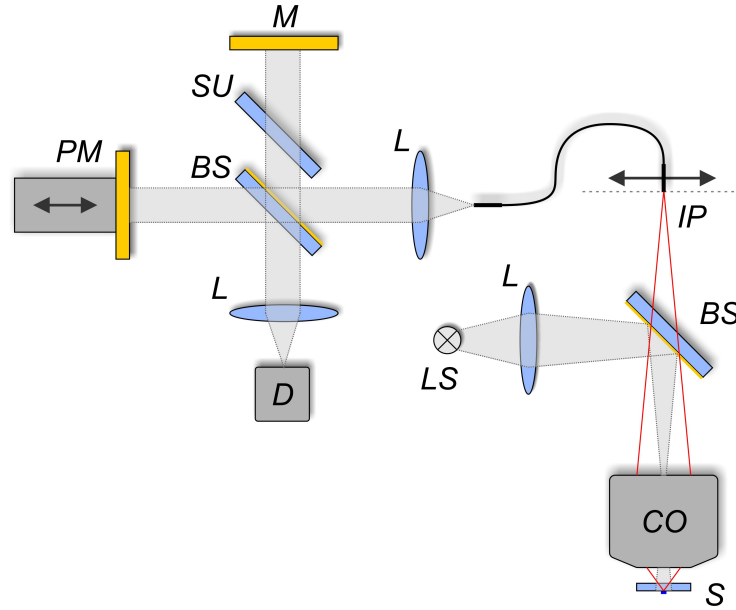


**Figure 5.6.:** Schematics of the optical setup used for the measurement of the infrared cloak. *LS*: Light source *L*: Lens *BS*: Beam splitter *CO*: Cassegrain objective *S*: Sample *IP*: Image plane with end of fiber mounted on microstepper *SU*: Bare substrate *M*: Mirror *PM*: Piezo mirror *D*: Detector.

from 200 nm to 8  $\mu\text{m}$  for a thickness of 1 mm) and a rather flat dispersion and is ideally suited for this purpose. Standard fused silica optics would not be suited for this setup since they exhibit an absorption peak at around 2.2  $\mu\text{m}$ , which is right in the middle of our measurement window. We image the filament of the light bulb onto the microscope objective. This ensures that the sample is illuminated quite homogeneously. In front of the objective, a beamsplitter is placed so that the same objective can be used to collect the reflected light from the sample. The home-made beamsplitter consists of a  $\text{CaF}_2$  substrate with a thickness of 6 mm, on top of which we have deposited 5 nm of gold *via* electron beam deposition. This beamsplitter exhibits a good reflection to transmission ratio throughout the complete spectral interval of interest. For the microscope objective, we use a Cassegrain lens with a focal length of  $F = 5.41$  mm and  $\text{NA} = 0.5$ . This NA corresponds to a full illumination angle and full viewing angle of about  $60^\circ$ . The use of this lens primarily avoids any chromatic aberrations in the imaging process of the sample. The Cassegrain objective creates an image of the sample plane at the image plane with a magnification factor of 80. To measure the spatial and spectral dependence, we scan one end of a multimode chalcogenide-glass optical fiber (CIR-340/400, A.R.T. Photonics, 340  $\mu\text{m}$  fiber core diameter, transparency between 1 and 6  $\mu\text{m}$  wavelength) across the image plane in the direction which corresponds to the  $x$ -direction of the sample. For this, we use a computer-controlled microstepper. The light emerging from the other end of the fiber is collimated and sent into a home-built Fourier-transform infrared-spectrometer. Therefore, we measure the complete spectrum at each spatial position. The Fourier-transform infrared

spectrometer consists of a Michelson interferometer with a piezo-controlled shiftable mirror in one arm. By linearly translating the arm, an interferogram is recorded which can then be Fourier-transformed to get the spectrum. In the spectrometer, we use another home-made beamsplitter of the same type as before. In fact, a second  $\text{CaF}_2$  substrate is introduced into one arm of the spectrometer to compensate for dispersion and to make sure that a symmetric interferogram is measured. The detector of the spectrometer is a liquid-nitrogen-cooled InSb detector (J10D-M204-R01M-60-SP28, Judson Technologies). It has sufficient sensitivity up to  $2.7\ \mu\text{m}$  wavelength.

### 5.2.2. Measurement Results and Discussion

Let us now turn to the measurement itself. In Section 4.3.3, we already introduced the bright-field and dark-field mode. To recapitulate briefly, in bright-field mode the sample includes an angle of  $90^\circ$  with the optical axis. Here, a flat mirror looks bright, since all of the light is reflected back and collected by the objective. In this measurement, the spectral characteristics of the illumination source is still included. Furthermore, the illumination of the sample may not be perfectly homogeneous. To eliminate these spectral and spatial characteristics of the illumination, the measured data is divided by the reflection from the gold film on the bare glass substrate taken right next to the structures. For the dark-field mode, we tilt the sample with respect to the optical axis by  $30^\circ$  along an axis parallel to the bump. This is the largest angle that is possible without the sample glass substrate touching the objective. Here, reflected light is normally not collected by the Cassegrain objective, since the angle under which it leaves a flat mirror is too large. Only scattered light is collected. We divide the measurement data of the dark-field mode by the same reference as in the bright-field mode.

In the following, we will present the measurement results of the infrared carpet cloak. Fig. 5.7(a) shows the data for the bright-field measurement. The horizontal axis is a spatial coordinate which indicates the fiber tip's position along the  $x$ -direction. The vertical axis displays the spectral information at each point. Let us examine the reference first. It shows a clear "fingerprint" of the bump (compare Section 4.3.3), namely a double minimum in intensity along the cross section scan, in the spectral interval from  $1.4\ \mu\text{m}$  to  $2.6\ \mu\text{m}$ . Above  $2.6\ \mu\text{m}$ , the chalcogenide fiber shows very sharp spectral features, which cannot be normalized completely due to slight changes in these features from measurement to measurement. At wavelengths of around  $1.4\ \mu\text{m}$ , the double minimum vanishes. This can be explained by entering the stop band (compare spectral data in Fig. 5.5). Here, the reflectance peak leads to the fact that less light reaches the bump in the first place. If we consider even shorter wavelengths at around  $1.1\ \mu\text{m}$ , we leave the stop band and reflectance goes down again. In this regime, light is scattered and diffracted strongly (*e.g.*, into the glass substrate), so that the portion of light that is actually collected by the finite numerical aperture of the objective decreases. Note that Fabry-Pérot oscillations are also visible in this measurement. Let us now examine the cloak's measurement result. For

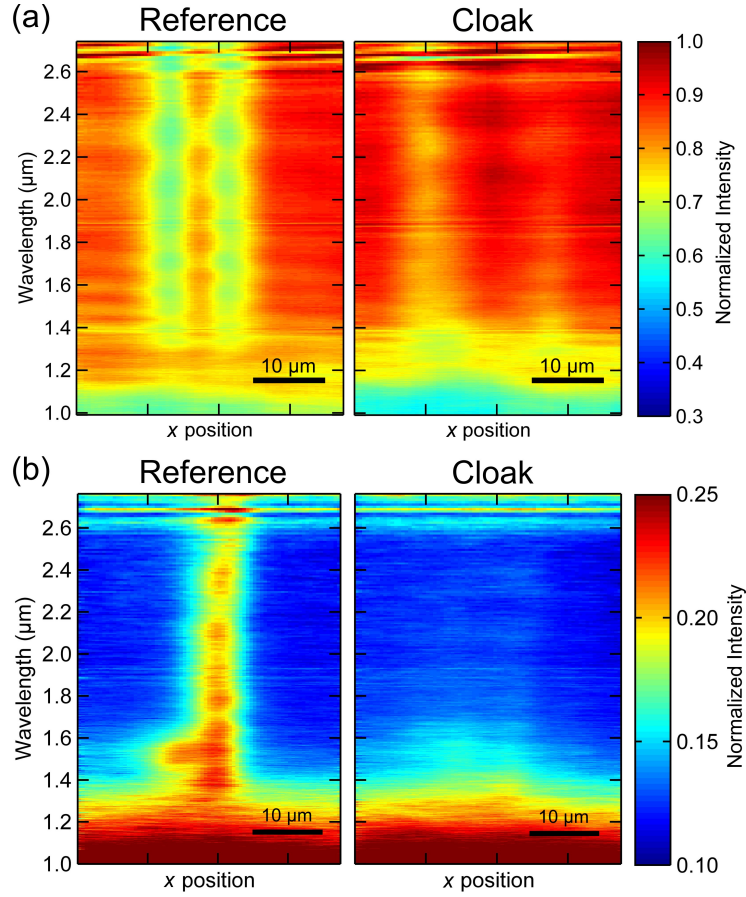


**Figure 5.7.:** Measurement results for the carpet cloak at infrared wavelengths. **(a)** Bright-field mode. On the left-hand side, the data for the reference structure is shown. The typical double-minimum “fingerprint” of the bump is visible above  $1.4\ \mu\text{m}$ . Here, the woodpile is transparent and can act as an effective medium. Below this wavelength, the stop band is entered and reflectance peaks. Since very little light reaches the bump in the first place, its signature vanishes. Intensity drops further when the wavelength is decreased, which is due to diffraction orders that are not collected by the finite numerical aperture of the objective. On the right-hand side, the result for the cloak is shown. The intensity approaches a homogeneous distribution – the result one would expect from a flat mirror. Cloaking is observed down to  $1.4\ \mu\text{m}$ . **(b)** Dark-field mode. Here, the reference bump lights up due to scattered light from the sides. Intensity increases when wavelengths drop below  $1.4\ \mu\text{m}$  due to increased diffraction and scattering. For the cloak, the effect of the bump is drastically suppressed and the measurement shows the characteristics of a flat mirror [106].

the complete interval from  $1.4\ \mu\text{m}$  and above, a drastic reduction in the bump's double minimum signature is visible. This approaches the expected homogeneous intensity distribution of a flat mirror. Slight distortions remain, whose possible origins we will discuss later. The behavior for wavelengths of  $1.4\ \mu\text{m}$  and below is similar to the reference, with the exception that the increase in reflected intensity in the stop band is not there. This might seem like a contradiction to the spectral data in Fig. 5.5, but we must remember that the transmittance and reflectance spectra were taken far away from the bump, where the cloak's woodpile is periodic and exhibits a stop band. Right in the vicinity of the bump, there simply is no clear stop band, since there is a gradual change of the filling fraction.

Fig. 5.7(b) shows the results for the dark-field mode. Here, we see an inverse behavior compared to the bright-field mode. At  $1.4\ \mu\text{m}$  and above, the bump lights up as a bright stripe. For wavelengths below  $1.4\ \mu\text{m}$ , the intensity gradually increases. This is expected, since we are in a measurement mode where we only collect scattered or diffracted parts of the illumination light. For even smaller wavelengths, the complete woodpile lights up (compare optical micrograph in Fig. 5.3(b)). The effect of the cloak in dark-field mode is even more impressive. The bright stripe almost completely disappears, giving rise to the expected reflection pattern of a flat mirror.

Overall, the performance of the cloak is very good. In fact, it is better than we estimated and demonstrates that the effective medium limit of the woodpile photonic crystal can in fact be set rather aggressively. Until the edge of the stop band, the woodpile apparently performs excellent. For a wavelength interval from  $1.5\ \mu\text{m}$  up to the end of the measurable wavelengths around  $2.7\ \mu\text{m}$  (spanning almost a full octave), we see good cloaking.

Apparently, the metamaterial that we used for the construction of the carpet cloak is quite forgiving in terms of spectral performance and losses. We wanted to check further how important the correct refractive-index distribution is for the cloaking effect. Therefore, we created samples which were flawed on purpose. For the first sample, we eliminated the low-index areas from the quasiconformal mapping (compare for example Fig. 5.4(b)). We simply set all values of the map that were below the reference refractive index  $n_{\text{ref}}$  equal to that value. The result of this experiment is shown in Fig. 5.8(a). The reference shows the expected double minimum. Note that depending on the sample quality, the stop band can be more or less pronounced. In this case, it is barely recognizable. However, the small cavity that forms the Fabry-Pérot resonances seems to be of good quality. For the cloak without the low-index parts, some cloaking behavior is observed. There is an increase in intensity in the middle, yet cloaking is definitely worse than in the optimal cloak case. The second test sample exhibited the opposite modifications. We replaced all values above the reference refractive index with the index itself, thereby removing the large high-index area in the vicinity of the bump. The results are shown in Fig. 5.8(b). Here, the reference again barely shows a stop band, yet the Fabry-Pérot oscillations are very pronounced. On a side note, we fitted these oscillations in one measurement. The extracted values for the

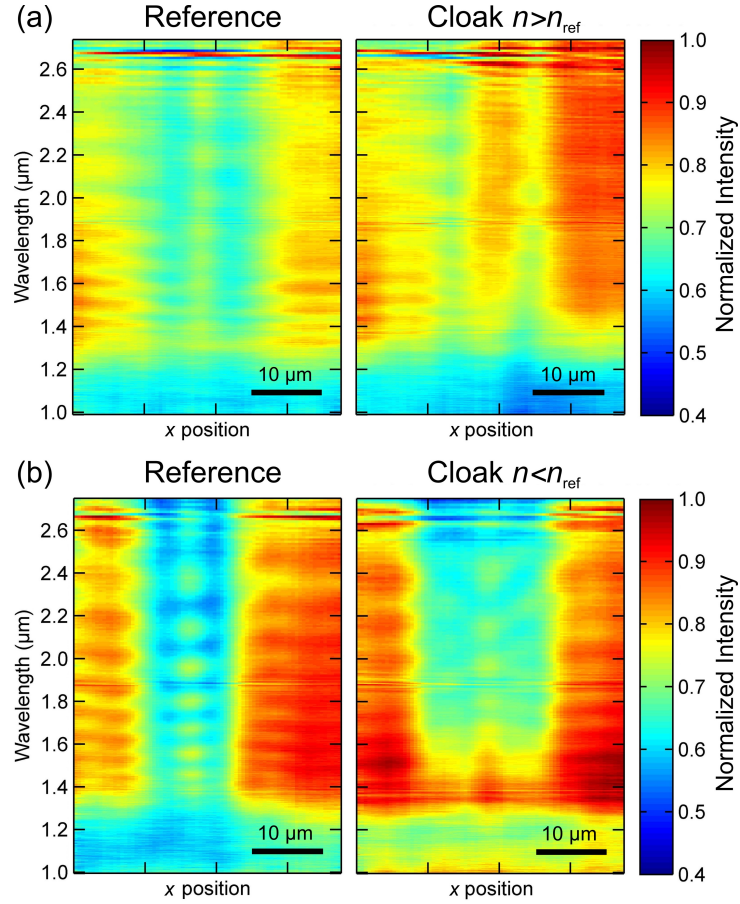


**Figure 5.8.:** Bright-field test measurements of cloaking structures with modified quasiconformal mapping. **(a)** Test cloak with no low-index areas at the side of the bump, all values below the reference refractive index are set equal to that index. The remaining high-index area of the index distribution leads to some cloaking. **(b)** Test cloak with no high-index area and only values below or equal to the reference refractive index. Cloaking is obviously bad, in fact the double minimum even shows an increased width for the cloak [106].

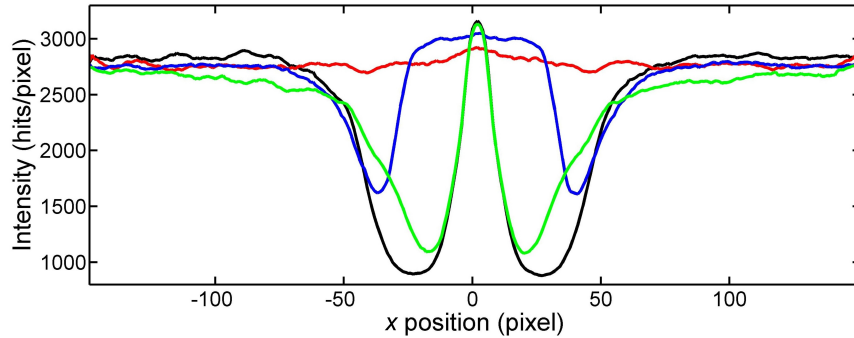


**Figure 5.9.:** Ray-tracing calculations of different modified cloaks. We show similar cross sections as in Fig. 5.8, yet without spectral information. The double-minimum signature of the uncloaked bump (black) is compensated almost perfectly by the optimal cloak with the complete quasiconformal map (red). The two modified versions, one *without* the low-index areas of the map (blue) and one *only with* the low-index areas (green), fail to cloak the bump. The results are in very good agreement with the measurement data (see Fig. 5.8).

thickness of the cloak and the reference refractive index that we got from this measurement were in good agreement with the expectations. On the right-hand side of Fig. 5.8(b), the cloak barely shows any cloaking. In fact, the double-minimum even seems to have increased in width. Since there is almost no change in filling fraction in the vicinity of the bump (the low-index areas are relatively small), the cloak can again exhibit a stop band around  $1.4\ \mu\text{m}$ .

For comparison with theory, we performed ray-tracing calculations using the same code as in Section 4.3.3. We calculated the cloak's performance for the case of the complete quasiconformal map and for both cases of the modified map. Fig. 5.9 depicts the results. We show cross sections through the bump in  $x$ -direction, very similar to the measurement but of course without the spectral information. The black curve is the intensity distribution of the uncloaked bump, the familiar double minimum. The red curve shows the optimal cloak with the complete quasiconformal map. The cloaking effect is almost perfect and the intensity distribution is nearly flat. For the modified distribution without the low-index areas, the blue curve shows that there is some reconstruction of the intensity around the middle of the bump, which is in agreement with the measurement shown in Fig. 5.8(a). However, this cloak fails to compensate the double minimum at the sides. Finally, the green curve depicts the result for the second modified cloak, where only the low-index areas are present. It is obvious that the cloak fails to compensate anything around the center of the cloak, in fact the curve coincides with the uncloaked case. Only at the sides, where the low-index areas are situated, some improvement is visible. However, the intensity at both sides increases more slowly, giving rise to a wider double minimum signature. This result is again in good agreement with the measurement in Fig. 5.8(b).

The data show that the cloak only performs good when the complete quasiconformal map is implemented. However, it is also clear from these results that the large high-index areas near the bump are much more important for the cloaking effect than the relatively small low-index areas at the sides, as one would have expected regarding the difference in size between these areas.

Finally, let us turn to possible reasons for the remaining distortions of the cloak in Fig. 5.7. In an experiment, one seldomly expects a perfect result, and pinpointing the exact reason for an imperfect result is often difficult. In our case, we want to discuss some possible issues:

- Theoretical considerations
  - In the theoretical derivation of the carpet cloak index distribution, some approximations have already been made. For example, the remaining finite anisotropy of the quasiconformal map was completely neglected. This alone already introduces shifts into the reflected light, as was discussed in Section 2.3.
  - The carpet cloak was originally conceived for a two-dimensional scenario. The extrusion into three dimensions leads to the fact that rays outside the design plane encounter a “wrong” refractive index profile.
  - The actual numerical calculation of the quasiconformal map is not perfect. Although one expects smooth iso-index lines in the distribution, they show small wiggles in our calculated map.
  - We calculated the woodpile’s isofrequency surface in wave vector space to be nearly spherical. There certainly remains some anisotropy, which is neglected and could disturb the isotropic implementation of the index distribution.
- Experimental considerations
  - In the fabrication of structures *via* DLW, the stability of the laser source that is used can be an issue. If there are drifts or deviations from the nominal laser power during the write process, the result is an incorrect mapping of the index distribution onto the filling fraction of the woodpile.
  - We actually perform a mapping twice. First we map the refractive-index distribution onto the filling fraction of the woodpile. This is followed by the mapping of the filling fraction onto the excitation laser power. The second mapping can also introduce imperfections into the system.
  - For this cloak, we used a technique where the thickness of the rods is controlled by choosing the number of voxels each rod is composed of. This number is obviously an integer, so that the filling fraction is actually mapped in a discrete step-like fashion and not completely gradual.

- Finally, in order to fabricate a reflecting mirror with the bump in it, we have to create a polymer layer on which the gold can be deposited. If there were no polymer carpet, the gold would simply cover the woodpile and even enter the structure to some extent. For us to create a smooth mirror, the polymer carpet is mandatory, but unfortunately it has a finite thickness on the order of several hundred nanometer. Therefore, the reflecting mirror is not exactly where it is supposed to be, but it rather has a buffer layer of polymer between itself and its designated destination.

### 5.3. Cloaking at Visible Wavelengths

After the successful demonstration of broadband three-dimensional polarization-independent optical cloaking at infrared wavelengths, the question arose whether the spectral operating regime of the cloak could be extended into wavelengths that are visible to the human eye. After all, the cloaking effect presented in Section 5.2 could not be seen with the bare eye, it rather had to be visualized from measurement data. Additionally, the measurement process itself at such uncommon wavelengths is painstaking due to the lack of suitable optical components. Theoretically, the task should be very easy. Since Maxwell's equations are scalable, we simply would have to shrink the cloaking structure by a factor of 3.7 to cover the complete spectrum of the human eye starting at a wavelength of 380 nm.

Of course, it is not that simple. Since the DLW-lithography process already operates at the diffraction limit, it was not until STED-DLW became available (see Section 3.3.2) that we could start decreasing the woodpile rod distance and therefore pushing the lower wavelength limit of the effective medium into the visible regime. We finally managed to shrink the woodpile to a rod distance of  $a = 350$  nm, miniaturizing the structure by a factor of 2.3. This should scale down the operation wavelength from the lower limit of about 1.5  $\mu\text{m}$  in the infrared case down to

$$\frac{1.5 \mu\text{m}}{2.3} = 650 \text{ nm}, \quad (5.1)$$

which is visible red light. The samples of the visible cloak shown in this part of the thesis were fabricated by Joachim Fischer in our group.

An electron micrograph of the new miniaturized carpet cloak is shown in Fig. 5.10(a). To enhance the visibility of details, we have overlaid two scanning electron micrographs with different brightness to produce a high dynamic range image. Similarly to the infrared case, we place a reference structure right next to the cloak. For inspection of the interior, we again have to destroy some structures in the FIB process. In Fig. 5.10(b), such a cut through nominally identical structures is depicted. Again, the good quality and clear

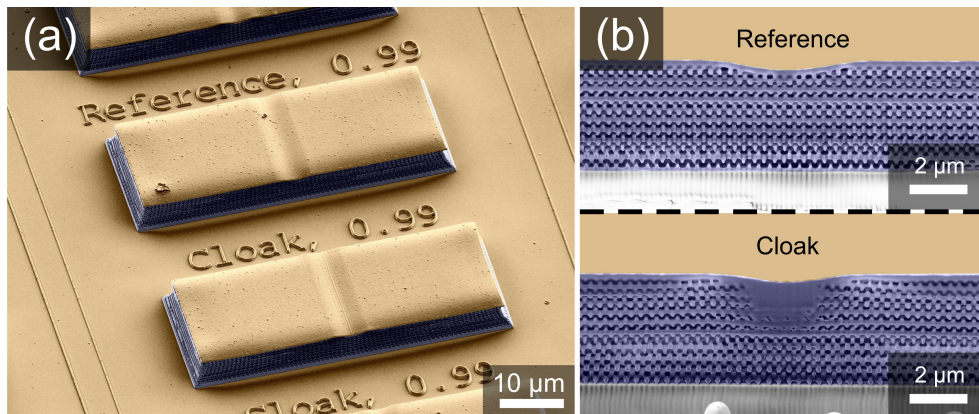


**Figure 5.10.:** (a) Electron micrograph of the miniaturized version of the carpet cloak. Gold parts are colored in yellow, polymer parts in blue. The rod distance is 350 nm, which brings the lower end of the working range into the visible regime at around 650 nm. Again, a reference structure (top) is situated right next to the cloak (bottom). (b) Electron micrographs of a nominally identical sample. Here, the structures have been cut open in the middle along the  $x$ -direction *via* FIB milling [119].

periodicity of the reference woodpile is visible as well as the gradual polymer filling fraction change inside the cloak.

For this structure, we choose different overall dimensions and also a slightly different bump compared to the infrared cloak. The external dimensions of the new cloak are 50  $\mu\text{m}$  in length ( $x$ -direction), 5  $\mu\text{m}$  in height ( $y$ -direction), and 20  $\mu\text{m}$  in width ( $z$ -direction). The height of the cloak corresponds to 40 subsequent layers of polymer rods. The bump itself follows the same  $\cos^2$ -shape as in the infrared case, yet its full width is  $w = 6 \mu\text{m}$  and its height is  $h = 0.5 \mu\text{m}$ . After the lithography process, a 100 nm thick gold film is sputtered onto the polymer carpet. The fabrication (apart from the STED-DLW approach and a different photoresist system) is similar to the one that was used for the infrared cloak, with one important difference: For this cloak, we gradually change the excitation laser intensity to control the thickness of the rods, thereby gradually changing the filling fraction and effective refractive index. This was a major advancement in the actual mapping of the theoretically calculated quasiconformal map onto the physical system.

Fig. 5.11 shows the carpet cloak as it is seen through a commercial standard microscope (Leica DMLM, N Plan 20 $\times$ , NA=0.4) under different illumination conditions and at different stages of the fabrication. In all of these images, an incandescent lamp is used for illumination. The images are taken with a common digital camera attached to the microscope. Fig. 5.11(a) shows a typical series of samples written with different parameters such as overall laser power or mapping of the target filling fraction to the laser power. The image was made right after the lithography process in reflective mode of the microscope. The images (a)-(c) are taken from the air side (note the letters right next to the structure).

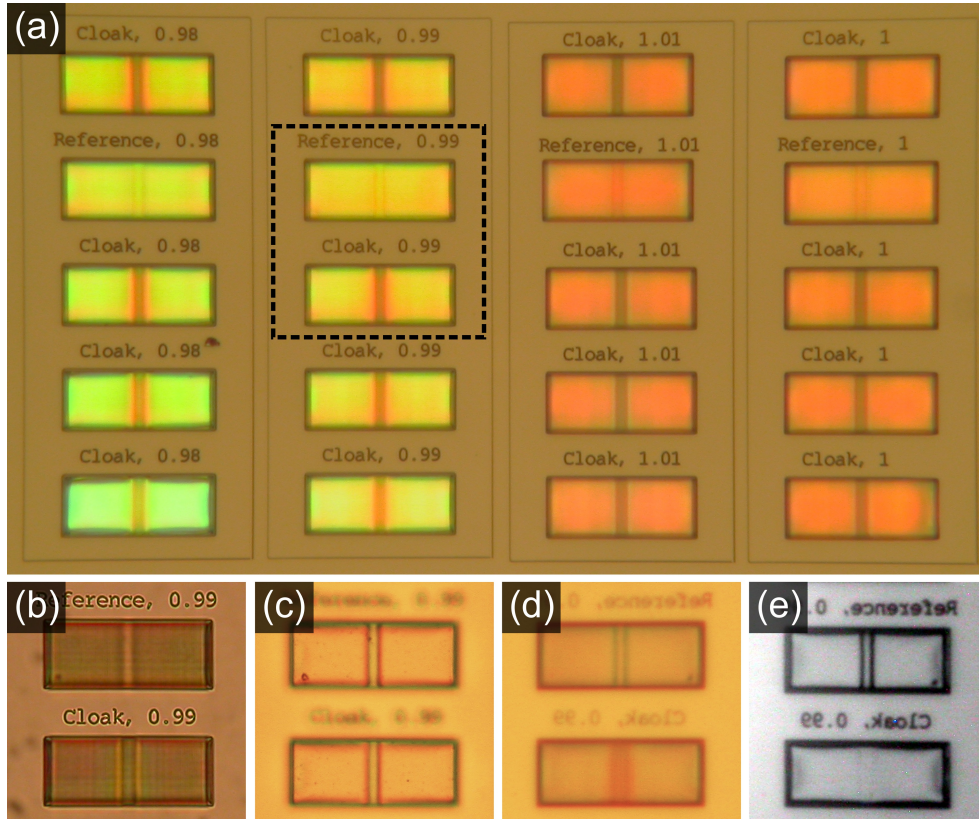


**Figure 5.11.:** Optical micrographs taken with a standard microscope and a common digital camera. Illumination is done with unpolarized white light. **(a)** Reflection mode of the microscope. The image shows a series of structures with different write parameters of the lithography process directly after fabrication. The black square marks the structures that were chosen for extensive studies throughout the rest of this work. These structures are also shown in (b)-(e). **(b)** Same as (a), but for transmission mode of the microscope. **(c)** Same as (a), but after the gold film has been sputtered onto the carpet. Both reference and bump show a double minimum, since we look from “the wrong side” (namely the air side) onto the dent (backside of the bump). **(d)** and **(e)** The sample has been flipped under the microscope. Now we look through the glass substrate and the woodpile/cloak onto the carpet and the bump (“correct” side) in reflection mode. In (d), the double minimum is visible for the reference, but with low contrast. The cloak is not working in white light illumination. In (e), an additional 760 nm long-pass filter has been introduced into the illumination path. Now, the contrast for the reference is greatly enhanced since the woodpile is transparent. For the cloak, the signature of the bump is almost completely gone – the mirror appears flat.

Note the homogeneous color of the reference structure and, in contrast to that, the change in color around the bump in the cloak. This change in color is a clear indicator for a change in the filling fraction. The local polymer content dictates the effective refractive index, which in turn dictates the position of the stop band, and thus the color. The marked black square is the part of the image that is shown in Fig. 5.11(b)-(e). These two structures are actually studied throughout the rest of this work. The image in Fig. 5.11(b) is taken under the same conditions as in (a), but for transmission mode of the microscope. Note that in contrast to the infrared cloak (see Fig. 5.3(a)), single rods can not be resolved anymore. Fig. 5.11(c) depicts the structures after the sputtering process. A 100 nm thick gold film forms a reflecting mirror. Figs. 5.11(d) and (e) depict the structure from the glass side (which in fact is the correct side to look at the sample). We have simply flipped the complete sample under the microscope (note the flipping of the letters). Aside from the direction of the view, Fig. 5.11(d) depicts the same as (c). For the reference, the double minimum is still visible, although weak. The cloak obviously does not hide the bump, since a lot of the components of the white light illumination are in fact below the working wavelength of the cloak. To eliminate these components, we have introduced a long-pass optical filter (Schott RG760), which suppresses all spectral components below 760 nm, into the illumination path. The corresponding image is shown in Fig. 5.11(e). The double minimum is clearly visible with a high contrast, since the woodpile is transparent at these wavelengths. For the cloak, the bump's fingerprint has almost completely disappeared, giving rise to the impression that the mirror is actually flat.

After the first inspection of the cloak under a standard microscope, we use an optical setup to measure the cloak under more controlled conditions in terms of the light source (see Fig. 5.12). Here, we illuminate the sample with a laser source (Inspire HF 100, Spectra Physics), which can be tuned from 345 nm to 2.5  $\mu\text{m}$  wavelength. Due to the monochromaticity (bandwidth of roughly 4 nm) and its tunability, this light source offers the possibility to measure the spectral characteristics very conveniently. The light is sent through a rotating diffuser (Thorlabs DG20-120), a beamsplitter and onto the sample using a microscope objective (ZEISS, LD Achromplan, 20 $\times$ , NA = 0.4). As we have shown at the end of Section 4.3.3, larger numerical apertures approaching unity would lead to a less sensitive test of the cloak's performance. The same objective that is used for the illumination collects the reflected light from the sample and images the sample plane onto the plane of the bare CCD-chip of a color camera (TK-C1381, JVC) *via* the beamsplitter.

In contrast to the incandescent illumination lamp in the case of the infrared cloak or the imaging of the visible cloak with the commercial microscope, we deal with highly polarized coherent light here. The images that are shown throughout the rest of this chapter are taken either with linear or circular polarization. We carefully probed for any deviations of the measured images depending on the actual polarization state of the light field. We could measure no difference whatsoever between the results for the two orthogonal linear polarizations or the circular polarization. For all intents and purposes of this work, the light can be regarded as unpolarized.

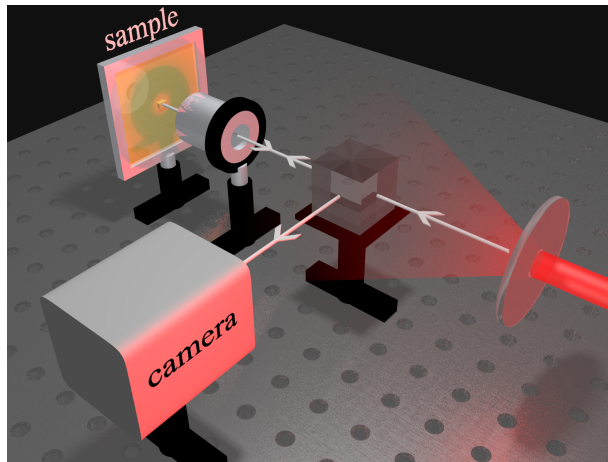


**Figure 5.12.:** Illustration of the optical setup that is used for the measurement of the carpet cloak at visible wavelengths. A laser is sent through a rotating diffuser. The resulting scattered light illuminates the sample through a beamsplitter and an objective. The sample plane is then imaged onto the image plane, which lies on the chip of a color camera. The camera simply takes pictures or a video, respectively.

The second characteristic of the illumination light, its coherence, poses a bigger problem. In a situation where the sample is illuminated directly by the laser without the diffuser in between, strong interference effects, such as diffraction at sharp edges, are expected. This largely obscures the measured image. Fig. 5.13(a) depicts this case for an illumination wavelength of 700 nm. Note the strong ripples and distortions at the edges of the structures or the thin lines on the substrate surface. This is clearly not suited for the measurement. Therefore, we introduce a diffuser into the path of the beam. Fig. 5.13(b) shows the image that results from this configuration. At first glance, it seems as if the situation has worsened. A heavy speckle pattern due to the rough surface of the diffuser obscures the view on the sample. Furthermore, the interference effects due to the coherence of the light did not vanish, although the interference patterns have changed. This dependence of the interference pattern on the speckles holds the key to the solution. If the diffuser is moved even a small bit, the speckle pattern and, along with it, the interference pattern changes. Now, we simply have to rotate the diffuser very rapidly, so that a large number of interference patterns are recorded in the camera during the exposure time of one frame. The camera will then see an image in which the intensity distortions are averaged out. The result is an image that is comparable to one that would have been obtained using a non-coherent light source. This sort of “destroying” the undesired interference effects of a laser source is referred to as “thermal light” in the literature [157, 158]. Importantly, the light is of course still highly coherent, which will become apparent in Section 5.4.

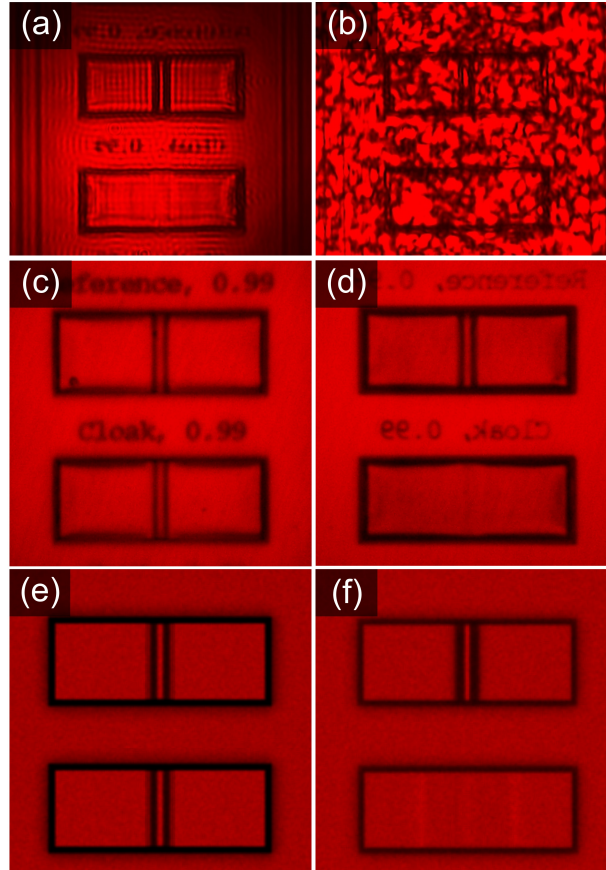


**Figure 5.13.:** Optical micrographs of the cloak and the reference under circular polarized illumination light at 700 nm. **(a)** The sample is illuminated directly by the laser without the diffuser in the beam path. Due to the coherence, the image is obscured by interference effects, for example diffraction at sharp edges. **(b)** The diffuser is introduced into the beam path. Now, a speckle pattern obscures the view completely. **(c)** When the diffuser is rotated rapidly, the camera averages out the speckle and interference patterns during the exposure time of one frame. The image clears up. In this image, we depict the “wrong” air side of the sample as a control experiment. From this side, both reference and cloak should look the same. **(d)** Here, the sample was flipped around by  $180^\circ$ . From the “correct” glass side, the reference still shows the two pronounced dark stripes. For the cloak, these stripes, and therefore the bump, essentially disappear. **(e)** and **(f)** are ray-tracing calculations corresponding to (c) and (d), respectively [114, 119].

The image that is measured with a rapidly rotating diffuser is shown in Fig. 5.13(c). Here, we get an unobscured view of both the reference and the cloak. Note the readability of the letters next to the structures, therefore, we again look at the sample “from the wrong side”, *i.e.*, from air directly on the metal carpet and the dent. This is a useful test measurement to make sure that both reference and cloak exhibit the same bump shape and an identical bump fingerprint. In Fig. 5.13(d), we again flip the sample around and observe the structures through the glass substrate and the woodpile. As already seen in the case of the commercial optical microscope including the long-pass filter (compare Fig. 5.11(e)), the cloak hides the presence of the bump making it, and any object hidden underneath, effectively invisible. Only very small distortions remain.

Finally, we can again turn to ray tracing to compare these results with theory. Figs. 5.13(e) and (f) depict such calculations. They correspond to the cases where the sample is viewed from the air side (Fig. 5.13(c)) and from the glass side (Fig. 5.13(d)), respectively. The agreement for the air side is excellent. The most prominent deviations of the theoretical calculations (panel (f)) from its experimental counterpart (panel (d)) are two brighter stripes left and right of the bump in the case of the ray-traced cloak. These stripes stem from the fact that the cloak region is surrounded by a homogeneous embedding woodpile. At the extremely small but finite refractive-index jump at this interface (which is not present in the experiment), total internal reflections can occur which result in an increased intensity (see Section 4.3.3 for details). Apart from that, the agreement for the glass side is also excellent.

### 5.3.1. Parametric Studies of the Carpet Cloak at Visible Wavelengths

A property that should be addressed when studying cloaks is the robustness of the cloaking effect under the change of observation parameters. These can include the wavelength of the incident light, the angle under which the cloak is illuminated (especially since we deal with a three-dimensional cloak) and the dependence of the “sharpness” of the image, *i.e.*, the position of the focal plane during imaging with respect to the cloak. In this part of the work, we want to study these parameter dependencies.

The spectral dependence of the carpet cloak at visible wavelengths is even more interesting than in the infrared case, since we can actually see the structure. For the measurement, the wavelength of the monochromatic laser source can easily be selected. We tune the source to a spectral position and image the cloak there. In Fig. 5.14, we have depicted a selection of such measurements. For comparison with the color images of the cloak, we have plotted the normal-incidence transmittance and reflectance curves of the reference woodpile measured with a commercial spectrometer in Fig. 5.14(a) before the sample was sputtered with gold. Here, a pronounced stop band centered around 575 nm is clearly visible. Above 650 nm, the woodpile becomes transparent. This is in very good agreement

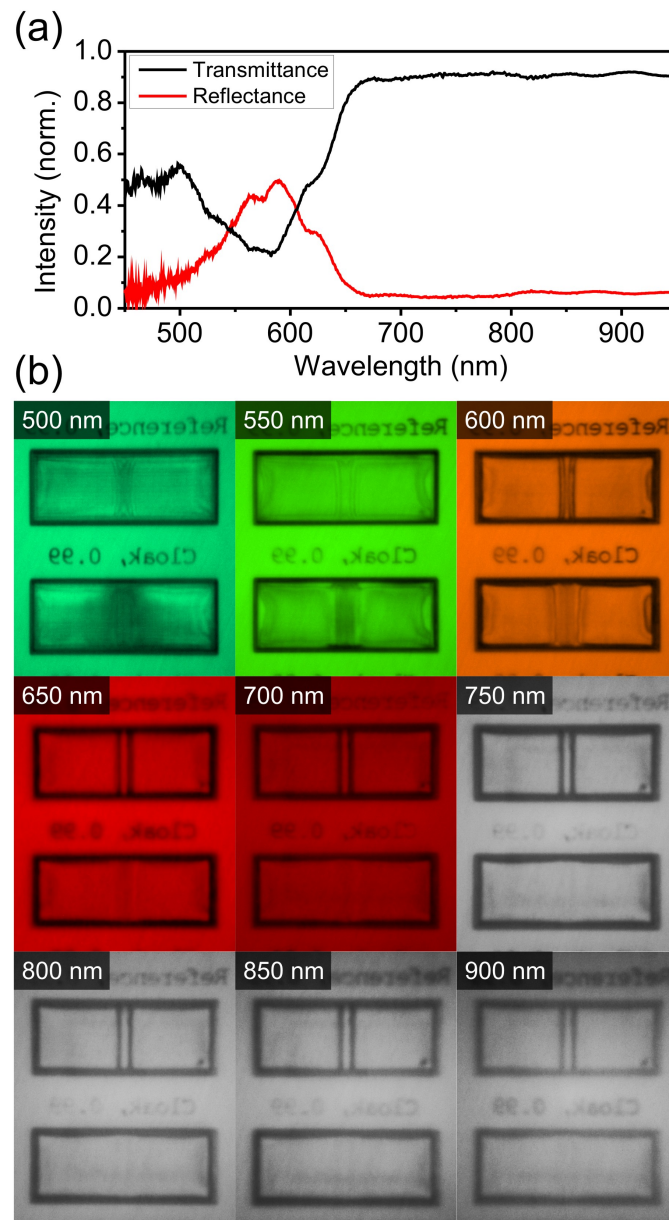


**Figure 5.14.:** (a) Measured normal-incidence transmittance and reflectance spectra of the polymer woodpile taken on the reference structure before gold sputtering. (b) As Fig. 5.13(d), but for different illumination wavelengths as indicated [114].

with our scaling estimate in Eq. (5.1) regarding the shrinking factor of 2.3 compared to the infrared cloak.

In Fig. 5.14(b), let us start in the green at 500 nm and 550 nm. Here, we are inside the stop band. This explains the fact that we can barely see the double-minimum fingerprint of the bump for the reference (top), since a large portion of the light never propagates through the woodpile to hit the bump, but it is rather reflected at the glass/woodpile interface. With this in mind, the inhomogeneous dark regions around the bump in the case of the cloak can also be explained. Here, the inhomogeneous filling fraction does not lead to a clear stop band. At 600 nm, we start to leave the stop band. Now, the fingerprint gets more pronounced in the case of the reference and it starts to fade out in the case of the cloak, although strong distortions are still present. After leaving the stop band at 650 nm, the fingerprint is now clearly visible for the reference. The cloaking effect sets in, as we have reached the effective medium limit of the woodpile photonic crystal. For all subsequent longer wavelengths, the cloaking performance does not change and remains excellent. This is expected, since we are only moving deeper into the effective medium approximation. Since we are measuring these images with a standard color camera with a silicon chip, the maximum wavelength that can be reached with acceptable data quality is 900 nm. However, we do expect the cloak to keep performing excellent until a wavelength of about 3  $\mu\text{m}$ . Here, absorption in the polymer occurs. This would give the cloak a spectral bandwidth of more than two octaves.

The second imaging parameter that we want to address is the angle dependence of the cloaking effect. Ideally, for a perfect three-dimensional cloak, there should be no dependence on the observation and illumination angle at all. There are three axes around which the sample can be tilted. The tilt around the  $z$ -axis (which is parallel to the bump) was already addressed in the ray tracing in Section 4.3.3 and in the measurement of the infrared cloak in Section 5.7. There, we referred to this measurement as the dark-field mode. The tilt around the  $x$ -axis (which is perpendicular to the bump and the optical axis) has not been addressed so far, but we will do so in the following. A tilt around the  $y$ -axis clearly does not make sense due to the cylindrical symmetry of the imaging setup (the  $y$ -axis points along the optical axis of the setup). The maximum tilt angle that we can achieve in the measurement is  $30^\circ$ . This is limited by geometric constraints (distance of the imaging objective from the sample and glass substrate size).

The measurement for the tilt around the  $z$ -axis (dark-field mode) is shown in Fig. 5.15. In Fig. 5.15(a), we depict the same measurement as in Fig. 5.13(d), but for a tilt of  $30^\circ$  of the sample. The reference (top) shows a clear bright stripe that marks the bump. For clarification, we have marked this stripe with a white dashed ellipse. At the bump, light is reflected off of the side slope, so that the reflection angle is such that the light can be collected by the microscope objective. For the cloak, this bright stripe disappears. Note that the bright stripes to the right of the bump in Fig. 5.15(a) are due to scattering at the side walls of both reference and cloak. These sides are now exposed to light due to the tilt. In Fig. 5.15(b), we show corresponding ray-tracing calculations. The theoretical

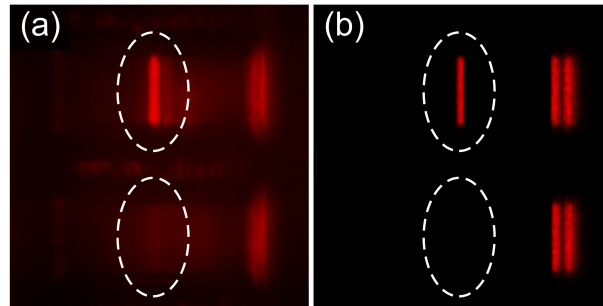


**Figure 5.15.:** (a) Same as Fig. 5.13(d), but for a tilt angle of  $30^\circ$  with respect to the optical axis (“dark-field mode”). The tilt axis is the  $z$ -axis parallel to the bump. White dashed ellipses mark the location of the bump in the case of the reference (top) and the cloak (bottom). (b) Ray-tracing calculations corresponding to (a) [114].

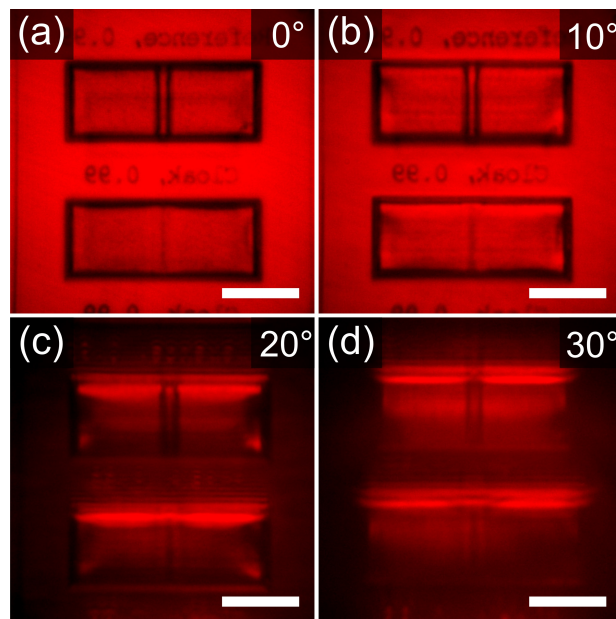


**Figure 5.16.:** True-color microscope images as in Fig. 5.13(d), but for a rotation of the sample around the  $x$ -axis. Measurements in steps of  $10^\circ$  to a maximum angle of  $30^\circ$  are depicted. The scale bars correspond to  $20\ \mu\text{m}$  [120].

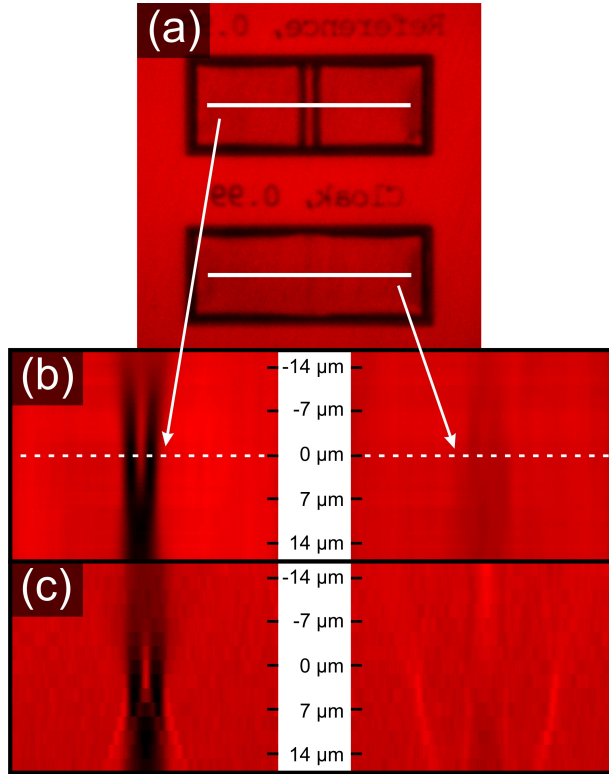


**Figure 5.17.:** (a) For clarification and comparison, we reproduce Fig. 5.13(d) here. The white lines indicate the cuts used in (b). (b) This panel exhibits the cuts in (a) versus focus position. The left image shows the reference structure, the right one the cloak. The distance from the optimal focus position is given in the middle of the panel. (c) Ray-tracing calculations corresponding to (b) [120].

calculations reproduce the experimental results to a very good extent. Note that the bright side stripes in the ray-tracing case are due to total internal reflections at the side walls. The cloak still performs excellent when tilted around the  $z$ -axis.

The second tilt axis of interest is the  $x$ -axis. We again tilt the sample by  $30^\circ$ . The result is shown in Fig. 5.16, where we depict tilt steps of  $10^\circ$ , respectively. For each angle, we stitched two separate images together: The first one is taken with the focus position at the center of the cloak, while the second one is focused on the reference. This is necessary due to the depth of sharpness when tilting the sample. Although slight distortions around the bump are visible in the cloak, the cloaking effect still persists. There is a clear reduction of the bump's fingerprint with respect to the reference structure.

Including the tilt around both aforementioned axes and using a microscope objective with  $NA = 0.4$ , the three-dimensional carpet cloak was exposed to and measured with a cone

of light that had a full opening angle of about  $110^\circ$ . We could determine that the angle dependence is only very weak.

The final parameter that we want to study is the dependence of the cloak's performance on the focal position of the imaging objective. Here, we vary the position of the sample along the optical axis of the system, which is the  $y$ -axis, by translating the sample with a computer-controlled microstepper. In other words, we "play with the knob" of the microscope. Since light is reflected from the cloak as if it would have come from a flat mirror, there should be absolutely no dependence of the cloaking effect on the "sharpness" of the image. A flat mirror always looks like a homogeneous plane, no matter where one focuses the camera. Fig. 5.17 shows the results of this measurement, where we reproduce the image at optimal focus position from Fig. 5.13(d) in panel (a). The optimal position of the focus is when the sample plane (more precisely the plane in which the carpet mirror lies) is imaged onto the plane of the camera chip. In this configuration, we get a sharp image of the carpet. All images in this work (except for this parametric study) have been taken with that focus position. (For the tilted cases, we aimed for the focus to be at the center base of the bump.) We set this position to be the zero value for this measurement. In the experimental data, the measured step size of the focus position is  $0.6\ \mu\text{m}$ . The deviation in micrometers in both directions from this position is given in the middle of panel (b) in Fig. 5.17. At different distances from the optimal focus position, we depict cross sections through the bump (marked in white in Fig. 5.17(a)). On the left side of Fig. 5.17(b), these cuts are shown for the reference, the results for the cloak are shown on the right. In the case of the reference, the bump's fingerprint changes shape depending on the focus position. For the cloak, there is no dependence on the "sharpness" of the image. We can qualitatively verify these results with ray-tracing calculations shown in Fig. 5.17(c). Note that the two outer bright stripes in the case of the ray-traced cloak are again the total internal reflections at the cloak's outer edges.

Finally, we can conclude that the three-dimensional carpet cloak is quite robust under variation of several imaging parameters, such as wavelength, angle and focus position. In all cases, we see good cloaking. Nevertheless, the hardest test of the cloak's abilities still remains to be carried out. It will be addressed in the following section.

## 5.4. Full-Wave Cloaking Including the Light Phase

So far, we have only shown cloaking for the light amplitude. This task can actually be achieved in various (sometimes quite trivial) ways, and TO only plays a role in few of them. For example, one can put on a scattering coat, place a camera which continuously records the scenery behind oneself, and project the image onto the coat from the front. An observer would have the impression to see through the person. The group of S. Tachi at Tokyo University has posted remarkable videos of that technique [159]. An interesting application of this kind of "invisibility" is augmented reality and man machine interfaces,

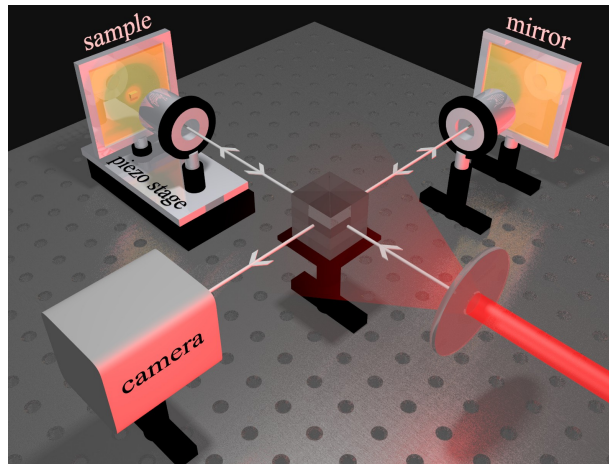


**Figure 5.18.:** Illustration of the interferometric setup. The images of both sample and reference mirror arm of this Michelson-like arrangement interfere at the camera and provide phase sensitivity [119].

for example in a transparent cockpit of a vehicle [160]. The same basic idea could be implemented by using flexible liquid crystal displays, which could be the constituents of a piece of clothing. Nevertheless, when it comes to real cloaking, these approaches would all fail. Since light is a wave phenomenon, we also have to consider the light phase. With projection and display approaches, the phase information is lost and only the amplitude can be reproduced. Such a cloaking device could immediately be detected by an interferometric experiment. In the mentioned devices, the light wave is not really guided or influenced in any way. It is simply detected and a similar pattern of light is emitted at a different position.

TO, on the other hand, delivers the possibility to really influence the trajectory of light. From the theoretical standpoint, one might think that the amplitude and phase of the light should always be cloaked simultaneously, since we usually start in an empty flat space where this connection is definitely given. However, depending on the transformation that is used, this is not always true. U. Leonhardt proposed cloaking devices which utilize a non-Euclidean geometry in their transformation [26, 32]. Here, light rays from an Euclidean branch of space (a hyperplane) can cross over into a non-Euclidean branch (a hypersphere). These rays can be guided around an object, similar to the cylindrical cloak. However, these rays experience a longer path than their counterparts outside of the cloak, they have a different time-of-flight. In terms of the phase of an electromagnetic wave, this means that the cloak only works at a single frequency (and multiples of it), where the additional path length is a multiple of the wavelength.

In the case of the carpet cloak, we should not encounter such problems, and we expect the cloak to work for the phase of the light, too. However, we have to verify this assumption experimentally. We also have to bear in mind that in the process of implementing the carpet

cloak, several approximations have been made (see end of Section 5.2). To measure the phase response of the cloak, we have to extend the setup in Fig. 5.12 such that it provides interferometric sensitivity. For this, we add another arm to form a Michelson interferometer (Fig. 5.18). We use the same objective and the exact same distances in this arm, so that it is nominally identical to the sample arm. Instead of the cloak, we place a bare substrate sputtered with gold at the position of the sample to serve as a reference mirror. The sample arm (including the sample itself and the objective) is mounted on a piezo stage. In this configuration, the image of the sample is overlaid with the image of the reference mirror. It is clear that in order for these images to interfere, we need coherent light. We have already discussed that the purpose of the diffuser is to create thermal light, *i.e.*, get rid of the coherence. Here, the camera averages over a multitude of interference patterns during the exposure time of one frame. However, for each single point in time, we have to consider different aspects of the coherence: There is lateral (spatial) coherence, which we want to get rid of, and there is temporal coherence. With temporal coherence we mean the interference along the optical axis. This interference holds the desired information about the phase of the reflected light. The averaging of the speckle pattern destroys the lateral coherence, however, it preserves the temporal coherence. Since both arms of the interferometer, after careful adjustments, are identical, the images of both arms exhibit the same speckle pattern at each point in time. The phase relation of these two images is therefore fixed, and it is not influenced by the averaging process.

We use the same laser as before, which in fact is a pulsed source (80 MHz repetition rate). This has not been of great significance up to now, but it is important for the interferometric measurement. Once the two arms have exactly the same length, we will see the interference image. Otherwise, the pulses from both arms miss each other. This adds to the demands in terms of adjustment, but it relieves us from potentially misleading and undesired interference effects from light that is reflected at optical components (for example, lenses).

Raw data of an interference image are shown in Fig. 5.19(a). If the reference mirror arm was blocked, these images would revert to Fig. 5.13(d). Note the interference fringes (dark/bright oscillations) in the area of the bump in the case of the reference (top) and the almost homogeneous intensity for the cloak (bottom). This is already an important clue to the phase response of the cloak, yet these images can be difficult to interpret. Let us denote the optical length difference between two corresponding rays in both arms as  $\Delta l$ . At  $\Delta l = 0$ , we have ideal constructive interference. If we move the piezo stage in the sample arm, we reposition both the sample itself and the imaging objective. At  $\Delta l = \lambda/2$ , we would have destructive interference, were  $\lambda$  is the wavelength of the incident light. Note that if the piezo moves by  $\delta$ , the change in the optical path of the interfering light is  $2\delta$ . This is due to the fact that we have a double-pass situation for the light, since it is reflected at the mirror. If we move the piezo by the same length  $\delta$  repeatedly, we expect the intensity to oscillate in a cosine-like fashion. For illustration, Fig. 5.19(b) shows the same as Fig. 5.19(a), but for a different piezo position.

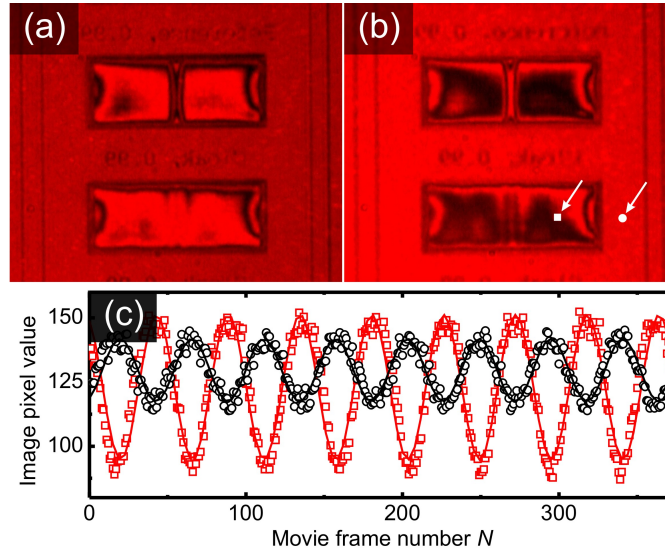


**Figure 5.19.:** Measured camera images at 700 nm wavelength illumination. **(a)** With the reference arm, the image provides phase contrast. Note the interference fringes at the bump of the reference (top) and the homogeneous intensity for the cloak (bottom). **(b)** Same as (a), but for a different piezo position. The data of the pixels marked with white circle and square are depicted in (c). **(c)** Raw data (circles and squares) and fits (lines) at two randomly picked pixel positions. The movie frame number corresponds to the piezo position [119].

For the measurement, we change the piezo position linearly and record a movie of the interference image at the same time. The movie typically has a length of 20 seconds and records about 8 to 9 full periods of the interference oscillation. Note that the piezo displacement can not be arbitrarily large, since we use pulsed light. At some point, the pulse envelope will start to play an increasing role until the interference pattern eventually vanishes. We measure around the  $\Delta l = 0$  position, where the pulse envelope is flat.

After recording the movie, we examine it pixel by pixel and frame by frame. Each individual pixel of the image has to oscillate in a cosine-like fashion. Therefore, we fit a function  $u$  of the form

$$u(a, \nu, N, \varphi, b) = a \cdot \cos(\nu N + \varphi) + b \quad (5.2)$$

to each pixel's data. Here,  $a$  is the amplitude,  $\nu$  is the frequency,  $N$  is the movie frame number,  $\varphi$  is the phase and  $b$  is the offset. The result of this fitting process is depicted in Fig. 5.19(c), where the data points are shown as circles and squares and the fits as lines. The data are taken from the (randomly picked) pixels indicated in Fig. 5.19(b).

We can simplify the fit procedure, since the frequency  $\nu$  has to be constant for all pixels at

a fixed wavelength. We fit the complete function in Eq. (5.2) to a small test set of pixels and derive the frequency. The deviations between these extracted frequencies turn out to be smaller than  $10^{-4}$ . Afterwards, the frequency is a fixed parameter for the rest of the image fitting. The phase is extracted from these fits for each pixel. Naturally, it can only be defined modulo  $2\pi$ , which leads to many disturbing discontinuous jumps in the resulting raw phase images. Therefore, we make the assumption that the phase change per spatial resolution is substantially smaller than  $2\pi$ , in other words, that the topology of the imaged surface is relatively flat. Under this assumption, we can shift the different  $2\pi$ -branches of the image by a computer algorithm such that continuous two-dimensional phase images result. This assumption breaks down when we consider the edges of the cloak or reference structure.

In Fig. 5.20, we depict the measured and extracted phase data for an illumination wavelength of 700 nm and corresponding ray-tracing calculations. For reasons of comparison, we again start with the air side of the sample (Fig. 5.20(a)). The phase images of both reference (top) and cloak (bottom) are identical within the measurement uncertainty. This again proves that the bumps in both structures are in fact identical, since the phase image can be interpreted as the geometrical topology that the light perceives. The local phase is false-color coded, and we depict a cross section as a white line to enhance the visibility of the topology and for later quantitative analysis. Note the gray areas around the reference and the cloak. Here, the extraction of the phase difference between the mirror and the glass substrate surface is not possible, since the structure exhibits a geometrical discontinuity at its edge. Therefore, the assumption of the phase reconstruction is not applicable. The height of the mirror above the glass substrate is arbitrarily chosen as  $7\pi$ . The phase measurement is very sensitive. Even the written letters next to the sample structures are resolved. In Fig. 5.20(b), the sample is again measured from the glass-substrate side. For the reference, the bump is clearly visible. In the case of the cloak, the phase response is nearly flat. Only very small perturbations remain. These experimental findings of the cloak's ability to reconstruct the amplitude as well as the phase of the light are confirmed by the results of the "phase tracing" calculation in Fig. 5.20(c) (see Section 4.3.3 for details).

For a quantitative analysis of the cloak's performance in terms of its ability to reconstruct the light phase, it is instructive to study cross sections through the bump. The cross sections considered here are marked as white lines in Fig. 5.20 and depicted in Fig. 5.21. Let us start with the theoretical ray-tracing results for the imaging from the glass-substrate side. The curve for the reference is depicted in green. The original design dimensions for the bump were  $6\ \mu\text{m}$  in width and  $500\ \text{nm}$  in height. Naturally, these parameters were used for the quasiconformal mapping and also for the ray-tracing calculations. The data depicted were calculated for a free-space wavelength of  $\lambda_0 = 700\ \text{nm}$ . With the reference refractive index of  $n_{\text{ref}} = 1.18$ , this translates into a wavelength in the medium of  $\lambda = \lambda_0/n_{\text{ref}} = 593\ \text{nm}$ . The ray-tracing data for the reference have a value of  $10.6\ \text{rad}$  at their maximum, which translates into  $0.84\ \lambda$ , considering the double-pass situation. As expected, the geometrical height of the reference bump results as  $500\ \text{nm}$ . For the cloak,

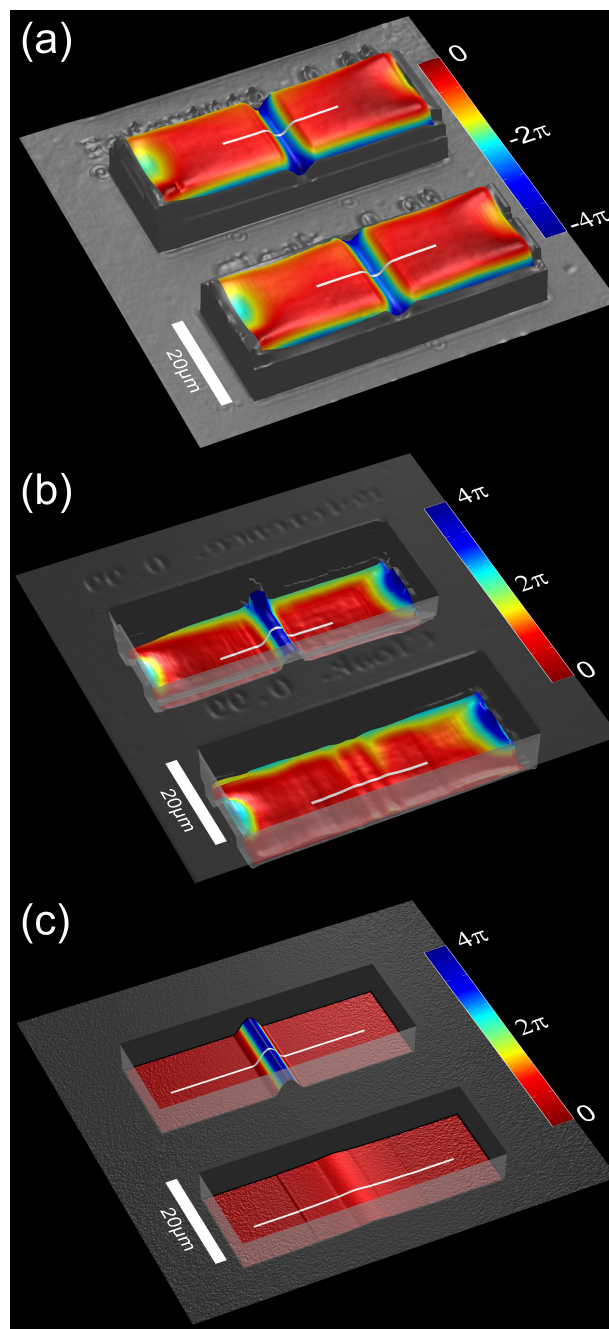


**Figure 5.20.:** Phase images, where the phase is coded in false color and given in units of rad. The gray colored areas originate from the fact that the phase reconstruction does not work at geometric discontinuities, such as the edges of the structure. Therefore, the phase difference to the colored areas cannot be determined. The white curves are cuts through the data that are separately shown in Fig. 5.21. **(a)** Measured phase image taken from the air side. The bumps are identical within the measurement uncertainty. **(b)** Measured phase image taken from the glass-substrate side. **(c)** Ray-tracing calculations corresponding to (b) [119].

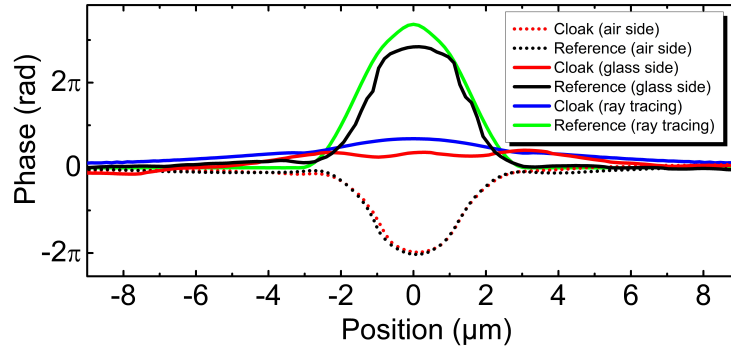


**Figure 5.21.:** Selected cuts through the phase-image data (see white curves in Fig. 5.20). The dashed black curve corresponds to the measurement of the reference taken from the air side, the almost coinciding dashed red curve corresponds to the cloak. From the glass-substrate side, the solid black and red curves correspond to the measurement on the reference and cloak, respectively. Corresponding ray-tracing calculations for the phase are shown for the reference (green) and the cloak (blue).

the ray-tracing results (blue curve in Fig. 5.21) show a strong suppression of the phase response of the bump. At its maximum, the remaining phase corresponds to 20% of the uncloaked bump’s response.

Let us now turn to the experimental data in Fig. 5.21. The solid black line shows the phase response of the reference bump. The maximum value here is 8.93 rad or  $0.71 \lambda$ . If we assume the theoretical reference refractive index that we aimed for and used for the ray tracing, the geometrical height of the bump results as 421 nm. If we consider the cloak (solid red curve), we find that the cloaking effect is actually better than the ray-tracing calculations suggested. The cloak suppresses the bump’s phase response down to 13% or lower with respect to the reference bump.

Finally, let us examine the experimental results for the air side. The data for the reference and the cloak are depicted as black and red dashed lines, respectively. Since these curves almost coincide, the bumps both in the reference and the cloak have essentially identical shape. When we evaluate the maximum amplitude of these bumps, we find that they have a height of 6.38 rad or  $1.02 \lambda_0$ , which corresponds to 360 nm. Obviously, this height differs from the height we extracted from the glass-substrate side. An explanation for this could be that the design filling fraction, and therefore the reference refractive index, was not implemented correctly in the experiment. Hitting the right laser power in the writing process is difficult, so that deviations from the design filling fraction are common. Our findings suggest that the filling fraction throughout the structure is higher than anticipated. When the measurement from the air side is taken as a reference value, the reference refractive index results as  $n_{\text{ref}} = 1.36$ . The findings also suggest that the bump itself is not as high as it was designed.

## 5. *Experimental Results*

---

Although not perfect, this three-dimensional carpet cloak demonstrates that it is fully capable of hiding an object from detection – even from an interferometric measurement. This impressively reveals the full potential of TO.

## 6. Summary

Transformation Optics (TO) is a field of optics that has only been researched for about five years. The approach of TO allows to “reverse-engineer” Fermat’s principle in a sense. Where Fermat’s principle predicts the trajectory of light in a given distribution of optical parameters by choosing an extremal path for the light, TO allows to design a desired path of light and calculate the necessary optical parameters that lead to that path. In the short period of time of its existence, TO has led to some remarkable theoretical proposals for new optical devices. However, the experimental realization for most of these devices still needs to be done. The goal of this thesis was to study one of these novel devices: a three-dimensional invisibility cloak. The task was to conceive, design, and numerically study a feasible cloak, before it should be fabricated using direct laser writing. Finally, it should be measured and optically characterized to provide the proof of principle that optical invisibility cloaks are in fact science, not science fiction.

In the first part of this thesis, we have presented the mathematical framework of the theory of TO (Section 2.1). After introducing the necessary tools, we have recapitulated how the geometry of space(-time) is connected to the propagation of electromagnetic waves. As an example, we have shown the complete transformation procedure of the cylindrical cloak, one of the most famous cloaking devices derived by TO. We have also numerically studied this cloak in order to assess its experimental feasibility (Appendix A.1). The result of these studies was that the implementation of an invisibility cloak (or in that respect, any transformation device) that requires values of the (anisotropic) permittivity that are below unity is not feasible at optical frequencies. This is due to the fact that the losses of metamaterials that provide such optical parameters are too high in that frequency regime. Furthermore, the cylindrical cloak in its ideal form requires an anisotropic magnetic response, which is also not feasible at optical frequencies and for this geometry. Although there is a way to circumvent the necessity of a magnetic response in some cases, it makes the device sensitive to the polarization state of the light. Therefore, the cylindrical cloak was ruled out as an experimental device.

The theoretical proposal of another type of cloak, the carpet cloak (Section 2.3), showed a way to realize a cloaking device without a magnetic response and with isotropic material parameters. With the fabrication capabilities of our group in the field of three-dimensional dielectric structures in mind, this was a promising path to pursue. Since our final goal was to create a three-dimensional cloak, we began with numerical studies of this carpet cloak, which was originally proposed for a two-dimensional geometry. In order to perform

any kind of numerical calculations, we first had to recalculate the cloak's optical parameters *via* a quasiconformal mapping procedure, that was implemented using the genetic algorithm (Section 4.1). In the numerical studies subsequent to the derivation of the optical parameters, we followed two different approaches. The first approach was to study the cloak in two dimensions using finite-element calculations with the commercial software package *Comsol Multiphysics* (Section 4.2). Here, we demonstrated that the carpet cloak's refractive-index distribution could be implemented using a purely dielectric metamaterial, resembling a cut through a three-dimensional woodpile photonic crystal. We studied the angle dependence of the cloak, its dependence on the wavelength of the incident light and the light's polarization (Section 4.2). The result was that the cloak's performance showed little to no dependence on the polarization or the incident angle of the light. Furthermore, we confirmed that we could use a dielectric photonic crystal in the long-wavelength limit as a metamaterial to implement the cloak's refractive-index distribution. Since these finite-element calculations were restricted to a relatively small calculation domain, it was out of reach for us to assess the performance of the cloak in the far field of a fully three-dimensional environment. Therefore, we followed the second approach in our numerical studies: geometrical ray tracing.

For the ray tracing (Section 4.3), we programmed two distinct dedicated codes using *Matlab*. Both codes were able to calculate the cloak in a three-dimensional virtual environment, where the cloak was described in the effective-medium approximation. Using the first code, we studied the cloak in terms of its overall three-dimensional performance. For this, we calculated photorealistic images of a cloak with macroscopic dimensions situated in a virtual museum room (Section 4.3.2). We could demonstrate that the cloak works remarkably good in three dimensions, even for large angles out of the original design plane. As a next step, we wrote another dedicated ray-tracing code that was capable of calculating a complete optical imaging setup, including light source, lenses and the sample with the cloak (Section 4.3.3). With this code, we were able to show how such a cloak would look like when fabricated on a glass substrate and placed under a microscope. These ray-tracing calculations served as a direct theoretical comparison to the subsequent experiments, and we could again study the angle dependence as well as the robustness of the cloaking effect in terms of depth of field or focus position, respectively. The results were very encouraging, so that we could proceed with the experimental realization of the carpet cloak.

Based on our experience with three-dimensional woodpile photonic crystals, we designed the carpet cloak using such a woodpile, but varying the local filling fraction and, thus, controlling the local refractive index. We have also performed band-structure calculations using the free software package *MIT Photonic-Bands* in order to assess the isotropy of the woodpile that we used. These calculations showed that the iso-frequency surface in wave vector space was nearly spherical, and the woodpile provided a suitable metamaterial to implement the cloak's index distribution, as long as it was used in the long-wavelength limit. The smallest stable woodpile with controlled filling fraction that we could fabricate using regular direct laser writing exhibited a rod distance of  $a = 800$  nm (Section 5.1).

---

For this, we roughly estimated a minimal operating wavelength around  $2\ \mu\text{m}$  in the infrared regime. We were surprised when the measurements showed that the cloak in fact outperformed these expectations and that the effective-medium limit could be set rather aggressively.

For the measurements of the infrared cloak, we built an optical setup that was able to evaluate the cloaking effect at these frequencies (Section 5.2.1). We imaged the magnified sample plane onto the image plane and scanned one end of a chalcogenide optical fiber across that plane. At every position, we measured the spectrum using a home-built Fourier-transform infrared spectrometer that was coupled to the other end of the fiber. With this setup, we were able to measure the performance of the cloak over a spectral range from  $1\ \mu\text{m}$  to  $2.7\ \mu\text{m}$ . Importantly, we performed a *three-dimensional* measurement, since we averaged over a large angle distribution in the cone of light that the microscope objective picked up. With this experiment, we were able to demonstrate the first realization of a three-dimensional polarization-independent invisibility device, ever. The measurements showed very good cloaking behavior for wavelengths that are larger than  $1.5\ \mu\text{m}$  (Section 5.2.2). Unfortunately, for the measurement of the infrared cloak, we were restricted to data from a cross section, since the pointwise measurement proved to be very time consuming.

However, this changed when we were able to miniaturize the carpet cloak by a factor of 2.3 using a stimulated-emission-depletion-inspired direct-laser-writing setup. For this cloak (Section 5.3), the rod distance was  $350\ \text{nm}$ , pushing the minimal operation wavelength into the visible at  $650\ \text{nm}$ . Here, we could simply image the complete structure using a microscope and record these images with a standard color camera. The results could be compared directly to the corresponding ray-tracing calculations carried out before. With this structure, we could demonstrate three-dimensional polarization-independent broadband invisibility cloaking for wavelengths of the human visible spectrum for the first time. We studied the angle dependence more closely and could confirm our previous findings: the cloak works for a large angle spread of about  $110^\circ$  (full opening angle of the measured cone). The measurement of even larger angles was restricted due to geometrical constraints of the sample. We also confirmed the insensitivity to the exact focal position, as the ray-tracing calculations had predicted. As a last important parameter, we studied the spectral dependence using a tunable laser source and imaging the cloak at several wavelengths. Beginning at around  $650\ \text{nm}$ , the cloak showed excellent performance up to wavelengths of  $900\ \text{nm}$ . This upper limit was again due to the setup, since the CCD-chip of the camera was not sensitive enough to deliver images of proper quality at longer wavelengths. However, we expect the cloak to work up until a wavelength of around  $3\ \mu\text{m}$ , where absorption of the polymer sets in. This would correspond to a bandwidth of more than two octaves.

Finally, we completed the proof of principle of a three-dimensional cloak at visible wavelengths by measuring not only the reconstruction of the light amplitude, but also the light phase (Section 5.4). In fact, this measurement put the highest demands on the performance

## 6. Summary

---

of the cloak. We were able to demonstrate that the cloak suppresses the phase distortion introduced by the mirror bump by roughly 90%, resulting in an almost flat phase profile. With these measurements, we could show that the cloak is capable of hiding objects even from interferometric detection, and that it is possible to create a cloak for the full electromagnetic wave at visible wavelengths.

Although the carpet cloak presented in this thesis was a “mere” proof of principle and will most likely not find its way into everyday life, the underlying principles of TO may yet prove to introduce some other practical devices in the future. Improved aberration-free lenses, devices for an increased efficiency in light harvesting and photovoltaics, shape-independent functional devices in integrated optical circuits, or protection from forces of nature like tsunamis or earthquakes by “cloaking” objects from the corresponding waves are just a few examples the author wants to mention. Since the field of TO is still very young, it has not yet risen to its full potential. Furthermore, even during the course of this thesis, major advances in fabrication techniques took place, which enabled us to create the cloak at visible wavelengths. It is not clear at what rate further advancements in lithography or other techniques will happen. But it is clear that as they do, more and more proposals derived from TO will become feasible. We may yet be surprised what type of novel devices will become available in the future, in the same sense as the creation of an invisibility cloak has amazed the public, the media and scientists alike.





# A. Appendix

## A.1. Finite-Element Calculations of the Cylindrical Cloak

As the main theme of this thesis revolves around cloaking devices, we want to present our work on cylindrical cloaking devices [21, 81, 82]. These types of cloaks were the first to be proposed, and the focus of several experimental groups lay on them. In the first months of this thesis, we numerically studied these devices in order to assess their experimental feasibility and applicable material systems for realizing them. We used the commercial finite-element software package *Comsol Multiphysics* to carry out these calculations.

Let us start by quickly recapitulating the optical parameters for a cylindrical cloak. In this type of cloak, a cylindrical region with  $r' < b$  is compressed into a concentric cylindrical shell with  $a < r < b$ , where  $r$  is the radius and  $a$  and  $b$  are the inner and outer radius of the cloaking shell, respectively. The center point is mapped onto the inner radius  $a$ , which “rips a hole” into space. Every object that is placed inside this inner core region is invisible, since it cannot interact with any electromagnetic field from the outside. A note on the side: The person hiding inside this cloak is by definition absolutely blind. Even a flashlight would not help to make him see the outside world - the same argument that states that no light can enter the core simultaneously implies that no light can exit it. As was demonstrated in Section 2.1.5, the optical parameters for the cylindrical cloak are

$$\varepsilon_r = \mu_r = \frac{r - a}{r} \quad (\text{A.1})$$

$$\varepsilon_\theta = \mu_\theta = \frac{r}{r - a} \quad (\text{A.2})$$

$$\varepsilon_z = \mu_z = \left( \frac{b}{b - a} \right)^2 \frac{r - a}{r}. \quad (\text{A.3})$$

If we examine for example the permittivity  $\varepsilon$ , we see that its radial component goes to the constant  $(b-a)/b$  for  $r \rightarrow b$ . Its azimuthal component is the inverse of the radial component at any point. For  $r \rightarrow b$ , the  $z$ -component also goes to that constant, namely  $b/(b-a)$ . It is clear from these values, that the cloak is impedance-matched to the surrounding

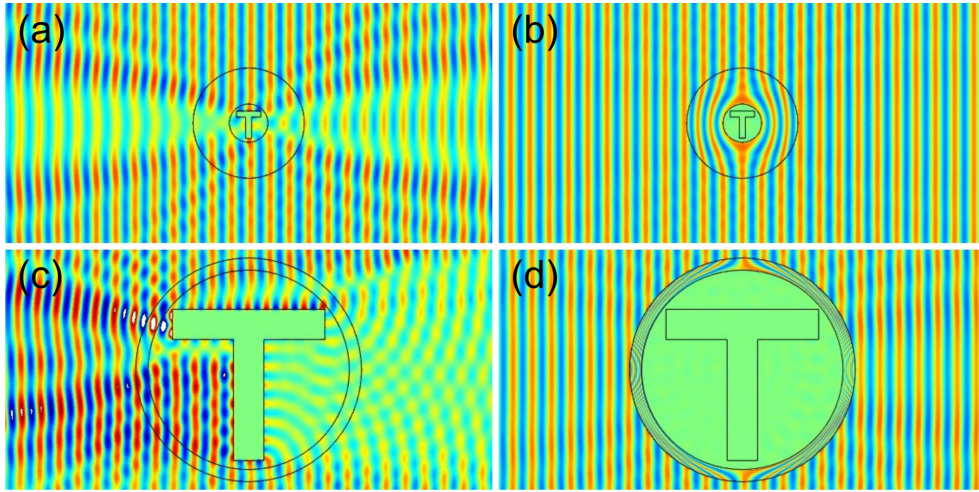


**Figure A.1.:** Finite-element calculations of a cylindrical cloak. A TM-polarized plane wave impinges from the left. The calculations show snapshots of the  $z$ -component of the magnetic field. **(a)** A T-shaped metallic scatterer without cloak is hit by the wave. **(b)** The cylindrical cloak with ideal parameters is put in place. No field can enter the inner core and the object is made invisible. **(c)** Same as (a), but with enlarged inner core and outer radius. The cloak is squeezed into the small shell. **(d)** The cloaking effect is not influenced by the choice of inner and outer radius.

vacuum (or air) at the outer edge. The impedance (for both TE and TM polarization) at  $r = b$  is

$$Z|_{r=b} = \sqrt{\frac{\mu_\theta}{\varepsilon_z}} = \sqrt{\frac{\mu_z}{\varepsilon_\theta}} = 1. \quad (\text{A.4})$$

It is interesting to note that the cloak does not show any singular values at the outer edge. By choosing an adequate size of the cloaking shell and therefore a suitable ratio  $a/b$ , the absolute values of the optical parameter components can be kept quite feasible. The story changes when the other limit,  $r \rightarrow a$ , is examined. Here, the radial and the  $z$ -component are zero, while the azimuthal component is infinite. Furthermore, the impedance is infinite or zero at  $r = a$ . This is an expression of the fact that the inner core of the cloak and the cloaking shell are electromagnetically decoupled, no field can penetrate the inner core. When a wave hits the cloaking shell along the horizontal middle axis, it slows down until it finally “jumps” over (or around) the inner core with superluminal phase velocity that tends to infinity. From the viewpoint of the wave, all points on the inner radius  $a$  are spatially equivalent, since they originate in one mathematical point of the untransformed space.

Figure A.1(a) shows numerical calculations for a T-shaped metallic scatterer without a cloak (the shell marked with black lines is simply air in this case). We choose a TM-polarized plane wave (magnetic field normal to the propagation plane) for this calculation,

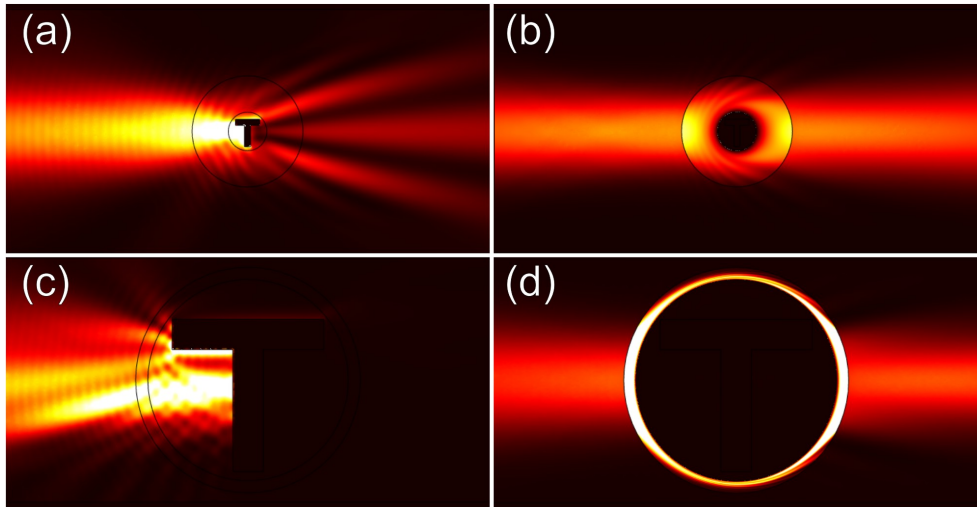


**Figure A.2.:** Same configuration as Fig. A.1, with the difference that the plane wave is replaced by a Gaussian beam. We plot the time-averaged total energy density.

yet the result for TE polarization is the same (not shown). The wave propagates from left to right, and the wavelength for all calculations is  $\lambda = 632.8$  nm. The inner radius of the cloak shell is  $a = \lambda$  and the outer radius is  $b = 2.9\lambda$ . Obviously, the scatterer casts a shadow and reflects the wave partially, which leads to standing waves. In Fig. A.1(b), the cylindrical cloak is surrounding the scatterer. Here, the optical parameters in Eqs. (A.1)-(A.3) are implemented. These parameters are referred to as “ideal” parameters, since they are directly derived from the transformation without any further approximation. This set of parameters automatically introduces polarization-independence, since  $\boldsymbol{\varepsilon} = \boldsymbol{\mu}$  holds everywhere. Note how the phase fronts “flow” around the inner core, very much like water around a stone in a river, and leave the cloak perfectly undisturbed. An interesting aspect of the cloak is, at least theoretically, its scalability. This means that the ratio  $a/b$  can be chosen arbitrarily without affecting the cloaking performance. However, for large values of  $a/b$ , the optical parameters become more and more unfeasible. Figs. A.1(c) and (d) shows such a scaled up version, the inner core area is enlarged and the cloak is squeezed into a small shell. Here, the inner radius of the cloak shell is  $a = 5.2\lambda$  and the outer radius is  $b = 5.8\lambda$ . Nevertheless, the cloak works perfectly. Even more impressive is the performance of the cloak when illuminated by a Gaussian beam of light instead of a plane wave (see Fig. A.2). Note how the Gaussian beam is totally reflected in the case of the large scatterer (Fig. A.2(c)), and how the light is guided around the inner core in the case with the cloak (Fig. A.2(d)). The beam is completely reconstructed after exiting the cloak.

Since we are interested in the feasibility of these designs, the ideal parameter set is obviously not a good choice: it is singular and requires a non-zero anisotropic magnetic response. Especially the necessary magnetic response turns out to be the greatest obstacle at optical

frequencies. As we have pointed out in Section 2.1, the propagation of the wave inside the transformation medium is governed by the product of the corresponding principal values  $\varepsilon_i \mu_j$ . Therefore, a different set of parameters (with the same product  $\varepsilon_i \mu_j = \varepsilon'_i \mu'_j$ ) can be chosen. Of course, it is convenient to choose  $\mu'_j = 1$  and  $\varepsilon'_i = \varepsilon_i \mu_j$ . This is referred to as the “reduced” parameters. This restricts the problem to a two-dimensional geometry with only one allowed polarization – a typical waveguide situation. If we choose TM polarization, the necessary parameter set boils down to

$$\varepsilon'_r = \left(\frac{b}{b-a}\right)^2 \left(\frac{r-a}{r}\right)^2 \quad (\text{A.5})$$

$$\varepsilon'_\theta = \left(\frac{b}{b-a}\right)^2 \quad (\text{A.6})$$

$$\mu'_z = 1. \quad (\text{A.7})$$

This choice of parameters comes with a price: Fresnel reflections at the outer interface of the cloak shell. If we examine the impedance at that point, it reads

$$Z' = \sqrt{\frac{\mu'_z}{\varepsilon'_\theta}} = 1 - \frac{a}{b}. \quad (\text{A.8})$$

Again, the choice of the ratio  $a/b$  determines the gravity of this drawback.

Up to now, we have not yet discussed the experimental realization of these parameters. We can use metamaterials (see Section 3.1) to achieve the necessary values, for example the values close to zero for the permittivity at the inner core of the cloak. Necessarily, we have to introduce a material with a negative permittivity (metal or resonant structure) as one component of the metamaterial together with a dielectric with positive permittivity in order to have a zero overall response. This has grave consequences. Metals at optical frequencies as well as resonant phenomena are always accompanied by losses. Nevertheless, we want to study the impact of these losses on the overall cloak performance.

Figure A.3(a) shows an implementation of the reduced parameter set in the cylindrical cloak. When comparing the result with the ideal parameter cloak (see Fig. A.1(b)), a perturbation of the field is noticeable. This is due to the impedance mismatch and the resulting Fresnel reflections at the outer edge of the cloak. Also note the non-zero field inside the inner core at the scatterer. This is due to the non-singular impedance at the inner radius  $a$  – fields can penetrate. Yet, the overall performance of the cloak with reduced parameters is still good. We have to find a metamaterial structure that provides the necessary reduced parameters yet. W. Cai *et al.* [161] proposed a so-called “wing structure”, since it looks like the paddle wheel of a paddle wheel steamer or a cylinder with wings on it (compare Fig. A.3(d)). It consists of alternating wings of metal and dielectric with gradually changing radius-dependent thickness. As a metal, we choose silver as described by Johnson and Christy [162] with a permittivity of  $\varepsilon_s = -17.1 + 0.24i$ ,

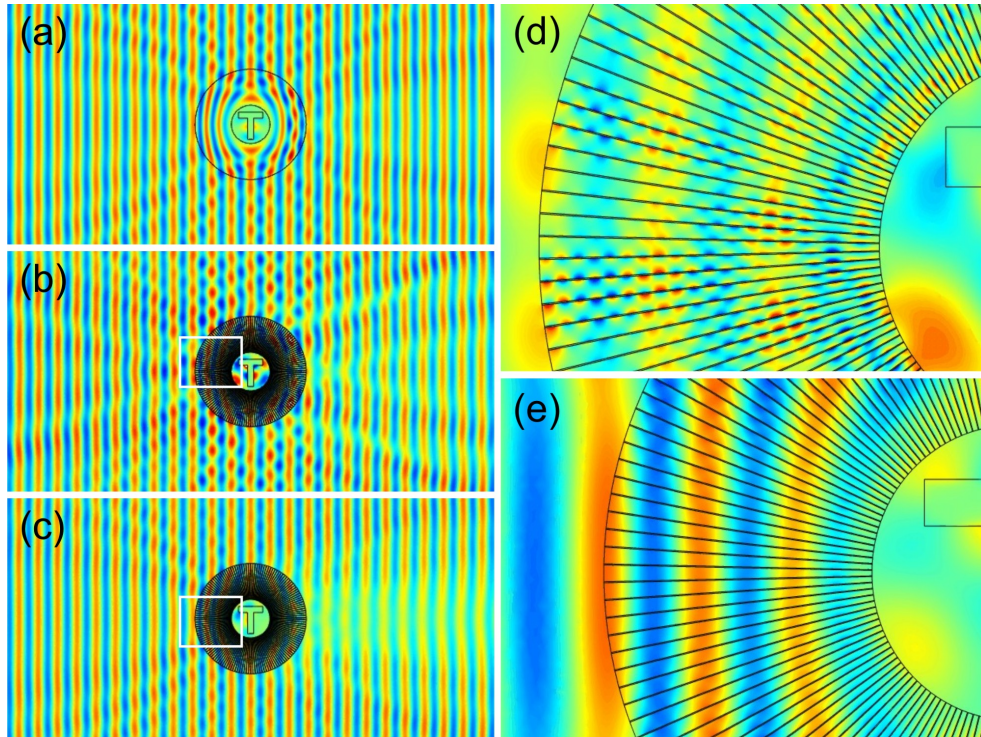


**Figure A.3.:** Numerical calculations similar to Fig. A.1. **(a)** The ideal parameters of the cloak (Fig. A.1(a)) have been replaced by the reduced parameters. Fresnel reflections at the outer boundary occur (compare Fig. A.1(b)). **(b)** Full-geometry implementation of the reduced parameters *via* a structure of alternating “wings” of silver and silicon dioxide. Losses of the metal are neglected. **(c)** Same as (b), but with losses. Scattering is reduced, but the cloak now casts an obvious shadow. **(d)** Zoom of the area marked with a white rectangle in (b). Note the field enhancements due to plasmonic oscillations, which lead to scattering (to avoid saturation, this panel is plotted on a different scale). **(e)** Zoom of the area marked with a white rectangle in (c). The plasmon oscillations are damped and the scattering is reduced.

and as a dielectric we use silicon dioxide with a permittivity of  $\varepsilon_d = 2.12$ . At  $r = a$ , the ratio of the thickness of the metal  $t_m$  and of the dielectric  $t_d$  is  $t_m/t_d = 0.039$ . At the outer edge  $r = b$ , this ratio becomes  $t_m/t_d = 0.062$ . In total, the cloak consists of 160 wing pairs of metal and dielectric. Figure A.3(b) shows the fully implemented wing geometry for the cloak, but we have neglected losses here. The performance is similar to the analytical reduced parameters result in terms of the reconstruction of the phase fronts, yet it shows more scattering. Interestingly, although the casted shadow gets more pronounced, the scattering is reduced when the metal losses are introduced (Fig. A.3(c)) and the phase fronts are reconstructed better. This can be understood by having a closer look at the field distribution at the metal wings. Figs. A.3(d) and (e) give an enlarged view of the areas marked with white rectangles in Figs. A.3(b) and (c). A.3(d) shows the case without losses. Strong field enhancements are visible at the metal surfaces, which is a sign for plasmonic oscillations. These plasmons radiate again, which leads to the enhanced scattering. In the case with losses (Fig. A.3(e)), these plasmons are damped and, therefore, scattering is suppressed.

With regard to our goal of assessing the experimental feasibility of a cylindrical cloak at optical frequencies, we must come to the conclusion that the demands on fabrication techniques and materials are too high. First of all, the precise fabrication of metal wings down to Å-levels with a controlled gradient is out of reach at this moment. Secondly, there are simply no materials at optical frequencies which deliver the necessary real parts of the optical parameters while fulfilling the demands on the imaginary parts, namely low losses. In conclusion, the experimental realization of transformation-optical devices which exhibit close-to-zero optical parameters at optical frequencies is not feasible with nowadays materials and fabrication techniques.

## A.2. 90° Beam-Bending Sphere

The concepts of TO enable the design of some rather exotic devices (see Section 2.2), among them unconventional lenses. They can also be used to shed new light on known devices. One example for this is the Eaton lens [43]. The lens consists of a sphere, which has the property of a perfect retro reflector: every light ray that impinges the sphere travels around the center and leaves antiparallel to the original direction of the ray. While proposed in 1952 by J. E. Eaton, it can be improved by transmutation of the singularities in its refractive-index profile by using TO [64]. Several related devices have been proposed [44], among them an invisible sphere (note the difference from an *invisibility* sphere) and a sphere which bends the light not by 180°, as the Eaton lens does, but by 90°.

Since these devices (although not directly derived by TO) are of relevance to the field of TO, we have numerically studied the 90° beam-bending sphere. Since it had never been done before, we performed ray-tracing calculations with the goal of visualizing this device.

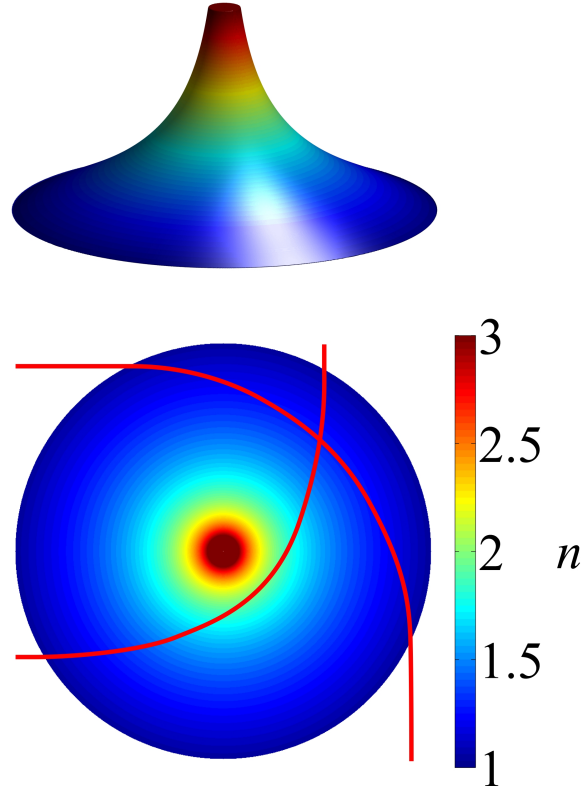


**Figure A.4.:** Refractive-index profile of the 90° beam-bending sphere. The top shows a representation of the profile at a cross section through the center of the sphere. The singular profile has been truncated at  $n = 3$ . The refractive index is encoded in the color and height of the profile. The bottom shows the same cross section, but without height information. Two exemplary rays are depicted. All rays that impinge the sphere undergo a 90° bend. The effect is similar to a mass in a central potential (for example a comet passing by a planet) [45].

The refractive-index profile that is needed for such a sphere is depicted in Fig. A.4. It is given by the implicit equation

$$n^2(r) = \frac{R}{rn(r)} + \sqrt{\left(\frac{R}{rn(r)}\right)^2 - 1}, \quad (\text{A.9})$$

where  $n(r)$  is the refractive index as a function of the radius  $r$ , and  $R$  is the radius of the sphere. As can easily be shown, the refractive index becomes unity for  $r \rightarrow R$  and therefore is continuously connected and impedance-matched to the exterior (which is air or vacuum). For  $r \rightarrow 0$ , the refractive index is singular and goes to infinity. To visualize a feasible device with non-singular parameters, we truncate the index profile at  $n = 3$  (see Fig. A.4).

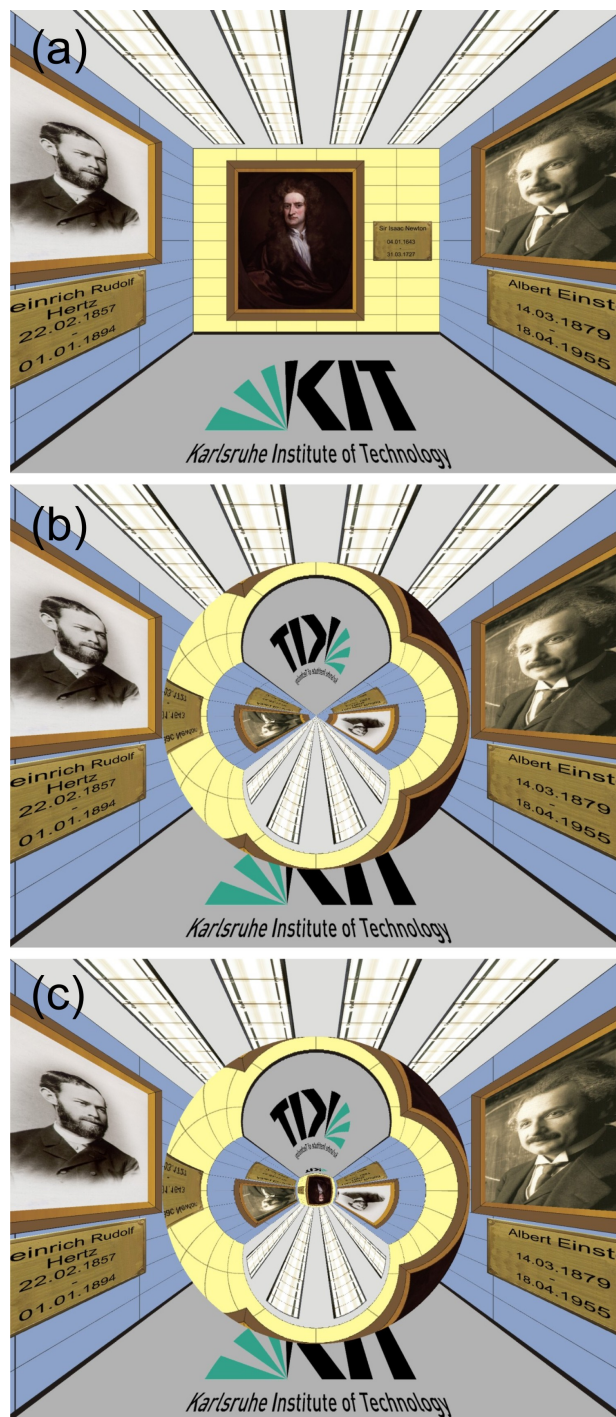


**Figure A.5.:** Photorealistic ray-tracing calculations of the  $90^\circ$  beam-bending sphere. (a) Rendered image of the scenery without any device in it. (b) The  $90^\circ$  sphere with singular refractive-index profile is positioned rather close to the observer. One can “look around the corner” in all spatial directions. (c) The singular profile is truncated at  $n = 3$ . The device gets transparent in the center and one can get a glimpse of Newton’s painting at the back wall [45].

For the ray tracing, we use a code that is similar to the one used in Section 4.3.2, with the difference that the sphere is discretized into  $5 \cdot 10^6$  concentric shells with stepwise constant refractive index. We also use the same scenery of a museum niche (see Fig. 4.8(a)), but with the logo of the Karlsruhe Institute of Technology on the gray floor. Figure A.5 shows the results of the photorealistic ray-tracing calculations. Figure A.5(a) depicts the bare scenery without any device. In Fig. A.5(b), the  $90^\circ$  sphere is introduced with the full singular profile. Note how one can look “around the corner” from all directions. It should be noted that the sphere is positioned rather close to the observer, so that rays with a large angle spread hit the sphere. This is also the reason why one starts to see the back wall with the painting of Newton and its plaquette at the brink of the sphere (corresponding to large angles). Figure A.5(c) shows the  $90^\circ$  sphere with truncated refractive-index profile. Now, one can see through the center of the device, where the refractive index is kept constant at  $n = 3$ , and get a glimpse of Newton’s painting.

These ray-tracing calculations and the visualization of transformation-optical devices in general can lead to new insights into the functionality and the performance of these types of structures. Since we are so reliant on our visual perceptions, they can also fire our imagination into conceiving even more extraordinary designs.

### A.3. Finite-Element Calculations for TM polarization

For completeness, this section shows the finite-element calculations of the full-geometry two-dimensional carpet cloak for TM polarization. We study the wavelength dependence (Fig. A.6) in the same manner as in the case of TE polarization (see Fig. 4.4 in Section 4.2). Here, the situation for short wavelengths is the same as in the case of TE polarization. In contrast, the stop band for TM polarization seems to be notably more narrow. It is only apparent for a wavelength of  $1.0a$  (not shown). Similarly to the TE case, the effective medium limit is reached at around  $2.6a$  and a prominent reflected beam emerges.

Figure A.7 shows the angle dependence of the cloaking effect for a TM-polarized wave. When compared to the TE case (see Fig. 4.5), only small differences are apparent. The cloaking performance is essentially independent of the polarization.

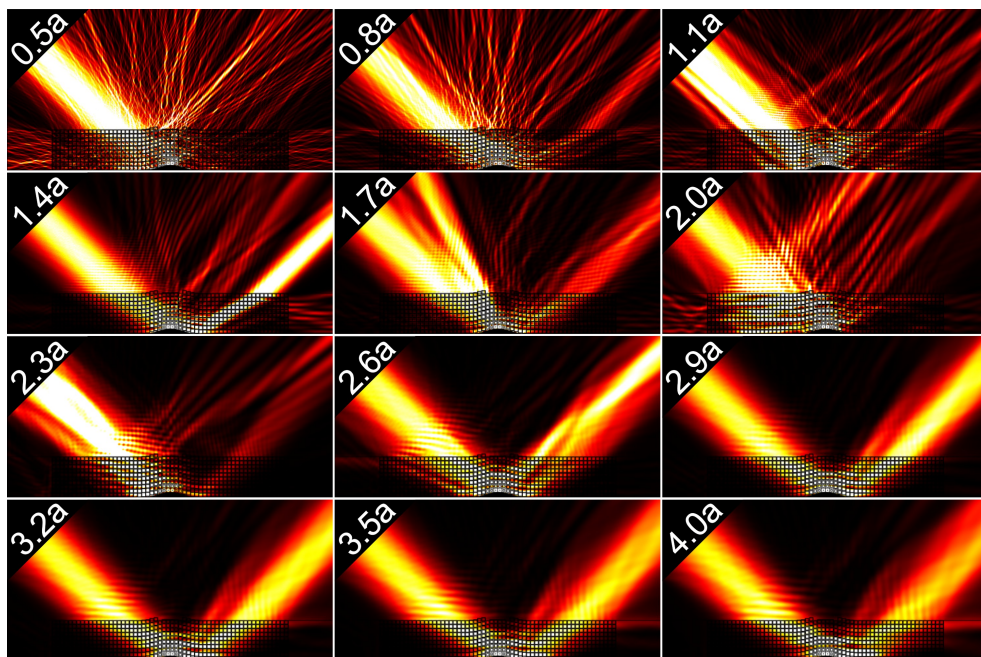


**Figure A.6.:** Same as Fig. 4.4, but for TM polarization. For illustration, we have also depicted the “air-hole” geometry here.

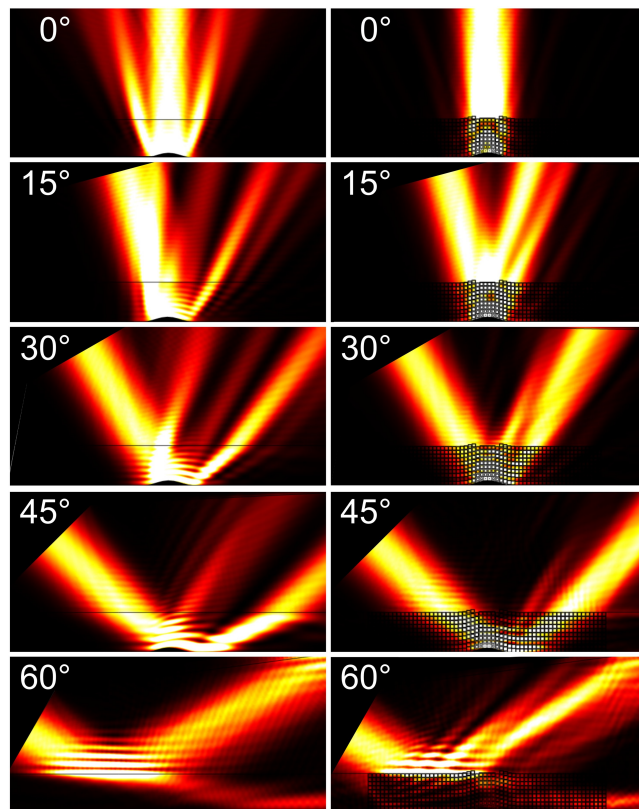


Figure A.7.: Same as Fig. 4.5, but for TM polarization.



# Bibliography

- [1] A. Einstein, “Die Grundlage der allgemeinen Relativitätstheorie,” *Annalen der Physik* **49**, 769–822 (1916).
- [2] I. Y. Tamm, “Electrodynamics of an Anisotropic Medium in the Special Theory of Relativity,” *Journal of the Russian Physical Chemistry Society* **56**, 248 (1924).
- [3] I. Y. Tamm, “Crystal-Optics of the Theory of Relativity Pertinent to the Geometry of a Biquadratic Form,” *Journal of the Russian Physical Chemistry Society* **56**, 1 (1925).
- [4] L. S. Dolin, “On a Possibility of Comparing Three-Dimensional Electromagnetic Systems with Inhomogeneous Filling,” *Izvestiya Vysshikh Uchebnykh Zavedenii. Radioelektronika* **4**, 964–967 (1961).
- [5] E. G. Post, *Formal Structure of Electromagnetics: General Covariance and Electromagnetics* (Interscience Publishers, 1962).
- [6] M. Lax and D. F. Nelson, “Maxwell Equations in Material Form,” *Physical Review B* **13**, 1777–1784 (1976).
- [7] J. Plebanski, “Electromagnetic Waves in Gravitational Fields,” *Physical Review* **118**, 1396–1408 (1960).
- [8] J. B. Pendry, A. J. Holden, W. J. Stewart, and I. Youngs, “Extremely Low Frequency Plasmons in Metallic Mesostructures,” *Physical Review Letters* **76**, 4773–4776 (1996).
- [9] J. B. Pendry, A. J. Holden, D. J. Robbins, and W. J. Stewart, “Magnetism from Conductors and Enhanced Nonlinear Phenomena,” *IEEE Transactions on Microwave Theory and Techniques* **47**, 2075–2084 (1999).
- [10] R. A. Shelby, D. R. Smith, and S. Schultz, “Experimental Verification of a Negative Index of Refraction,” *Science* **292**, 77–79 (2001).
- [11] D. R. Smith, J. B. Pendry, and M. C. K. Wiltshire, “Metamaterials and Negative Refractive Index,” *Science* **305**, 788–792 (2004).

- [12] C. M. Soukoulis, S. Linden, and M. Wegener, “Negative Refractive Index at Optical Wavelengths,” *Science* **315**, 47–49 (2007).
- [13] H. J. Lezec, J. A. Dionne, and H. A. Atwater, “Negative Refraction at Visible Frequencies,” *Science* **316**, 430–432 (2007).
- [14] J. Yao, Z-Liu, Y. Liu, Y. Wang, C. Sun, G. Bartal, A. M. Stacy, and X. Zhang, “Optical Negative Refraction in Bulk Metamaterials of Nanowires,” *Science* **321**, 930 (2008).
- [15] J. Valentine, S. Zhang, T. Zentgraf, E. Ulin-Avila, D. A. Genov, G. Bartal, and X. Zhang, “Three-Dimensional Optical Metamaterial with a Negative Refractive Index,” *Nature* **455**, 376–379 (2008).
- [16] V. G. Veselago, “The Electrodynamics of Substances with Simultaneously Negative Values of  $\varepsilon$  and  $\mu$ ,” *Soviet Physics Uspekhi* **10**, 509 (1968).
- [17] J. B. Pendry, “Negative Refraction Makes a Perfect Lens,” *Physical Review Letters* **85**, 3966–3969 (2000).
- [18] W. C. Chew and W. H. Weedon, “A 3D Perfectly Matched Medium from Modified Maxwell’s Equations with Stretched Coordinates,” *Microwave and Optical Technology Letters* **7**, 599–604 (1994).
- [19] G. W. Milton, M. Briane, and J. R. Willis, “On Cloaking for Elasticity and Physical Equations with a Transformation Invariant Form,” *New Journal of Physics* **8**, 248 (2006).
- [20] A. J. Ward and J. B. Pendry, “Refraction and Geometry in Maxwell’s Equations,” *Journal of Modern Optics* **43**, 773 (1996).
- [21] J. B. Pendry, D. Schurig, and D. R. Smith, “Controlling Electromagnetic Fields,” *Science* **312**, 1780–1782 (2006).
- [22] U. Leonhardt, “Optical Conformal Mapping,” *Science* **312**, 1777–1780 (2006).
- [23] D. Schurig, J. B. Pendry, and D. R. Smith, “Calculation of Material Properties and Ray Tracing in Transformation Media,” *Optics Express* **14**, 9794–9804 (2006).
- [24] U. Leonhardt and T. G. Philbin, “General Relativity in Electrical Engineering,” *New Journal of Physics* **8**, 247 (2006).
- [25] U. Leonhardt and T. G. Philbin, “Transformation Optics and the Geometry of Light,” *Progress in Optics* **53**, 69–152 (2009).
- [26] U. Leonhardt and T. G. Philbin, *Geometry and Light: The Science of Invisibility* (Dover Publications, Inc., 2010).

- 
- [27] H. Chen, C. T. Chan, and P. Sheng, “Transformation Optics and Metamaterials,” *Nature Materials* **9**, 387–396 (2010).
- [28] V. M. Shalaev, “Transforming Light,” *Science* **322**, 384–386 (2008).
- [29] M. S. Mahoney, *The Mathematical Career of Pierre de Fermat, 1601-1665* (Princeton University Press, 1994).
- [30] D. Brewster, “On an Account of a Rock-Crystal Lens and Decomposed Glass Found in Niniveh,” *Die Fortschritte der Physik* **8**, 355–356 (1852).
- [31] C. W. Misner, K. S. Thorne, and J. A. Wheeler, *Gravitation* (Freeman, 1973).
- [32] U. Leonhardt and T. Tyc, “Broadband Invisibility by Non-Euclidean Cloaking,” *Science* **323**, 110–112 (2009).
- [33] J. D. Jackson, *Klassische Elektrodynamik* (deGruyter, 1999).
- [34] Personal correspondance with U. Leonhardt.
- [35] P. Piwnicki and U. Leonhardt, “Optics of Moving Media,” *Applied Physics B: Lasers and Optics* **72**, 51–59 (2001).
- [36] H. Chen and C. T. Chan, “Time Delays and Energy Transport Velocities in Three Dimensional Ideal Cloaking Devices,” *Journal of Applied Physics* **104**, 033113 (2008).
- [37] A. Sommerfeld, “Über die Fortpflanzung des Lichtes in dispergierenden Medien,” *Annalen der Physik* **349**, 177–202 (1914).
- [38] J. Huangfu, S. Xi, F. Kong, J. Zhang, H. Chen, D. Wang, B. Wu, L. Ran, and J. A. Kong, “Application of Coordinate Transformation in Bent Waveguides,” *Journal of Applied Physics* **104**, 014502 (2008).
- [39] D. A. Roberts, M. Rahm, J. B. Pendry, and D. R. Smith, “Transformation-Optical Design of Sharp Waveguide Bends and Corners,” *Applied Physics Letters* **93**, 251111 (2008).
- [40] M. Rahm, D. A. Roberts, J. B. Pendry, and D. R. Smith, “Transformation-Optical Design of Adaptive Beam Bends and Beam Expanders,” *Optics Express* **16**, 11555–11567 (2008).
- [41] W. X. Jiang, T. J. Cui, X. Y. Zhou, X. M. Yang, and Q. Cheng, “Arbitrary Bending of Electromagnetic Waves Using Realizable Inhomogeneous and Anisotropic Materials,” *Physical Review E* **78**, 066607 (2008).
- [42] Z. L. Mei and T. J. Cui, “Arbitrary Bending of Electromagnetic Waves Using Isotropic Materials,” *Journal of Applied Physics* **105**, 104913 (2009).

- [43] J. E. Eaton, “On Spherically Symmetric Lenses,” *Transactions of the IRE Professional Group on Antennas and Propagation* **4**, 66–71 (1952).
- [44] A. J. Danner and U. Leonhardt, “Lossless Design of an Eaton Lens and Invisible Sphere by Transformation Optics with no Bandwidth Limitation,” in “Conference on Lasers and Electro-Optics/International Quantum Electronics Conference,” (2009), pp. 1–2.
- [45] J. C. Halimeh, T. Ergin, N. Stenger, and M. Wegener, “Transformationsoptik: Maßgeschneiderter optischer Raum,” *Physik in unserer Zeit* **41**, 170–175 (2010).
- [46] D. Schurig, J. B. Pendry, and D. R. Smith, “Transformation-Designed Optical Elements,” *Optics Express* **15**, 14772–14782 (2007).
- [47] H. Chen and C. T. Chan, “Transformation Media that Rotate Electromagnetic Fields,” *Applied Physics Letters* **90**, 241105 (2007).
- [48] H. Chen, B. Hou, S. Chen, X. Ao, W. Wen, and C. T. Chan, “Design and Experimental Realization of a Broadband Transformation Media Field Rotator at Microwave Frequencies,” *Physical Review Letters* **102**, 183903 (2009).
- [49] D. Kwon and D. H. Werner, “Polarization Splitter and Polarization Rotator Designs Based on Transformation Optics,” *Optics Express* **16**, 18731–18738 (2008).
- [50] T. Zhai, Y. Zhou, J. Zhou, and D. Liu, “Polarization Controller Based on Embedded Optical Transformation,” *Optics Express* **17**, 17206–17213 (2009).
- [51] U. Leonhardt and P. Piwnicki, “Optics of Nonuniformly Moving Media,” *Physical Review A* **60**, 4301–4312 (1999).
- [52] U. Leonhardt and P. Piwnicki, “Relativistic Effects of Light in Moving Media with Extremely Low Group Velocity,” *Physical Review Letters* **84**, 822–825 (2000).
- [53] U. Leonhardt and T. G. Philbin, “The Case for Artificial Black Holes,” *Philosophical Transactions of the Royal Society* **366**, 2851–2857 (2008).
- [54] D. A. Genov, S. Zhang, and X. Zhang, “Mimicking Celestial Mechanics in Metamaterials,” *Nature Physics* **5**, 687–692 (2009).
- [55] E. E. Narimanov and A. V. Kildishev, “Optical Black Hole: Broadband Omnidirectional Light Absorber,” *Applied Physics Letters* **95**, 041106 (2009).
- [56] H. Chen, R.-X. Miao, and M. Li, “Transformation Optics that Mimics the System Outside a Schwarzschild Black Hole,” *Optics Express* **18**, 15183–15188 (2010).
- [57] Q. Cheng, T. J. Cui, W. X. Jiang, and B. G. Cai, “An Omnidirectional Electromagnetic Absorber Made of Metamaterials,” *New Journal of Physics* **12**, 063006 (2010).

- 
- [58] N. I. Landy, S. Sajuyigbe, J. J. Mock, D. R. Smith, and W. J. Padilla, “Perfect Metamaterial Absorber,” *Physical Review Letters* **100**, 207402 (2008).
- [59] A. V. Kildishev, L. J. Prokopeva, and E. E. Narimanov, “Cylinder Light Concentrator and Absorber: Theoretical Description,” *Optics Express* **18**, 16646–16662 (2010).
- [60] M. Rahm, D. Schurig, D. A. Roberts, S. A. Cummer, D. R. Smith, and J. B. Pendry, “Design of Electromagnetic Cloaks and Concentrators Using Form-Invariant Coordinate Transformations of Maxwell’s Equations,” *Photonics and Nanostructures - Fundamentals and Applications* **6**, 87–95 (2008).
- [61] A. V. Kildishev and V. M. Shalaev, “Engineering Space for Light via Transformation Optics,” *Optics Letters* **33**, 43–45 (2008).
- [62] W. Lu, Z. Lin, H. Chen, and C. T. Chan, “Transformation Media Based Super Focusing Antenna,” *Journal of Physics D: Applied Physics* **42**, 212002 (2009).
- [63] P. Tichit, S. N. Burokur, and A. de Lustrac, “Ultradirective Antenna via Transformation Optics,” *Journal of Applied Physics* **105**, 104912 (2009).
- [64] T. Tyc and U. Leonhardt, “Transmutation of Singularities in Optical Instruments,” *New Journal of Physics* **10**, 115083 (2008).
- [65] Y. G. Ma, C. K. Ong, T. Tyc, and U. Leonhardt, “An Omnidirectional Retroreflector Based on the Transmutation of Dielectric Singularities,” *Nature Materials* **8**, 639–642 (2009).
- [66] J. Perczel, C. Garcia-Meca, and U. Leonhardt, “Partial Transmutation of Singularities in Optical Instruments,” *Journal of Optics* **13**, 075103 (2011).
- [67] A. V. Kildishev and E. E. Narimanov, “Impedance-Matched Hyperlens,” *Optics Letters* **32**, 3432–3434 (2007).
- [68] M. Tsang and D. Psaltis, “Magnifying Perfect Lens and Superlens Design by Coordinate Transformation,” *Physical Review B* **77**, 035122 (2008).
- [69] D. Schurig, “An Aberration-Free Lens with Zero F-Number,” *New Journal of Physics* **10**, 115034 (2008).
- [70] D. Kwon and D. H. Werner, “Transformation Optical Designs for Wave Collimators, Flat Lenses and Right-Angle Bends,” *New Journal of Physics* **10**, 115023 (2008).
- [71] M. Yan, W. Yan, and M. Qiu, “Cylindrical Superlens by a Coordinate Transformation,” *Physical Review B* **78**, 125113 (2008).
- [72] D. A. Roberts, N. Kundtz, and D. R. Smith, “Optical Lens Compression via Transformation Optics,” *Optics Express* **17**, 16535–16542 (2009).

- [73] H. F. Ma and T. J. Cui, “Three-Dimensional Broadband and Broad-Angle Transformation-Optics Lens,” *Nature Communications* **1**, 124 (2010).
- [74] R. Yang, W. Tang, and Y. Hao, “A Broadband Zone Plate Lens from Transformation Optics,” *Optics Express* **19**, 12348–12355 (2011).
- [75] T. Yang, H. Chen, X. Luo, and H. Ma, “Superscatterer: Enhancement of Scattering with Complementary Media,” *Optics Express* **16**, 18545–18550 (2008).
- [76] J. Ng, H. Chen, and C. T. Chan, “Metamaterial Frequency-Selective Superabsorber,” *Optics Letters* **34**, 644–646 (2009).
- [77] X. Luo, T. Yang, Y. Gu, H. Chen, and H. Ma, “Conceal an Entrance by Means of Superscatterer,” *Applied Physics Letters* **94**, 223513 (2009).
- [78] H. Chen, C. T. Chan, S. Liu, and Z. Lin, “A Simple Route to a Tunable Electromagnetic Gateway,” *New Journal of Physics* **11**, 083012 (2009).
- [79] Y. Lai, J. Ng, H. Chen, D. Han, J. Xiao, Z. Zhang, and C. T. Chan, “Illusion Optics: The Optical Transformation of an Object into Another Object,” *Physical Review Letters* **102**, 253902 (2009).
- [80] J. B. Pendry, “All Smoke and Metamaterials,” *Nature* **460**, 579–580 (2009).
- [81] D. Schurig, J. J. Mock, B. J. Justice, S. A. Cummer, J. B. Pendry, A. F. Starr, and D. R. Smith, “Metamaterial Electromagnetic Cloak at Microwave Frequencies,” *Science* **314**, 977–980 (2006).
- [82] W. Cai, U. K. Chettiar, A. V. Kildishev, and V. M. Shalaev, “Optical Cloaking with Metamaterials,” *Nature Photonics* **1**, 224–227 (2007).
- [83] T. G. Philbin, C. Kuklewicz, S. Robertson, S. Hill, F. König, and U. Leonhardt, “Fiber-Optical Analog of the Event Horizon,” *Science* **319**, 1367–1370 (2008).
- [84] A. Greenleaf, Y. Kurylev, M. Lassas, and G. Uhlmann, “Electromagnetic Wormholes and Virtual Magnetic Monopoles from Metamaterials,” *Physical Review Letters* **99**, 183901 (2007).
- [85] S. A. Cummer and D. Schurig, “One Path to Acoustic Cloaking,” *New Journal of Physics* **9**, 45 (2007).
- [86] H. Chen and C. T. Chan, “Acoustic Cloaking in Three Dimensions Using Acoustic Metamaterials,” *Applied Physics Letters* **91**, 183518 (2007).
- [87] S. A. Cummer, B. Popa, D. Schurig, D. R. Smith, J. B. Pendry, M. Rahm, and A. Starr, “Scattering Theory Derivation of a 3D Acoustic Cloaking Shell,” *Physical Review Letters* **100**, 024301 (2008).

- 
- [88] S. Zhang, C. Xia, and N. Fang, “Broadband Acoustic Cloak for Ultrasound Waves,” *Physical Review Letters* **106**, 024301 (2011).
- [89] M. Brun, S. Guenneau, and A. B. Movchan, “Achieving Control of In-Plane Elastic Waves,” *Applied Physics Letters* **94**, 061903 (2009).
- [90] M. Farhat, S. Guenneau, S. Enoch, and A. B. Movchan, “Cloaking Bending Waves Propagating in Thin Elastic Plates,” *Physical Review B* **79**, 033102 (2009).
- [91] M. Farhat, S. Guenneau, and S. Enoch, “Ultrabroadband Elastic Cloaking in Thin Plates,” *Physical Review Letters* **103**, 024301 (2009).
- [92] S. Zhang, D. A. Genov, C. Sun, and X. Zhang, “Cloaking of Matter Waves,” *Physical Review Letters* **100**, 123002 (2008).
- [93] D. Lin and P. Luan, “Cloaking of Matter Waves Under the Global Aharonov–Bohm Effect,” *Physical Review A* **79**, 051605 (2009).
- [94] M. Farhat, S. Enoch, S. Guenneau, and A. B. Movchan, “Broadband Cylindrical Acoustic Cloak for Linear Surface Waves in a Fluid,” *Physical Review Letters* **101**, 134501 (2008).
- [95] H. Chen, J. Yang, J. Zi, and C. T. Chan, “Transformation Media for Linear Liquid Surface Waves,” *Europhysics Letters* **85**, 24004 (2009).
- [96] J. Li and J. B. Pendry, “Hiding Under the Carpet: A New Strategy for Cloaking,” *Physical Review Letters* **101**, 203901 (2008).
- [97] J. Valentine, J. Li, T. Zentgraf, G. Bartal, and X. Zhang, “An Optical Cloak Made of Dielectrics,” *Nature Materials* **8**, 568–571 (2009).
- [98] L. H. Gabrielli, J. Cardenas, C. B. Poitras, and M. Lipson, “Silicon Nanostructure Cloak Operating at Optical Frequencies,” *Nature Photonics* **3**, 461–463 (2009).
- [99] J. H. Lee, J. Blair, V. A. Tamma, Q. Wu, S. J. Rhee, C. J. Summers, and W. Park, “Direct Visualization of Optical Frequency Invisibility Cloak Based on Silicon Nanorod Array,” *Optics Express* **17**, 12922–12928 (2009).
- [100] H. F. Ma, W. X. Jiang, X. M. Yang, X. Y. Zhou, and T. J. Cui, “Compact-Sized and Broadband Carpet Cloak and Free-Space Cloak,” *Optics Express* **17**, 19947–19959 (2009).
- [101] R. Liu, C. Ji, J. J. Mock, J. Y. Chin, T. J. Cui, and D. R. Smith, “Broadband Ground-Plane Cloak,” *Science* **323**, 366–369 (2009).
- [102] E. Kallos, C. Argyropoulos, and Y. Hao, “Ground-Plane Quasicloaking for Free Space,” *Physical Review A* **79**, 063825 (2009).

- [103] E. Kallos, C. Argyropoulos, and Y. Hao, “Simplified Directional Ground-Plane Cloaks,” in “International Conference on Electromagnetics in Advanced Applications,” (2009), pp. 105–108.
- [104] J. C. Halimeh, T. Ergin, J. Mueller, N. Stenger, and M. Wegener, “Photorealistic Images of Carpet Cloaks,” *Optics Express* **17**, 19328–19336 (2009).
- [105] J. Renger, M. Kadic, G. Dupont, S. S. Acimovic, S. Guenneau, R. Quidant, and S. Enoch, “Hidden Progress: Broadband Plasmonic Invisibility,” *Optics Express* **18**, 15757–15768 (2010).
- [106] T. Ergin, N. Stenger, P. Brenner, J. B. Pendry, and M. Wegener, “Three-Dimensional Invisibility Cloak at Optical Wavelengths,” *Science* **328**, 337–339 (2010).
- [107] T. Ergin, J. C. Halimeh, N. Stenger, and M. Wegener, “Optical Microscopy of 3D Carpet Cloaks: Ray-Tracing Calculations,” *Optics Express* **18**, 20535–20545 (2010).
- [108] H. F. Ma and T. J. Cui, “Three-Dimensional Broadband Ground-Plane Cloak Made of Metamaterials,” *Nature Communications* **1**, 21 (2010).
- [109] B. Zhang, T. Chan, and B.-I. Wu, “Lateral Shift Makes a Ground-Plane Cloak Detectable,” *Physical Review Letters* **104**, 233903 (2010).
- [110] P. Zhang, M. Lobet, and S. He, “Carpet Cloaking on a Dielectric Half-Space,” *Optics Express* **18**, 18158–18163 (2010).
- [111] X. Xu, Y. Feng, Z. Yu, T. Jiang, and J. Zhao, “Simplified Ground Plane Invisibility Cloak by Multilayer Dielectrics,” *Optics Express* **18**, 24477–24485 (2010).
- [112] R. Schmied, J. C. Halimeh, and M. Wegener, “Conformal Carpet and Grating Cloaks,” *Optics Express* **18**, 24361–24367 (2010).
- [113] X. Chen, Y. Luo, J. Zhang, K. Jiang, J. B. Pendry, and S. Zhang, “Macroscopic Invisibility Cloaking of Visible Light,” *Nature Communications* **2**, 176 (2011).
- [114] J. Fischer, T. Ergin, and M. Wegener, “Three-Dimensional Polarization-Independent Visible-Frequency Carpet Invisibility Cloak,” *Optics Letters* **36**, 2059–2061 (2011).
- [115] M. Gharghi, C. Gladden, T. Zentgraf, Y. Liu, X. Yin, J. Valentine, and X. Zhang, “A Carpet Cloak for Visible Light,” *Nano Letters* **11**, 2825–2828 (2011).
- [116] J. C. Halimeh, R. Schmied, and M. Wegener, “Newtonian Photorealistic Ray Tracing of Grating Cloaks and Correlation-Function-Based Cloaking-Quality Assessment,” *Optics Express* **19**, 6078–6092 (2011).
- [117] H. Gao, B. Zhang, and G. Barbastathis, “Photonic Cloak Made of Subwavelength Dielectric Elliptical Rod Arrays,” *Optics Communications* **284**, 4820–4823 (2011).

- 
- [118] B. Zhang, Y. Luo, X. Liu, and G. Barbastathis, “Macroscopic Invisibility Cloak for Visible Light,” *Physical Review Letters* **106**, 033901 (2011).
- [119] T. Ergin, J. Fischer, and M. Wegener, “Optical Phase Cloaking of 700 nm Light Waves in the Far Field by a Three-Dimensional Carpet Cloak,” *Physical Review Letters* **107**, 173901 (2011).
- [120] T. Ergin, J. Fischer, and M. Wegener, “Detailed Optical Characterization of Three-Dimensional Visible-Frequency Polarization-Independent Carpet Invisibility Cloak,” *Physica B* (2012). Accepted.
- [121] Z. Nehari, *Conformal Mapping* (McGraw-Hill, 1952).
- [122] N. I. Landy and W. J. Padilla, “Guiding Light with Conformal Transformations,” *Optics Express* **17**, 14872–14879 (2009).
- [123] J. P. Turpin, A. T. Massoud, Z. H. Jiang, P. L. Werner, and D. H. Werner, “Conformal Mappings to Achieve Simple Material Parameters for Transformation Optics Devices,” *Optics Express* **18**, 244–252 (2010).
- [124] J. Müller, T. Ergin, N. Stenger, and M. Wegener, “Doppelt oder gar nicht sehen,” *Physik Journal* **10**, 16–17 (2011).
- [125] D. R. Smith, W. J. Padilla, D. C. Vier, S. C. Nemat-Nasser, and S. Schultz, “Composite Medium with Simultaneously Negative Permeability and Permittivity,” *Physical Review Letters* **84**, 4184–4187 (2000).
- [126] R. M. Walser, “Electromagnetic Metamaterials,” in “Proceedings of SPIE - International Society for Optical Engineering, San Diego,” (2001).
- [127] J. Kästel and M. Fleischhauer, “Quantum Electrodynamics in Media with Negative Refraction,” *Laser Physics* **15**, 135–145 (2005).
- [128] P. Vukusic and J. R. Sambles, “Photonic Structures in Biology,” *Nature* **424**, 852–855 (2003).
- [129] S. John, “Strong Localization of Photons in Certain Disordered Dielectric Superlattices,” *Physical Review* **58**, 2486 (1987).
- [130] E. Yablonovitch, “Inhibited Spontaneous Emission in Solid-State Physics and Electronics,” *Physical Review* **58**, 2059 (1987).
- [131] J. D. Joannopoulos, J. G. Johnson, J. N. Winn, and R. D. Meade, *Photonic Crystals - Molding the Flow of Light* (Princeton University Press, 2008).
- [132] N. W. Ashcroft and N. D. Mermin, *Solid State Physics* (Harcourt Brace College Publishers, 1976).

- [133] K.-M. Ho, C. T. Chan, C. M. Soukoulis, R. Biswas, and M. Sigalas, “Photonic Band Gaps in Three Dimensions: New Layer-By-Layer Periodic Structures,” *Solid State Communications* **89**, 413–416 (1994).
- [134] S. Johnson and J. Joannopoulos, “Block-Iterative Frequency-Domain Methods for Maxwell’s Equations in a Planewave Basis,” *Optics Express* **8**, 173–190 (2001).
- [135] I. Staude, “Functional Elements in Three-Dimensional Photonic Bandgap Materials,” Ph.D. thesis, Karlsruhe Institute of Technology (2011).
- [136] H.-B. Sun, S. Matsuo, and H. Misawa, “Three-Dimensional Photonic Crystal Structures Achieved with Two-Photon-Absorption Photopolymerization of Resin,” *Applied Physics Letters* **74**, 786–788 (1999).
- [137] S. Kawata, H.-B. Sun, T. Tanaka, and K. Takada, “Finer Features for Functional Microdevices,” *Nature* **412**, 697–698 (2001).
- [138] M. Straub and M. Gu, “Near-Infrared Photonic Crystals with Higher-Order Bandgaps Generated by Two-Photon Photopolymerization,” *Optics Letters* **27**, 1824–1826 (2002).
- [139] M. Deubel, G. von Freymann, M. Wegener, S. Pereira, K. Busch, and C. M. Soukoulis, “Direct Laser Writing of Three-Dimensional Photonic-Crystal Templates for Telecommunications,” *Nature Materials* **3**, 444–447 (2004).
- [140] G. von Freymann, A. Ledermann, M. Thiel, I. Staude, S. Essig, K. Busch, and M. Wegener, “Three-Dimensional Nanostructures for Photonics,” *Advanced Functional Materials* **20**, 1038–1052 (2010).
- [141] “Nanoscribe GmbH, <http://www.nanoscribe.de>,” .
- [142] J. Fischer and M. Wegener, “Three-Dimensional Direct Laser Writing Inspired by Stimulated-Emission-Depletion Microscopy,” *Optical Materials Express* **1**, 614–624 (2011).
- [143] S. W. Hell and J. Wichmann, “Breaking the Diffraction Resolution Limit by Stimulated Emission: Stimulated-Emission-Depletion Fluorescence Microscopy,” *Optics Letters* **19**, 780–782 (1994).
- [144] T. A. Klar, S. Jakobs, M. Dyba, A. Egner, and S. W. Hell, “Fluorescence Microscopy with Diffraction Resolution Barrier Broken by Stimulated Emission,” *Proceedings of the National Academy of Sciences of the United States of America* **97**, 8206–8210 (2000).
- [145] T. F. Scott, B. A. Kowalski, A. C. Sullivan, C. N. Bowman, and R. R. McLeod, “Two-Color Single-Photon Photoinitiation and Photoinhibition for Subdiffraction Photolithography,” *Science* **324**, 913–917 (2009).

- 
- [146] L. Li, R. R. Gattass, E. Gershgoren, H. Hwang, and J. T. Fourkas, “Achieving  $\lambda/20$  Resolution by One-Color Initiation and Deactivation of Polymerization,” *Science* **324**, 910–913 (2009).
- [147] J. Fischer, G. von Freymann, and M. Wegener, “The Materials Challenge in Diffraction-Unlimited Direct-Laser-Writing Optical Lithography,” *Advanced Materials* **22**, 3578–3582 (2010).
- [148] P. Knupp and S. Steinberg, *Fundamentals of Grid Generation* (CRC Press, 1994).
- [149] O. Wiener, “Die Theorie des Mischkörpers für das Feld der stationären Strömung,” *Abhandlungen der mathematisch-physischen Klasse der Königlich-Sächsischen Gesellschaft der Wissenschaften* **32**, 509–604 (1912).
- [150] E. Haines, P. Hanrahan, R. L. Cook, J. Arvo, D. Kirk, P. S. Heckbert, and A. S. Glassner, *An Introduction to Ray Tracing* (Academic Press, 1989).
- [151] A. Appel, “Some Techniques for Shading Machine Renderings of Solids,” in “Proceedings of the April 30-May 2, 1968, Spring Joint Computer Conference,” (ACM, New York, NY, USA, 1968), pp. 37–45.
- [152] J. D. Foley and T. Whitted, “An Improved Illumination Model for Shaded Display,” in “Proceedings of the 6th annual conference on computer graphics and interactive techniques,” (1979).
- [153] A. J. Danner, “Visualizing Invisibility: Metamaterials-Based Optical Devices in Natural Environments,” *Optics Express* **18**, 3332–3337 (2010).
- [154] “POV-Ray-The Persistence of Vision Raytracer, <http://www.povray.org>,” .
- [155] G. Dolling, M. Wegener, S. Linden, and C. Hormann, “Photorealistic Images of Objects in Effective Negative-Index Materials,” *Optics Express* **14**, 1842–1849 (2006).
- [156] N. A. P. Nicorovici, R. C. McPhedran, S. Enoch, and G. Tayeb, “Finite Wavelength Cloaking by Plasmonic Resonance,” *New Journal of Physics* **10**, 115020 (2008).
- [157] W. Martienssen and E. Spiller, “Coherence and Fluctuations in Light Beams,” *American Journal of Physics* **32**, 919–926 (1964).
- [158] W. Martienssen and E. Spiller, “Intensity Fluctuations in Light Beams with Several Degrees of Freedom,” *Physical Review Letters* **16**, 531–533 (1966).
- [159] S. Tachi, “<http://www.youtube.com/watch?v=JKPVQal851U>,” .
- [160] S. Tachi, “<http://www.youtube.com/watch?v=PD83dqSfC0Y>,” .
- [161] W. Cai, U. K. Chettiar, A. V. Kildishev, and V. M. Shalaev, “Designs for Optical Cloaking with High-Order Transformations,” *Optics Express* **16**, 5444–5452 (2008).

- [162] P. B. Johnson and R. W. Christy, "Optical Constants of the Noble Metals," *Physical Review B* **6**, 4370–4379 (1972).





# Acknowledgments

Working on a Ph.D. project for three years naturally bears its ups and downs. I would like to make use of this opportunity to thank all those people who contributed to the ups.

First, I would like to express my gratitude to Prof. Dr. Martin Wegener, who advised me for the last three years and who provided me with a nearly perfect working environment. His interest in my work combined with almost daily valuable feedback, his willingness to have open discussions bringing in his knowledge as well as his direct and uncomplicated attitude has motivated me much. I am grateful for his trust in letting me work in the young and exciting field of transformation optics, and for giving me the opportunity to present my work at international conferences.

I would also like to thank Prof. Dr. Kurt Busch, who generously agreed to co-referee my thesis.

A researcher can only work efficiently if he is supported by the “backbone” of the institute, people who look after administrative matters, fabrication and IT-subjects. All the institute’s secretaries were of great help to me, especially Renate Helfen who always told me what I would have to send to whom and why – if she hadn’t already done so herself. I would also like to thank all the workshops, especially the electronics workshop. Cordial thanks go to Heinz Hoffmann, Helmuth Lay, and Werner Gilde for being so patient and for providing me with unbureaucratic support whenever I needed it. Furthermore, I always enjoyed our friendly and open conversations. I am also grateful to our technician Johann Westhauser for supporting me in the construction of needed experimental parts. In addition, I thank the Karlsruhe School of Optics & Photonics (KSOP) and the DFG-Center for Functional Nanostructures (CFN) for financial support during my thesis and for the opportunity to enrich my Ph.D. education by additional trainings.

I would like to express my gratitude to all my colleagues in our group for providing a friendly environment and helping me whenever I asked for it. Joachim Fischer, Dr. Nicolas Stenger and Jonathan Müller are the people I worked with most closely, and I especially thank them for fruitful discussions on work-related subjects, their contributions to the success of this thesis, and silly laughs on subjects related to nothing whatsoever making work more enjoyable.

I am grateful to all critical readers of this manuscript, namely Martin Streichfuss, Joachim Fischer, Jonathan Müller, Dr. Nicolas Stenger, and Bilge Reischauer, for helping me to “polish” my thesis.

Finally, I would like to express my deep feelings of love and gratitude to the people who are most special to me: my lovely wife Sarah, my wonderful son Selim, my sister Bilge and both my parents Ulrike and Erol.



